ELECTROCHEMICAL MICROFLUIDIC SENSORS WITH INTEGRATED ION-SELECTIVE POLYMER MEMBRANES FOR THE DETECTION OF TRACE IONS IN WATER

AYOBAMI ELISHA OSEYEMI

A DISSERTATION SUBMITTED TO

THE FACULTY OF GRADUATE STUDIES

IN PARTIAL FULFILLMENT OF THE REQUIREMENTS

FOR THE DEGREE OF DOCTOR OF PHILOSOPHY

GRADUATE PROGRAM IN MECHANICAL ENGINEERING

YORK UNIVERSITY

TORONTO, ONTARIO

September 2025

Abstract

There is a growing need for low-cost, portable, and sensitive sensors capable of detecting trace metal ions in water for environmental and public health protection as well as energy applications. Existing analytical techniques, while accurate, are often expensive, time-consuming, and less-practical for field deployment because they rely on bulky instrumentation and complex electrode modifications. Ion-imprinted polymers (IIPs) offer a promising alternative by enabling selective recognition of target ions through engineered binding sites within a polymer matrix. However, most IIP-based electrochemical sensors rely on surface coating of electrodes, which introduces variability, limits reproducibility, and increases fabrication complexity. Furthermore, the integration of IIPs into microfluidic platforms, especially as stand-alone sensing membranes rather than surface-bound films, remains underexplored.

This research aims to develop a novel microfluidic electrochemical sensing platform that leverages in-situ synthesized, stand-alone IIP membranes for the selective detection of sodium (Na^+), lead (Pb^{2+}), and lithium (Li^+) ions in water. In Objective 1, an ion-selective polymer (ISP) membrane sensor was developed to detect low-level salinity in drinking water. The sensor achieved a limit of detection (LOD) of 0.45 ppm and demonstrated a 28-fold sensitivity improvement compared to the membrane-less configuration. In Objective 2, sodium-specific IIP membranes were fabricated using 15-crown-5 as the ionophore. The Na-IIP sensor achieved an LOD of 58 ppb and a sensitivity of 9.1 nA/ppm, showing over 3-fold improved sensitivity compared to the non-imprinted sensor and strong selectivity over competing alkali metals. In Objective 3, the platform was extended to detect Pb^{2+} and Li^+ using tailored IIP formulations. The Pb-IIP sensor achieved a LOD of 7.3 ppb with 6.1-fold higher sensitivity than the membrane-less control, while the Li-IIP sensor achieved a LOD of 168 ppb and exhibited a 138.8% higher response to Li^+ over K^+. In all

cases, the sensors exhibited high reproducibility, effective selectivity in multi-ion environments, and strong recovery rates (69–109%) in municipal tap water.

This work demonstrates that the integration of IIP membranes as stand-alone structures in microfluidic chips provides a robust, cost-effective, and scalable approach for metal ion detection without the need for electrode pretreatment. The photopolymerizable design simplifies fabrication and enables future automation. The developed platform holds promise for environmental monitoring, lithium resource management, and public health surveillance. Future research should focus on multiplexing, enhancing membrane stability in harsher matrices, and integrating the system into fully automated Point-of-Need (PoN) diagnostic devices for real-time water quality monitoring.

Acknowledgement

Completing this study and writing my thesis has been one of the most challenging yet fulfilling experiences of my life. As I reach this milestone, I am overwhelmed with gratitude for the many people whose support has made this accomplishment a reality.

First, I would like to extend my deepest appreciation to my supervisor, Professor Pouya Rezai, for his exceptional guidance, encouragement, and unwavering support. His expertise, insightful feedback, and mentorship have played a vital role in shaping both my research and my development as a scholar. I am truly grateful for the privilege to work under his supervision.

I am also sincerely thankful to my committee members, Professors Razieh Salahandish and Reza Rizvi, for their invaluable feedback and encouragement throughout this process. Their thoughtful guidance, particularly during committee meetings and my comprehensive examination, was instrumental in refining my work and broadening my academic perspective.

I would also like to express my sincere appreciation to my colleagues at the ACµTe Lab, both past and present, for their support in this journey. In particular, I am grateful to Dr. Alireza Zahibihesari, Dr. Shapour Jafargholinejad, and Dr. Arezoo Khalili for their assistance in various capacities, especially during the early stages of this research.

My heartfelt gratitude goes to my wife, Esther, whose unwavering love, patience, and companionship sustained me throughout this journey. Meeting and getting married to her during the program has been one of the greatest blessings of my life.

I am equally indebted to my parents and my sister, Funmilayo, for their constant love, encouragement, and belief in me. Their enduring support has been the foundation upon which all my achievements rest.

Above all, I give the utmost thanks to God Almighty, the One who was, who is, and who is to come, for granting me the grace to be alive and to have come this far. All praise, honor, and adoration belong to Him alone.

Finally, I would like to acknowledge the financial support and recognition I received during my PhD, including the York Graduate Fellowship, the Academic Excellence Award, the 2025 SME Toronto Chapter 26 Joseph R. Benedetto Scholarship, the 2025 Mechanical Engineering Teaching Excellence Award, the Conference Travel Awards for both teaching assistantship and conference presentations, and the Francis Tetteh Memorial Award. These contributions were instrumental in helping me focus on and successfully complete my study.

Table of Contents

List of Tables

List of Figures

Abbreviations

AAM: Acrylamide

AIBN: Azobisisobutyronitrile

AuNPs: Gold nanoparticles

APTES: 3aminopropyltrimeth-oxysilane

Cd(NO3)2·4H2O: Cadmium nitrate tetrahydrate

CE: Counter electrode

CNTs: Carbon nanotubes

DBP: Dibutylphthalate

DI Water: Deionized water

DMPA: 2,2-Dimethoxy-2-Phenyl-Acetophenone

DMSO: Dimethyl Sulfoxide

DNP: Dinonylphthalate

DPC: Diphenylcarbazide

DOS: Dioctyl Sebacate

EDGMA: Ethylene Glycol Dimethacrylate

EDTA: Ethylenediaminetetraacetic Acid

HNO3: Nitric acid

IIP: Ion-imprinted polymer

ISP: Ion-selective polymer

g-C_3N_4: Graphitic Carbon Nitride Nanosheets

GNS: Graphene Nano Sheets

KCl: Potassium chloride

KNO3: Potassium nitrate

KTpClPB: Potassium Tetrakis (4-Chlorophenyl) Borate

LiCl: Lithium Chloride

Li-IIP: Lithium ion-imprinted polymer

MAA: Methacrylic Acid

MCWNT: Multi-Walled Carbon Nanotubes

MIP: Molecularly imprinted polymer

MMA: Methyl Methacrylate

MWs: microwires (MWs)

MWCNT: Multi-Walled Carbon Nanotubes

NaCl: Sodium Chloride

Na-IIP: Sodium ion-imprinted polymer

$NaNO_3$: Sodium Nitrate

NaTPB: Sodium Tetraphenylborate

Na_2SO_4: Sodium Sulfate

NPOE: o-Nitrophenyl Octyl Ether

NVP: N-Vinyl Pyrrolidone

$Pb(NO_3)_2$: Lead Nitrate

PC: Polycarbonate

PDMS: Polydimethylsiloxane

PMMA: Polymethyl Methacrylate

PON: Point-of-Need

PSA: Pressure-Sensitive Adhesive

PVC: Polyvinyl Chloride

RE: Reference Electrode

RGO: Reduced Graphene Oxide

SD: Standard deviation

SWCNT: Single-Walled Carbon Nanotubes

TCBZ : Thiosemicarbazide

WE: Working Electrode

2-VP: 2-vinyl pyridine

4-VP: 4-vinyl pyridine

8-HQ: 8-Hydroxyquinoline

12C4: 12-Crown-4

15C5: 15-Crown-5

Chapter 1

1. Motivation and introduction

Water pollution poses significant risks to public health and the environment, necessitating the development of rapid and reliable methods for drinking water quality monitoring [1]. Diseases caused by contaminated drinking water result in the death of a million people every year—the majority of which are children [2]. Water pollution arises when substances, such as chemicals or microorganisms, are present in harmful concentrations in water bodies, causing disruptions to the water's beneficial use and the natural balance of the ecosystem [3]. Contaminated water can harbor pathogens responsible for diseases such as cholera, typhoid fever, and dysentery, while exposure to pollutants like heavy metals, pesticides, and industrial chemicals has been linked to neurological disorders, cancer, and reproductive complications [4]. Water contaminants, whether inorganic, organic, or biological, exhibit dynamic concentration variations influenced by geographical location, contamination sources, environmental conditions, and treatment methods. For instance, sodium levels in Canadian drinking water fluctuate seasonally and geographically [5, 6]. Groundwater, surface water, and tap water exhibit sodium concentrations ranging from 6−130 ppm [6], 1−300 ppm [7], and 0.3−242 ppm [8], respectively due to natural mineral deposits, agricultural runoff, and industrial effluents. To comply with the widely recommended total daily sodium intake of 500 ppm for individuals on a sodium-restricted diet, drinking water sodium concentrations should not exceed 20 ppm [9, 10]. Among heavy metals, lead remains one of the most hazardous contaminants in drinking water, often attributed to aging infrastructure containing lead pipes in residential areas [11]. The World Health Organization (WHO) has established a

maximum acceptable concentration (MAC) of 10 µg/L for lead in drinking water [12]. Lead exposure primarily results from the corrosion of plumbing materials or contamination from external sources, as exemplified by the Flint, Michigan water crisis [13, 14]. Table 1-1 summarizes the maximum permissible concentration limit of the contaminant, contamination sources and some effects exposure to these contaminants.

Table 1-1 Contaminants and their potential effects on human health.

Contaminant MAC (ppm)	**Health effects**	**Sources**	**References**
Arsenic (0.01)	Skin and internal cancer, Peripheral neuropathy, Cardiovascular, dermatologic diseases	Agricultural application, geothermal activity, mining and smelting, electronic wastes	[15, 16]
Lead (0.01-0.015)	Birth defects, autism, dyslexia, kidney damage, paralysis, internal cancer, muscular weakness	Mining, natural deposits, PVC pipes, lead batteries, lunch boxes, manufacturing processes	[17, 18]
Cadmium (0.004)	Preterm birth, cancer (pancreatic, breast, ovarian), neuron cell damage, kidney disease, DNA damage, oxidative stress	Plastic synthesis, natural deposits, photovoltaic cell, mining, tobacco, sewage disposal	[19, 20]
Copper (1-2)	Liver and kidney damage, anemia, hyperactivity, alopecia, adreno-corticol	Electronic product, fertilizers, tanning, transmission industry, electroplating	[21, 22]
Nitrite (0.2)	Gastric problem, blue baby syndrome	Natural deposits, animal waste, septic tanks, Agricultural wastes	[23, 24]
Sodium (20 for low sodium diet, 200 for drinking water)	Blood pressure, heart disease, kidney disease	Natural (rock and soil), de-icing salts, , sewage, effluents	[5, 9]
Pesticide (1,3-dicholorphoropene) (0.02)	Low birth weight, skin irritations, brain tumors	Agricultural applications	[25]

Effective water quality monitoring necessitates rapid, efficient testing in potentially contaminated environments [26]. However, the extensive sample testing required across varying locations and times places a substantial burden on specialized laboratories, which primarily rely on centralized analytical techniques. This reliance on conventional detection methods impedes prompt intervention and water resource management [27]. Traditional water quality assessment methods, such as solid-phase extraction coupled with liquid chromatography-tandem mass spectrometry, are highly effective for targeted analysis of known contaminants [28]. These techniques offer low limits of quantification (LOQ), high precision, and robust quality assurance/control (QA/QC) protocols. Nevertheless, they are expensive, time-intensive, and require specialized equipment and trained personnel, making them unsuitable for field monitoring. Additionally, current methods involve sample collection, transportation, and laborious pretreatment using toxic solvents that pose environmental hazards [29].

In this context, chemo-sensors have emerged as highly sensitive detection devices capable of converting chemical or physical events into measurable signals [30, 31]. These sensors utilize molecular receptors that selectively bind to target analytes. A typical sensor integrates molecular recognition elements with transducers (e.g., optical or electrochemical devices), signal processors, and end-user interfaces tailored for diverse applications (Fig. 1-1). Such systems can detect a wide range of contaminants, including heavy metals, pesticides, pharmaceuticals, and biological agents (e.g., bacteria or viruses) [32, 33].

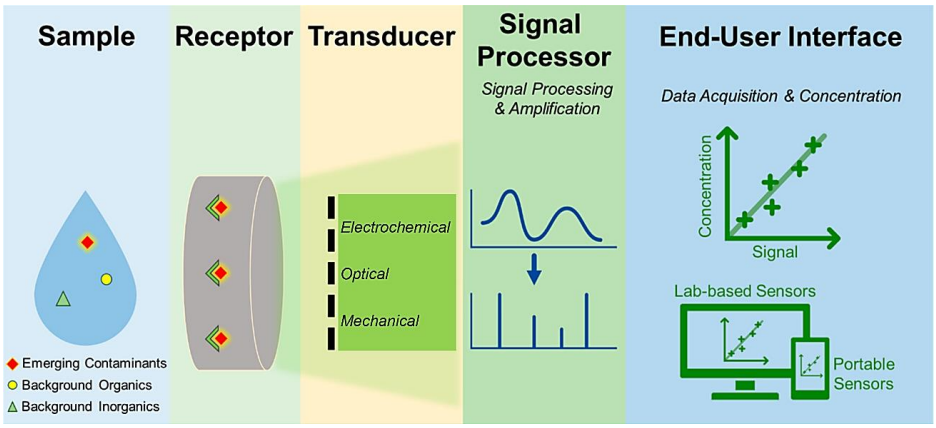

Fig. 1-1 Schematic illustration of a sensor system comprising key components: receptor (recognition unit), transducer, and signal processor (output system), and end-user interface. Adapted from Ref. [1], with permission from American Chemical Society (ACS).

The popularly used transduction mechanisms are broadly categorized into electrochemical, optical, and mechanical transducers (Fig. 1-1). Mechanical transducers, such as piezoelectric and micro-electro-mechanical systems (MEMS), detect mechanical property changes induced by recognition reactions. Quartz Crystal Microbalance (QCM), a widely used piezoelectric transducer, measures oscillation frequency variations corresponding to layer thickness changes during analyte interactions [34]. Optical transducers employ techniques like Surface Plasmon Resonance (SPR) and Total Internal Reflection Fluorescence (TIRF), which are extensively documented in the literature [35, 36]. Electrochemical transducers are considered the most sensitive and reliable due to their rapid response, cost-effectiveness, and miniaturization potential, making them ideal for point-of-need (PoN) applications [1] as pursued in this thesis work.

Electrochemical detection employs techniques such as amperometry, voltammetry, and impedance spectroscopy, ensuring signals with high sensitivity and specificity [37]. Conventional electrochemical sensor designs employ either a two-electrode or a three-electrode system [38]. In the three-electrode system, the setup includes a working electrode (WE), a reference electrode

(RE), and a counter electrode (CE). The WE, typically made of inert materials like gold, platinum, or glassy carbon, is where the electrochemical reaction of interest occurs, enabling the detection and quantification of analytes. The RE, often an Ag/AgCl or saturated calomel electrode, maintains a stable potential against which the WE's potential is measured. The CE, usually made of graphite or platinum, completes the circuit and balances current flow to prevent charge accumulation at the WE [96]. Two-electrode systems, simpler in design, combine the functions of the RE and CE into a single auxiliary electrode. This electrode arrangement facilitates electrical signal generation through the interaction of the analyte with the electrode surface. Measurement techniques in such systems include voltametric, potentiometric, and impedimetric methods [39]. Voltametric sensors apply potential and measure current, with variations like amperometry, linear sweep voltammetry, cyclic voltammetry (CV), and chronoamperometry. Potentiometric sensors use a constant electric current to measure potential changes for analyte detection. Impedimetric sensors apply alternating potential, measuring the resulting impedance, which provides analytical information about the analyte.

Recent years have witnessed increased adoption of recognition elements such as aptamers, molecularly imprinted polymers (MIPs) and ion-imprinted polymers (IIPs) [40] in the advancement of portable chemical sensors and biosensors, facilitated by the discovery of novel recognition elements and the integration of nanotechnology, ultimately enhancing the capabilities of sensors in terms of sensitivity, specificity, and limits of detection (LOD) and quantification (LOQ) [41, 42].

MIPs and IIPs are synthesized via the molecular imprinting technique (MIT), wherein a target analyte serves as a template to create specific recognition sites within the polymer matrix. While

MIPs offer advantages over conventional receptors, their development poses challenges, including the absence of a universal preparation method, complex transducer integration, and difficulties in translating binding events into measurable signals [43].

This research aims to deepen the understanding of IIPs in microfluidic chemical sensing by developing and optimizing methodologies for the controlled synthesis of stand-alone membranes. Unlike conventional approaches that coat electrodes with MIPs or IIPs, this study explores an innovative microfluidic chamber-based design featuring a membrane positioned between two electrodes that transduce interactions between the membrane and target analytes electrochemically.

1.1. Biosensors and Chemo-Sensors

Sensors serve as complementary platforms to traditional analytical methods, offering rapid, sensitive, and reliable detection of analytes. Their ease of operation, and minimal sample pretreatment make them highly suitable for portable PoN applications [44, 45].

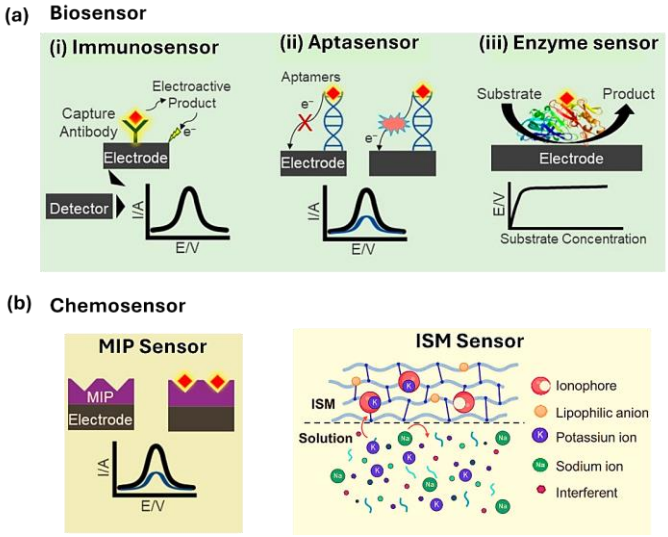

Fig. 1-2 Working principles of biosensors and chemo sensors for contaminant detection. Adapted from Ref. [1, 46] with permission from ACS and Elsevier, respectively.

Biosensors (Fig. 1-2a) use biological recognition elements such as aptamers, antibodies and enzymes to selectively interact with target analytes, generating a measurable signal that is transduced into electrical or optical outputs (e.g., immunosensors, aptasensors, and enzyme-based sensors) [47]. These biosensing platforms have been widely applied for detecting various water pollutants [48], including pesticides [49], heavy metals, antibiotics as well as endocrine disrupting chemicals [50]. The performance of biosensors is evaluated based on key parameters such as sensitivity, selectivity, response time, LOD, LOQ, and stability. These factors are strongly influenced by the properties of the recognition elements and transducers[51]. The downside of biosensing technologies, however, include stability of the bioreceptor in real-word applications and interference caused by nonspecific binding or adsorption of unwanted contaminants in complex environmental matrices.

Chemo sensors (Fig. 1-2b) combine the selectivity of synthetic receptors (e.g., polymers, metal complexes, ionophores) with the sensitivity of transducers to enable precise target detection [43]. They detect and respond to chemical substances by converting chemical information from the binding interaction into a measurable signal. Two widely used chemosensor types include ion-selective electrode/membrane (ISE/ISM)-based sensors and MIP/IIP-based sensors [52, 53]. ISMs are commonly employed in various sensor configurations, including electrochemical (voltametric/coulometric, potentiometric, and electrolyte-gated transistor-based) as well as optical systems. ISMs, as used in potentiometric sensors, contain ionophores—ligands that preferentially bind target ions in a lipophilic medium [54, 55]. This high specificity enables ISM-based sensors to quantify free ion concentrations in environmental samples, even in the presence of other chemical species, making them valuable tools for diverse applications [53]. On the other hand,

MIPs in MIP-based sensors function as stable polymeric receptors with molecular recognition capabilities, achieved by imprinting a target analyte (template) during polymerization. The subsequent removal of the template leaves binding sites that retain the analyte's size and shape [43]. The high thermal and mechanical stability, specificity, and sensitivity of MIP-based electrochemical sensors make them superior alternatives to traditional instruments and other sensor types [56]. Given their enhanced stability and versatility, imprinted polymers were selected as synthetic receptors for this research and will be discussed in detail in subsequent sections.

1.2. Developing sensors with microfluidic technology

Microfluidics allows for low-cost mass production of compact and field-deployable devices that require a short analysis time and small sample volume for measurement. Fundamentally, the surface to volume ratio in microfluidic devices increases substantially due to the scaling laws of physics, enabling the achievement of high levels of sensitivity and low detection limits [57, 58]. The miniaturization of on-chip/on-site sample analysis not only streamlines processes but also mitigates contamination risks during sample handling and transportation. A typical microfluidic detection system requires a method for reagent and sample introduction, a method for transporting and mixing the sample and reagent within the system, and a dedicated detection device (Fig. 1-3a) [59]. Some advanced microfluidic detection systems incorporate features such as membranes, monoliths, pillars, pneumatic controls, and acoustic controls, enhancing the overall performance of the analysis [60].

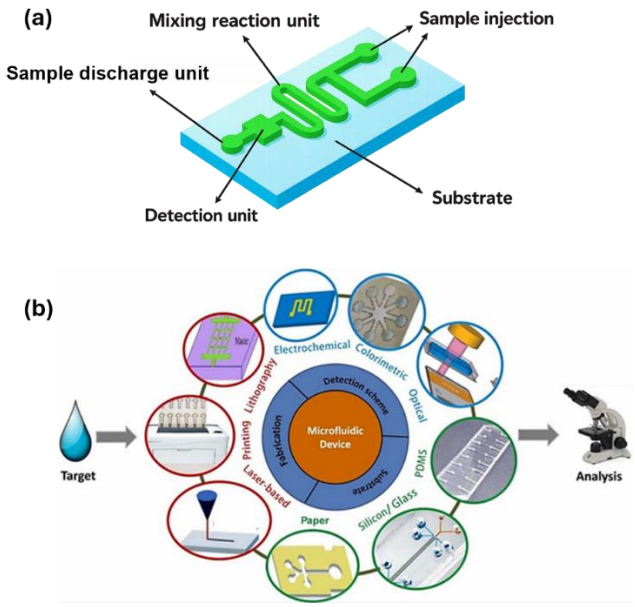

Fig. 1-3 Microfluidic technology for contaminant detection. Schematic illustrations of (a) a representative microfluidic sensing device and (b) a typical microfluidic sensing scheme. Reprinted from Ref. [59, 61], with permission from Elsevier.

Over the years, various detection mechanisms have been explored for microfluidics-based monitoring systems. These include optical methods such as absorbance-based, fluorescence-based, chemiluminescence-based, and surface plasmon resonance-based [34, 62, 63], electrochemical techniques like voltammetry, amperometry, and impedance [41, 64, 65], and mass spectrometry (e.g., QCM and microcantilevers) detections [34, 66]. Each of these methods brings unique advantages to the microfluidic platform, offering versatility and adaptability to diverse analytical needs. The applications of microfluidic detection systems are vast, ranging from drug screening [67], diagnostics [68], protein studies [69, 70], and cell studies [71], to environmental monitoring [72], power generation [73], and food analysis [74].

Recent advancements in microfluidic in lab-on-a-chip (LOC) systems have ushered in automation, increased sensitivity, rapid analysis, and broad analytical capabilities, leading to major

growth in diagnostics and other biological/chemical applications [74, 75]. Microfluidic chips can be fabricated using various materials ranging from traditional materials like glass and silicon to contemporary options such as paper and polymer (e.g., Polydimethylsiloxane (PDMS), Cyclic olefin copolymer (COC), Polymethyl methacrylate (PMMA)) [75, 76]. Fig. 1-3b illustrates the typical fabrication processes and detection approaches used in microfluidic devices. Selecting an ideal material for microfluidics-based Point-of-Need/Point-of-Care (PON/POC) systems requires careful consideration of factors like fabrication ease, integration capability, functionality, modification potential, and cost-effectiveness. An ideal microfluidics-based sensing platform should be easily fabricated, integrable, low-cost, and multifunctional. The selection of materials significantly influences fundamental properties like optical characteristics, cost, and chemical/physical attributes crucial for the realization and performance of microfluidic assays [76].

1.3. Ion-imprinted polymers (IIPs)

A schematic representation of an ion-imprinting process is illustrated in Fig. 1-4.

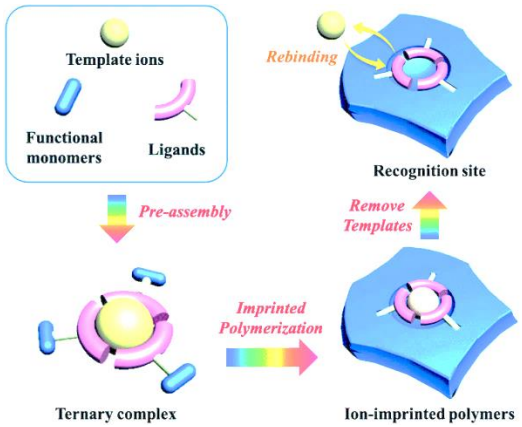

Fig. 1-4 A schematic illustration of an ion imprinting technique. Reprinted from Ref. [77], with permission from Royal Society of Chemistry (RSC).

The ion imprinting technology (IIT) is a specialized form of molecular imprinting that mimics the selective interactions between biological receptors and ligands [78]. In recent years, this technique has gained significant attention across various fields, including the chemical industry, medicine, food safety, environmental science, and analytical detection [79, 80]. The synthesis of IIP typically follows a multi-step process. Initially, a preassembly stage involves the formation of ternary complexes between template ions, functional monomers, and ligands. These complexes are then polymerized in the presence of a crosslinking agent, creating a stable polymeric structure. The subsequent removal of the template ions—often achieved through protonation—leaves behind highly specific recognition sites that are capable of selectively binding the target ions upon re-exposure while minimizing interference from non-target species [81].

IIPs are highly versatile due to their ability to generate recognition sites tailored to a wide variety of target ions, regardless of differences in size, shape, or chemical functionality [81]. Furthermore, their synthesis is relatively straightforward, and their binding characteristics can be fine-tuned through various engineering techniques to enhance selectivity and affinity, making them particularly valuable for water quality monitoring and contaminant detection [80, 82]. Hence, IIPs can be strategically synthesized and used as recognition elements for detecting emerging water contaminants.

The composition of IIPs includes key components such as functional monomers, ligands, cross-linkers, initiators, and solvents. The formulation and synthesis parameters directly influence the final morphology and binding performance of IIPs. Among these factors, the selection of an appropriate functional monomer and ligand is crucial, as it governs the interaction between the polymer and the target ion, thereby affecting both binding efficiency and specificity. The choice of

monomer and ligand is determined by the nature and strength of their interaction with the template ions [77, 81]

The interactions between IIPs and target ions during polymerization and subsequent recognition phases can occur through covalent, non-covalent, or ion-exchange mechanisms. Covalent interactions involve the formation of strong, reversible chemical bonds between the template ion and functional monomer, leading to highly stable binding sites, though the rigidity of these bonds may sometimes limit rebinding efficiency [83]. In contrast, non-covalent interactions, such as hydrogen bonding, van der Waals forces, hydrophobic interactions, and electrostatic forces, allow for more flexible and reversible recognition of target ions, making non-covalent imprinting the most widely used approach due to its ease of synthesis and adaptability [81, 83]. Additionally, ion-exchange interactions play a crucial role in the selective recognition of charged species, where target ions are exchanged with counterions within the polymer matrix, enhancing the specificity and affinity of IIPs [77]. By leveraging these molecular interactions, IIPs can achieve highly selective binding properties, making them ideal candidates for applications in environmental monitoring, wastewater treatment, and analytical sensing technologies.

The next section discusses the impact of each component on the synthesis and functionality of IIPs, as well as the parameters of polymerization and synthesis. Even though many studies have been done to understand the effect of various parameters associated with the synthesizing IIPs, it is still challenging to rationally comprehend them. Nonetheless, some findings can be highlighted, based on earlier studies.

1.3.1. Components for the synthesis of IIPs

The synthesis of IIPs generally begins with the formation of a complex between the ion template and at least one functional monomer. This complex is then copolymerized with a crosslinker, resulting in a polymer network that encapsulates the ion templates. In the final step, the templates are removed through a leaching process, leaving behind highly specific binding sites that are optimized to selectively recognize and adsorb the target ion used during synthesis [84]. This section presents a description of these components with reference to the most used ones in the literature (Fig. 1-5).

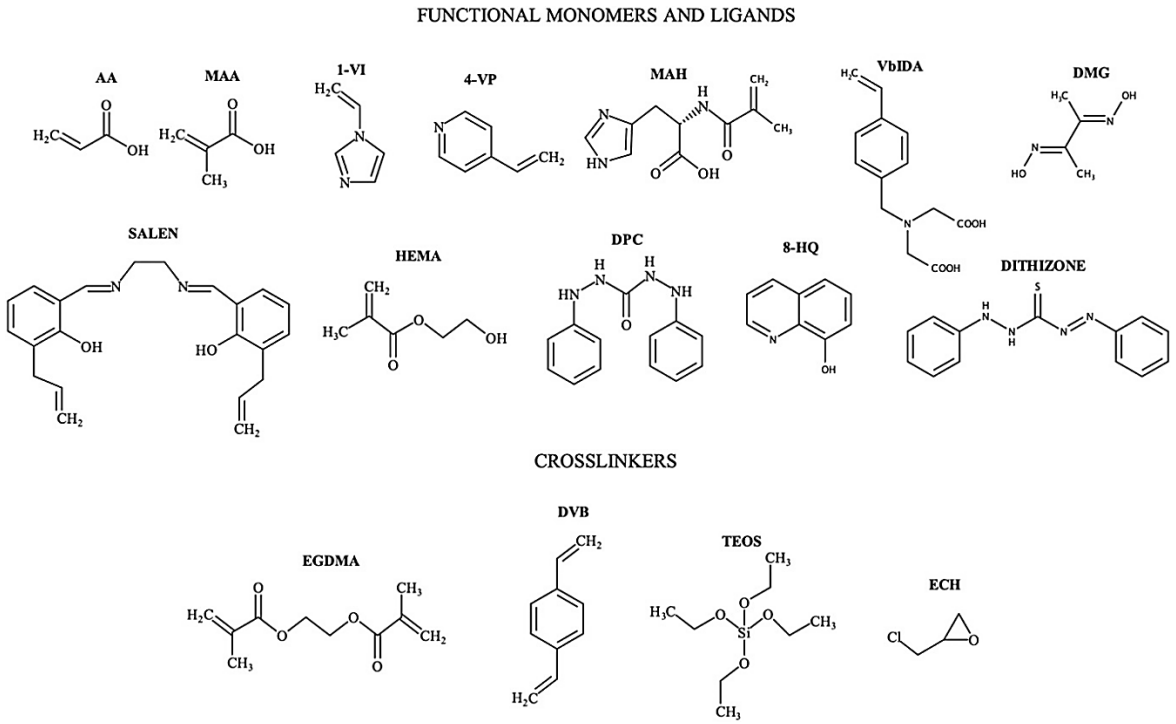

Fig. 1-5 Common functional monomers, ligands, and crosslinkers for synthesis of IIPs. Acrylic acid (AA), Methacrylic acid (MAA), 1-Vinylimidazole (1-VI), 4-vinylpyridine (4-VP), N-methacryloyl-(L)-histidine (MAH), Vinylbenzyl iminodiacetic acid (VbIDA), Dimethylglyoxime (DMG), N,N-o-phenylene bis (SALEN), 2-hydroxy methacrylate (HEMA), Diphenylcarbazide (DPC), 8-hydroxyquinoline (8-HQ), Ethylene glycol dimethylacrylate (EGDMA), Divinylbenzene (DVB), Tetraethoxysilane (TEOS), epichlorohydrin (ECH). Reprinted from Ref. [85] with permission from Elsevier.

1.3.1.1. Ligands, monomers, and crosslinker

Ligands, monomers, and cross-linkers play a central role in ion-imprinted polymer (IIP) synthesis, collectively shaping the chemical specificity, binding affinity, and mechanical stability of the final membrane. These components directly influence the sensor's ability to recognize target ions through selective binding interactions and maintain its structural integrity during operation. Ligands enable template-specific interactions through ion chelation mechanisms, where lone-pair-donating heteroatoms such as oxygen, nitrogen, sulfur, or phosphorus form coordination complexes with the metal ion template. Effective ligands contain multiple chelating groups to enhance affinity and selectivity. Many commercially available monomers possess intrinsic chelating properties, such as acrylic acid (AA) [86], 4-vinylpridine (4-VP) [87], and 1-vinylimidazole (1-VI) [88]. These monomers possess a polymerizable vinyl group, allowing them to be directly incorporated into the polymer structure. However, their selectivity is often relatively low. To enhance binding specificity, ligands without inherent polymerizable functionality can be chemically modified to introduce reactive groups, as seen in vinylbenzyl iminodiacetic acid (VbIDA) [89], N-methacryloyl-l-histidine (MAH) [90], and crown ethers [91]. Additionally, the introduction of the trapping method has enabled the use of a broader range of ligands lacking polymerizable groups, such as 8-hydroxyquinoline (8-HQ) [92], and dithizone [93]. This approach involves forming a ternary complex between the metal ion, a vinylated ligand, and a non-vinylated ligand. Typically, a commercially available monomer such as 4-VP, 2-VP, 1-VI, methacrylic acid (MAA), or AA is incorporated into the system to facilitate polymerization [94, 95].

A crosslinker is also essential for IIP synthesis, as it forms copolymers with the functional monomers to establish a three-dimensional polymer framework, stabilizing the imprinted binding

sites and preserving membrane porosity. Ethylene glycol dimethylacrylate (EGDMA) is the most widely used crosslinker, though alternatives such as trimethylolpropane triacrylate (TMPTA) [94], divinylbenzene (DVB) [96], epichlorohydrin (ECH) [97], tetraethoxysilane (TEOS) [97], and epichlorohydrin (ECH) [97].

1.3.1.2. Initiator, solvent and template leacher

The polymerization process requires an initiator to generate free radicals and initiate the polymerization reaction. Azobisisobutyronitrile (AIBN) is among the most commonly used initiators due to its mild fragmentation conditions and optimal decomposition temperature (approximately 65°C), making it compatible with most conventional solvents. Alternative initiators such as 2,2-dimethoxy-2-phenylacetophenone (DMPA) [98], and benzoyl peroxide (BPO) [99] have also been reported in the literature.

The solvent, or porogen, plays a dual role in IIP synthesis: it provides a medium for the polymerization reaction and influences the porosity of the final polymer. The choice of solvent directly affects the thermodynamic properties of the polymer, including its porosity, surface area, and adsorption efficiency. A well-structured porous network significantly enhances the accessibility of binding sites, improving target ion capture. Commonly used porogens include non-polar solvents such as toluene and chloroform, polar protic solvents like methanol and ethanol, and polar aprotic solvents such as dimethyl sulfoxide (DMSO), dimethylformamide (DMF), acetonitrile (AC), and dichloroethane [85, 100]. The polarity of the porogen is particularly critical, as it modulates interactions between the target ion and the ligand, thereby influencing the selectivity and final properties of the IIP. Aprotic solvents with low polarity are generally preferred,

as they minimize undesired interactions with the ligand-template complex, thereby stabilizing the complex during polymerization [101].

The final step in IIP synthesis involves template leaching, where a suitable reagent removes the ion template from the polymeric matrix, freeing the recognition sites. Strong acids such as HNO_3, HCl, or H_2SO_4 are commonly used for this purpose due to their high affinity for ligands, which facilitates efficient template removal [85, 102]. However, when acidic conditions are unsuitable due to the sensitivity of certain functional monomers, alternative leaching agents such as thiourea [86] and EDTA [86] can be employed to extract the target ion while preserving polymer integrity.

1.3.1.3. Templates used in IIPs

As mentioned earlier, IIT is a versatile technique that allows for the imprinting of various target ions within polymer matrices. These target ions range from metal ions—including heavy metals, alkali metals, and transition metals—to anions such as halides, oxyanions, and per- and polyfluoroalkyl substances (PFAS) [85]. Due to their robustness and reproducibility, ion-imprinted polymers (IIPs) offer tailored recognition elements that enable rapid detection of emerging water contaminants. During synthesis, functional monomers and ligands coordinate with the ion template to form a structured complex. Upon polymerization and subsequent template removal, these interactions create chemically and geometrically complementary binding sites. The rebinding mechanism is governed by ionic radius, charge density, and coordination geometry, as well as non-covalent forces such as electrostatic attraction, hydrogen bonding, and van der Waals interactions [100]. Table 1-2 provides a summary of recently developed IIPs with various ion templates.

Table 1-2 Some studies on imprinted polymers with ion templates in recent years.

Template ion	Monomer, ligand	Cross-linker	Solvent	Initiator	Washing agent	Format	Ref.
Arsenic	MAA, 1-VI	EDGMA	Methanol	AIBN	HCl	Particle	[88]
Arsenic	MAA	EDGMA	Methanol	AIBN	NaoH	Surface imprinting	[103]
Cadmium	MAA, Dithizone	EDGMA	Water	AIBN	HNO_3	Particle	[93]
Cadmium	2-VP, Diphenylcarbazide (DPC)	EDGMA	DMSO/ AC (1:1, v/v)	AIBN	HNO_3	Particle	[104]
Cadmium	MPS	TEOS	Ethanol/water (1.5:1)	-	HCl	Surface imprinting	[105]
Cobalt	8-HQ	ECH	Acetic acid, water	-	HNO_3	Particle	[106]
Copper	Itaconic acid	EDGMA	Methanol	AIBN	EDTA, HCl	Particle	[107]
Copper	MAA, Thiosemicarbazide (TCBZ)	EDGMA	Ethanol	AIBN	HCl	Particle	[108]
Lead	2-VP, DPC	EDGMA	Acetonititrile		HCl	Bulk	[109]
Lead	3aminopropyltrimeth-oxysilane (APTES), DPC	EDGMA	Acetone	AIBN	HNO_3	Surface imprinting	[110]
Zinc	MAA, Pentahydroxyflavone (PHF)	EDGMA	Ethanol-acetonitrile (2:1; v/v)	AIBN	HCl	Bulk	[111]
Nickel	2-VP, DPC	EDGMA	Acetonitrile	AIBN	HNO_3	Bulk	[112]
Potassium	MAA, dicyclohexano-18-crown-6 (DC18C6)	EGMA	DMSO, Acetonitrile	AIBN	HNO_3	Particle	[113]
Potassium	MAA, cryptand 222 (C222)	EDGMA	Acetonitrile	AIBN	HNO_3	Particle	[114]

The concept of IIPs was first introduced by Nishide et al. in 1976 [115]. However, the foundation for molecular imprinting was laid earlier in 1972 by Wulff et al. [116] and Takagishi et al. [117] who pioneered molecularly imprinted polymers (MIPs) based on enzyme-antibody interactions. Nishide et al. demonstrated that crosslinking poly(4-vinylpyridine) with 1,4-

dibromobutane, in the presence of different metal ions (Cu^{2+}, Co^{2+}, Fe^{3+}, Ni^{2+}, Hg^{2+}, or Zn^{2+}), allowed for selective rebinding of the respective ions [115].

IIPs can be synthesized using various polymerization methods. The most common approach is free radical polymerization, which includes bulk, precipitation, suspension, and emulsion polymerization [81, 85]. The characteristics of the synthesis methods are illustrated in Fig. 1-6.

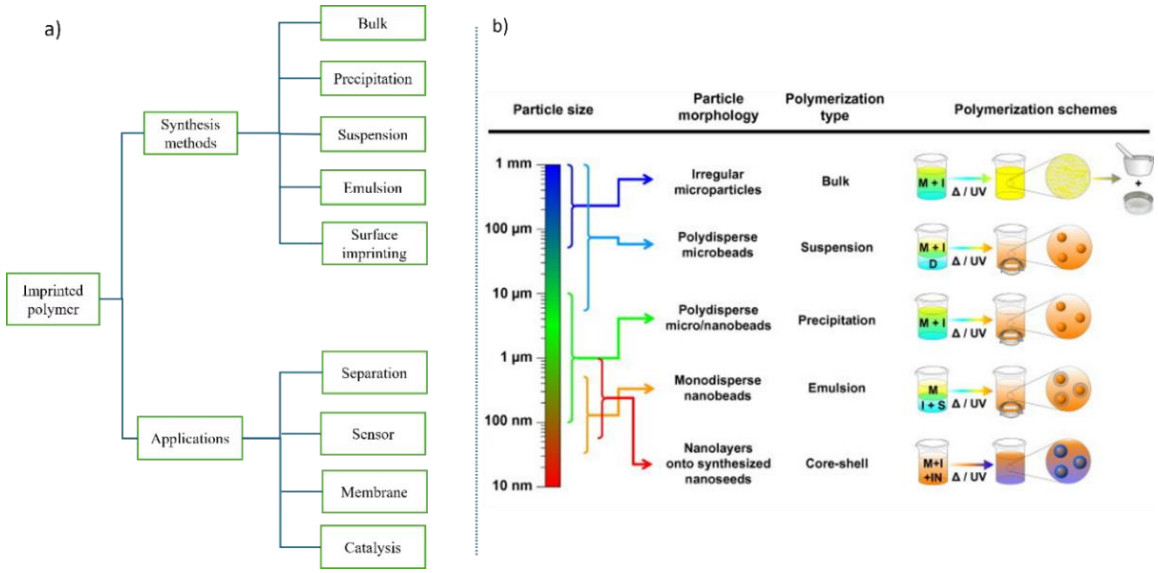

Fig. 1-6 IP synthesis (a) Synthesis and application environments of imprinted polymers [118] (b) Schematic illustration of different polymerization methods. Monomers (M); Initiator (I); Dispersing phase (D); Surfactant (S); Insoluble nanoseeds (IN). Reprinted from Ref. [119] with permission from Elsevier.

1.3.1.3.1. Bulk polymerization

Bulk polymerization is the simplest and most traditional method for IIP synthesis, requiring minimal specialized equipment [85, 100]. The template ion, functional monomer, crosslinker, and initiator are dissolved in a suitable solvent and polymerized. After polymerization, the bulk material is crushed, ground, and sieved to obtain IIP particles of the desired size. However, this process can destroy some binding sites and result in irregular particle shapes, which limits its

application in chromatography and separation technologies. To overcome these drawbacks, alternative polymerization techniques have been developed to produce IIPs in bead form using homogeneous or heterogeneous polymerization [85, 100].

1.3.1.3.2. Precipitation and dispersion

In precipitation polymerization, all reactants (monomers, ion templates, and initiators) are dissolved in a single-phase porogen solvent. Polymerization begins in a homogeneous solution, leading to the formation of insoluble polymer cores that precipitate and grow [85, 100]. Precipitation polymerization is the next commonly used method after bulk polymerization for the preparation IIP in particle form. This method enables precise control over particle size, allowing the synthesis of micrometer- and nanometer-scale IIPs. However, a significant limitation is the excessive use of porogen, requiring multiple purification steps to remove residual solvents and prevent leaching of the template ion.

Dispersion polymerization, a variation of precipitation polymerization, involves the use of stabilizing agents to prevent coagulation and improve control over particle morphology. This technique yields uniform polymer beads (~100 μm), but its widespread use is hindered by long reaction times and the need for additional purification steps [85, 120].

1.3.1.3.3. Suspension and emulsion polymerization

In suspension polymerization, the synthesis of IIPs occurs in the dispersed phase containing functional monomers, template ions, porogens, as well as initiators which can be described as a set of micro-reactors for executing local bulk polymerization [85, 100]. The process necessitates constant mechanical stirring for the particles to remain suspended in the continuous phase which contains the stabilizers. This technique produces micrometer-sized IIPs (250–550 μm) with

tunable porosity, controlled by the choice of porogenic solvents. To prevent template ion migration between the organic and aqueous phases, inverse suspension polymerization using a mineral oil dispersion phase is employed [85, 100].

In emulsion polymerization, the continuous phase is typically water, with hydrophobic monomers dispersed in water with the aid of an oil-in-water (O/W) emulsifier. The continuous phase has the initiators, which generate free radicals [85, 100]. In the reaction, a growing oil–water interface is produced as a result of the generation and growth of new polymer cores. A stabilization agent is needed, to prevent agglomeration of the developing nuclei. Reverse-phase emulsion polymerization (water-in-oil) allows for greater size control, enabling the production of uniform microspheres and nanospheres. However, the use of surfactants necessitates additional purification steps [85, 100].

1.3.1.3.4. Surface-Imprinting

Conventional IIP synthesis can result in deeply embedded template ions, making removal difficult and reducing affinity for the target species. Surface imprinting addresses these limitations by creating recognition sites on the material's surface, enhancing adsorption efficiency and selectivity [81, 85, 100]. Conventional IIP synthesis can result in deeply embedded template ions, making removal difficult and reducing affinity for the target species. Surface imprinting addresses these limitations by creating recognition sites on the material's surface, enhancing adsorption efficiency and selectivity [81, 85, 100, 121].

1.3.1.3.5. Other technologies

With advancements in IIT, novel strategies such as multiple functional monomers and dual/multiple template imprinting have gained interest [122]. The technology has also been

integrated with various applications, including separation membranes, catalysis, and electrochemical sensing [100, 121–123]. These emerging approaches enhance the efficiency and selectivity of IIPs, expanding their potential applications in environmental monitoring and beyond.

1.4. IIP-based electrochemical sensors for metal ion detection

Monitoring metal ions is of critical importance due to their potential negative impact on both the environment and human health [2, 124, 125]. Even trace amounts of certain metal ions can have severe consequences, necessitating the development of analytical methods capable of achieving low detection limits, even in complex matrices. Conventional techniques such as Atomic Absorption Spectroscopy (AAS) and Inductively Coupled Plasma Mass Spectrometry (ICP-MS) remain the gold standard due to their high accuracy and sensitivity. Their reliance on specialized instrumentation and centralized laboratories, however, can limit accessibility for frequent field monitoring. This has motivated complementary research into portable and cost-effective electrochemical sensors for trace metal ion detection.

Electrochemical sensors based on molecularly imprinted technology have already demonstrated high efficiency in quantifying organic pollutants [42, 95]. MIPs serve as highly selective receptors, significantly enhancing the sensitivity of coupled electrodes [43, 56]. The development of IIPs followed MIPs, specifically targeting the selective extraction of metal ions [83, 118]. Interest in the development of specific electrodes using IIPs for quantifying metal ions also growing [112, 126]. Like MIPs, IIPs are designed to selectively recognize a target ion, known as the template ion, which plays a key role in their synthesis. As earlier described, the typical procedure for IIP synthesis involves forming a complex between the template ion and a ligand molecule containing

at least one chelating group. This complex is then crosslinked to create a rigid three-dimensional network that maintains the shape and size of the binding sites after template removal (Fig. 1-4). Like MIPs, the selectivity of IIPs makes them particularly attractive as recognition elements for sensing applications.

For optical sensors, direct metal ion quantification via optical signals is challenging. Thus, IIP-based optical sensors often incorporate a fluoro-ionophore [127] or chromophore to generate or quench an optical signal. Alternatively, fluorescent nanoparticles such as quantum dots can be used [128, 129]. However, since most metal ions can be effectively quantified via electrochemical methods, such as voltammetry and potentiometry [51, 130], IIP-based electrochemical sensors do not require additional modifications for signal generation. Instead, IIPs act as highly selective receptors, enhancing sensitivity and selectivity. These sensors are particularly useful for analyzing complex environmental or wastewater samples, where interfering ions and matrix complexity present analytical challenges.

IIP-based electrochemical sensors leverage the selective binding properties of IIPs to improve metal ion detection, whether through potentiometry or voltammetry. In potentiometric sensors, IIP particles typically replace conventional ionophores in ion-selective electrodes (ISEs). For voltammetric sensors, IIPs function as selective accumulation sites for target metal ions [51]. Figure 1-7 illustrates various strategies for fabricating IIP-modified electrodes, using either IIP particles or thin films in electrochemical detection.

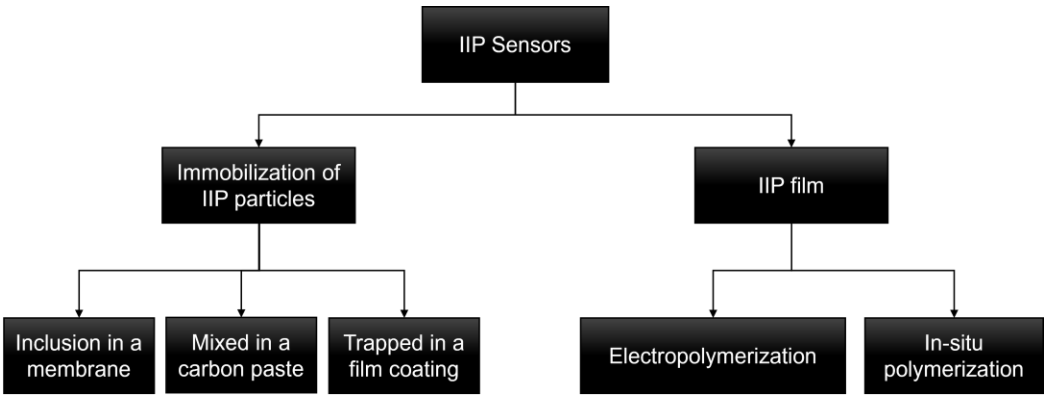

Fig. 1-7 Current methods for the fabrication of IIP electrochemical sensors [51].

1.4.1. Electrochemical sensors with IIP particles immobilized on electrode surfaces

Electrodes modified with IIP particles are typically fabricated as polymeric membranes containing a polyvinyl chloride (PVC) matrix, a plasticizer, and dispersed IIP particles. To improve ion transport and electrical characteristics, anionic additives, such as sodium tetraphenylborate (NaTPB) and potassium tetrakis(4-chlorophenyl) borate (KTpClPB), are incorporated. These additives reduce membrane impedance, promote charge transfer, and improve overall sensitivity [51]. The plasticizer serves a dual purpose: it imparts flexibility to the otherwise brittle PVC film, and, depending on its polarity, influences both ion mobility and recognition efficiency [131]. Typical formulations reported in the literature are summarized in Table 1-3 [132–135].

Table 1-3 Composition of membrane electrodes.

Target ion	IIP Particles (% composition)	Monomer (PVC) percentage (%)	Anion additive percentage (%)	Plasticizer (%) [a]	LOD (M)	Ref.
Copper	4	33.7	-	62.3 (DBP)	2e-6	[133]
Calcium	11	24	4 (NaTPB)	61 (DNP)	7.5e-7	[135]

Nickel	11	21.4	3 (NaTPB)	64.5 (DPB)	5e-6	[134]
Lead	4-8	26	1 (KTpCIPB)	65 (NPOE, DOS)	8.3e-8	[136]
Silver	9	27.6	1.9 (NaTPB)	61.3 (DNP)	1e-6	[137]
Arsenic	10.1	27.6	4 (NaTPB)	64.5 (DNP)	5e-7	[132]

[a]DBP = Dibutylphthalate, DNP = Dinonylphthalate, NPOE = o-Nitrophenyl Octyl Ether, DOS = Dioctyl Sebacate, KTpClPB = Potassium Tetrakis (4-Chlorophenyl) Borate.

Comparison of these compositions (Table 1-3) reveals that membrane formulation strongly influences detection performance. For instance, the lead (Pb^{2+}) – selective electrode exhibits the lowest LOD (8.3×10^{-8} M), a performance attributed to the synergistic use of dual plasticizers (NPOE, DOS) and the anionic additive KTpClPB. This combination not only enhances ion-exchange efficiency but also stabilizes charge balance within the sensing layer. In contrast, nickel (Ni^{2+}) and copper (Cu^{2+}) sensors have relatively higher LODs (5×10^{-6} M and 2×10^{-6} M, respectively), suggesting slower ion-exchange kinetics and less effective imprinting of their respective recognition sites.

The role of plasticizer is particularly evident: membranes based on DNP, e.g., calcium, silver, arsenic sensors generally outperform those using DBP. DNP's higher polarity may facilitate stronger ion solvation and binding, improving both selectivity and lower LODs. Similarly, the incorporation of anionic additives (NaTPB, KTpClPB) contributes to charge balance and conductivity, further enhancing sensor performance. For example, the calcium electrode,

containing 4% NaTPB, achieves a LOD of 7.5×10^{-7} M, markedly lower than nickel which lacks such an additive.

IIP particle loading (composition) also exhibits a non-linear effect. Moderate concentrations (~9–10%) yield favorable performance in silver and arsenic electrodes (LOD 10^{-6} - 10^{-7} M), whereas lower loading (~4%) produces mixed outcomes: excellent performance in lead but poorer sensitivity in copper. This suggests that while higher IIP content can improve recognition site density, excessive loading may compromise membrane homogeneity and ion transport pathways.

From an application perspective, these results highlight the adaptability of IIP-based membranes for specific sensing needs. Ultra-low limits of lead and arsenic are majorly relevant for environmental monitoring, aligning with stringent regulatory standards (e.g., WHO limit for lead at 4.8×10^{-8} M for drinking water). Conversely, electrodes with higher LODs (e.g., Ni^{2+} and Cu^{2+} may be more suitable in applications where concentrations are typically higher, such as for industrial effluents or biological fluids.

Another class of IIP sensors that have been used as ISE are Carbon Paste Electrodes (CPE). While they have been classified as liquid membrane type electrodes. Another class of IIP-based sensors, used as ion selective electrode, utilizes Carbon Paste Electrodes (CPEs), which, although classified as liquid membrane electrodes [87], differ significantly from PVC-based electrodes due to their primary composition of graphite carbon paste [138]. In IIP-CPEs, IIP particles replace conventional ionophores. These sensors are widely used due to their simple preparation: graphite is mixed with a binder (e.g., paraffin oil) and IIP particles using a mortar and pestle. To enhance electrode contact, high-surface-area conductive additives such as Single-Walled Carbon Nanotubes (SWCNT) [139] , graphitic carbon nitride nanosheets (g-C3N4) [140] or Graphene Nano Sheets (GNS) [141] are often incorporated.

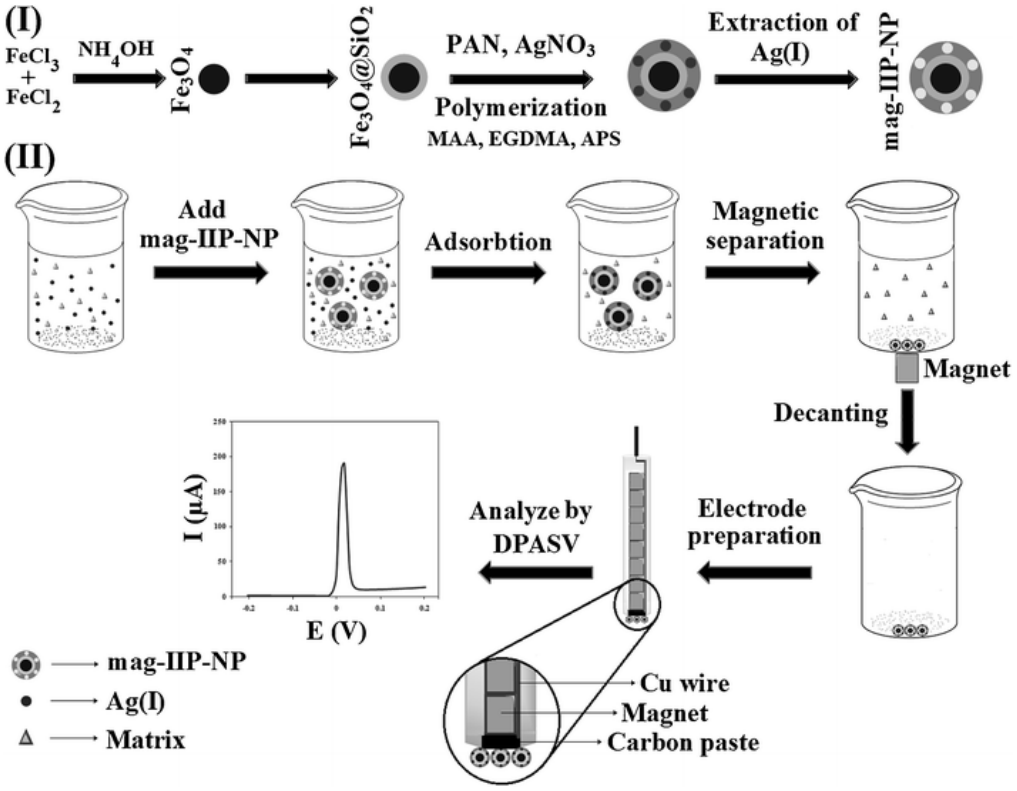

Fig. 1-8 Coupling a Carbon Paste Electrode and Magnetic IIP Nanoparticles for the selective adsorption and analysis of the target analyte. Reprinted from Ref. [97] with permission from Elsevier.

An innovative method for immobilizing IIP particles on electrodes was demonstrated by Ghanei-Motlagh et al. [97] who leveraged the magnetic properties of IIP-modified magnetic nanoparticles (MNPs). This approach enables the selective adsorption and electrochemical analysis of target ions by magnetically recovering IIP particles onto an electrode surface equipped with a magnet (Fig. 1-8). Unlike conventional CPEs, this method does not require mixing IIP particles into the carbon paste, allowing for easier cleaning and reuse.

In other studies, IIP particles have been directly cast onto electrode surfaces. Razmi et al. and Rajabi et al. both dispersed the IIP particles in a solvent, applied them on electrode surfaces and left them to dry [142, 143]. However, since IIPs can act as resistors, controlling polymer thickness

is crucial. To mitigate this issue, conductive additives such as multi-walled carbon nanotubes (MWCNTs) are often incorporated into the polymer matrix before application.

Additionally, some studies have explored the direct casting of IIP-modified magnetic nanoparticles onto electrodes, enhancing signal strength through increased surface area and adsorption capacity [95, 144]. A primary challenge with this approach is the potential loss of IIP particles during reuse or washing, which can affect reproducibility. To address this, Di Masi et al. [145] reported the functionalization of gold electrodes using a "grafting-to" method, where IIP nanoparticles were chemically anchored to a self-assembled monolayer (SAM) of cysteamine, ensuring strong polymer adhesion.

1.4.2. Electrochemical sensors with electrode surfaces modified with IIP film

A widely used technique for forming IIP films directly on electrodes is electropolymerization. This method involves immersing the working electrode in a monomer solution and applying cyclic potential scans to initiate polymerization, resulting in a polymer film on the electrode surface [146]. One key advantage of this approach is that the formed polymer film is conductive, facilitating electron transfer. Various studies utilizing this technique are summarized in Table 1-4, where conductive nanoparticles are often added to improve conductivity and surface area.

Table 1-4 Some metal ion sensors studies involving IIP electrode by electropolymerization.

Target ion	**Monomer**	**Detection method** [a]	**Mediator**	**LOD (M)**	**Ref.**
Copper	p-phenylenediamine	Potentiometry	-	2.7e-9	[147]
Copper	pyrrole/methyl red	DPASV	-	6.5e-9	[148]

Arsenic	p-phenylenediamine	CV	Au (nano-porous)	7.1e-12	[149]
Cadmium	pyrrole	SWASV	RGO	2.31e-9	[150]
Mercury	mercaptobenzotriazole	DPASV	Au particles/ SWCNT	8e-11	[151]

[a] DPASV: Differential Pulse Anodic Stripping Voltammetry, CV: Cyclic Voltammetry, SWASV: Square Wave Anodic Stripping Voltammetry.

Notably, arsenic detection was achieved an exceptionally low LOD (7.1e-12 M) when using gold nanoporous mediators, demonstrating the effectiveness of increasing surface area and enhancing electron transfer. Similarly, mercury sensors incorporating SWCNT and gold particles achieved impressive detection limits (8e-11 M), reinforcing the role of conductive nanomaterials in improving analytical sensitivity. By contrast, copper detection via potentiometry, without a mediator, exhibited a comparatively higher LOD (2.7e-9 M), highlighting the significance of mediator incorporation in lowering detection thresholds. These findings underscore the importance of tailoring electrode materials and fabrication methods to enhance sensitivity for specific target ions.

Another approach is in-situ polymerization, which involves spin-coating or dip-coating an electrode with a pre-polymerization mixture followed by polymerization via established free radical techniques. Table 1-5 presents studies employing in-situ polymerization for IIP sensor fabrication.

Table 1-5 Some metal ion sensors studies involving IIP electrode fabrication by in-situ polymerization.

Target ion	**Fabrication method**	**Additive**	**LOD (M)**	**Ref.**
Zinc	Spin-coating and in-situ polymerization	MWCNT	2.5e-10	[152]
Copper	Deposition of Graphene Oxide and prepolymer solution, polymerization with epichlorohydrin	Graphene oxide	1.5e-7	[153]
Copper	Spin coating of MWCNT and prepolymer solution mixture, followed by in-situ polymerization	MWCNT	2.5e-10	[152]
Cobalt	Coating electrode with MNP, followed by in-situ polymerization	-	1e-10	[154]
Gadolinium	Spin-coating and in-situ polymerization	-	1.21e-10	[155]

Unlike electropolymerized films, in-situ polymerized films are generally non-conductive. For this reason, most studies incorporate conductive additives, as seen in the use of MWCNT for zinc and copper detection (LOD: 2.5e-10 M) [152]. Here, Kumar et al. added MWCNT to the prepolymer solution, spin-coated it on the electrode and polymerized to make an IIP film. Other studies have explored different other conducting additives like graphene oxide [153], graphene [156] etc., either prior to or together with the prepolymer solution. The incorporation of graphene oxide (LOD: 1.5e-7 M) for copper detection resulted in a slightly higher LOD, suggesting that MWCNT may provide superior electrical conductivity in this context. Notably, cobalt sensors utilizing magnetic nanoparticles (MNP) achieved a remarkable LOD of 1e-10 M, highlighting the advantages of

leveraging magnetic properties to improve sensor efficiency. The trends in detection limits suggest that while in-situ polymerization methods benefit from structural flexibility, their reliance on conductive additives is crucial to maintaining low LODs.

In summary, IIP-based electrochemical sensors represent a promising class of analytical tools for metal ion detection. Their ability to selectively recognize target ions while enhancing electrode sensitivity makes them valuable in diverse applications, particularly in environmental monitoring and wastewater analysis. Ongoing research continues to refine fabrication techniques and improve sensor performance, broadening the scope of IIP-based detection systems.

1.5. Microfluidic IIP-based sensors for metal ion detection

Microfluidics technology enables precise control and manipulation of fluids within channels ranging from 5 to 500 μm in size. This technology has witnessed growing applications in chemistry, biology, and analytical biochemistry, owing to laminar flow, short diffusion lengths, and high surface-to-volume ratios that improve mass transfer and reaction efficiency [157]. By combining IIPs with microfluidic systems, portable, low-consumption and rapid detection platforms can be developed for a wide range of analytes, including environmental pollutants [1, 158, 159]. IIPs can be immobilized onto microchannel surfaces or microparticles, facilitating efficient target molecule capture and separation from complex mixtures. Microfluidic IIP-based sensors offer several advantages over conventional sensing methods, including enhanced sensitivity and selectivity via enriched surface interactions, improved reproducibility, reduced sample/ reagent consumption and shorter analysis times [158, 159]. These systems enable the creation of fast, automated, and self-contained detection platforms [158, 160], making them highly

versatile across various applications [160]. Despite the promise, reports on IIP-integrated microfluidics remain fewer than those using MIPs or bioreceptors, reflecting both fabrication challenges (robust immobilization, channel wetting) and historical emphasis on MIP platforms.

Zhou et al. developed a three-dimensional (3D) paper-based microfluidic sensor incorporating fluorescent ZnSe quantum dots for the detection of cadmium (Cd^{2+}) and lead (Pb^{2+}) ions [158]. Liquid-phase QD-IIPs were transferred to a glass-fiber paper, enabling capillary-driven, multi-channel operation (Fig. 1-9 I(A–F)). The device showed linearity from 1–70 µg/L (LOD 0.245 µg/L; ≈ 2.18 nM) for Cd^{2+} and 1–60 µg/L (LOD 0.335 µg/L; ≈ 1.62 nM) for Pb^{2+}. The sensor combined high selectivity and sensitivity with simple,low-cost fabrication and multiplexed readout, indicating potential for field monitoring.

Similarly, Qi et al. introduced a 3D origami ion-imprinted polymer microfluidic paper-based chip for multiplexed detection of Cu^{2+} and Hg^{2+} ions (Fig. 1-9, G (II)) [159]. The paper surface was modified by grafting CdTe quantum dots through amino processing, forming Cu^{2+} or Hg^{2+} IIPs and CdTe QD complexes. This led to fluorescence quenching of the quantum dots via energy transfer/inner-filter effects (Fig. 1-9, A-F (II)). The Cu^{2+} sensor exhibited good linearity from 0.11 to 58.0 µg/L with LOD 0.035 µg/L (0.55 nM), while the Hg2+ sensor showed 0.26–34.0 µg/L with LOD 0.056 µg/L (0.28 nM).

Across these optical microfluidic IIP applications, quantum-dot transduction is a primary driver of sensitivity, yielding sub-nanomolar to low-nanomolar LODs (Cu^{2+} = 0.55 nM; Hg^{2+} = 0.28 nM; Cd^{2+} = 2.18 nM; Pb^{2+} = 1.62 nM). This suggests a general design principle: pairing high-affinity IIP recognition with high-quantum-yield reporters in short optical pathlength microchannels can lower detection limits while preserving selectivity. The resulting performance aligns with trace-level environmental monitoring requirements, where ultra-low concentrations are critical.

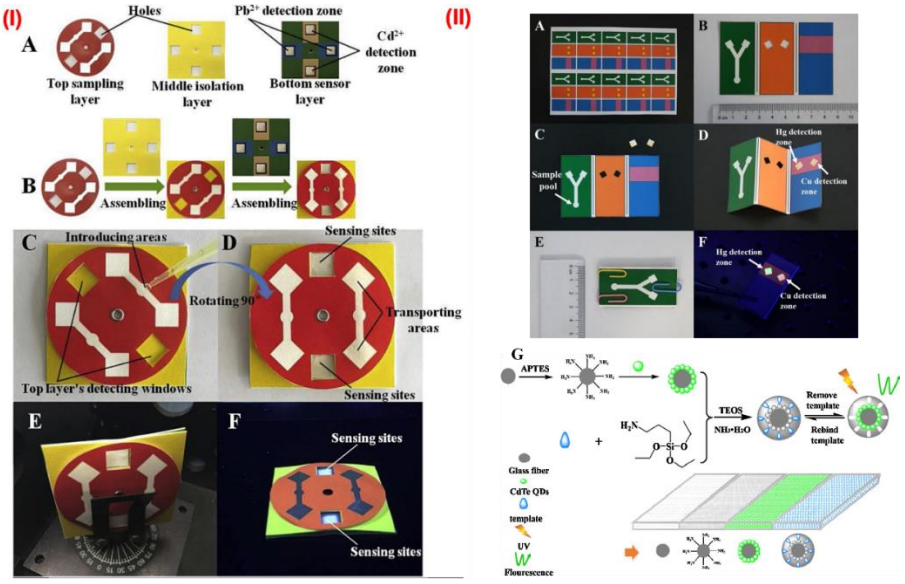

Fig. 1-9 (I) The fabrication and description of a microfluidic-based ion-imprinted optic sensor for Cd and Pb detection [158] and (II) (a-f) description and working (G) synthesis process of imprinted optic sensor for Cu and Hg detection [159]. Images adapted from Ref. [158, 159], with permission from Elsevier.

Wang et al. [161] also designed a rotary cloth/paper hybrid microfluidic analytical device (μCPAD) that integrates a cloth-based fluorescent sensing pad t with a rotary paper microfluidic manifold for simultaneous detection of Hg^{2+} and Pb^{2+} ions. The cloth provides mechanical robustness and durable QD/IIP anchoring, simplifying production. The three-layers stack with patterned hydrophilic channels and hydrophobic barriers, enables addressable multiplexing by rotation. Fluorescence quenching readouts achieved LODs of 0.18 μg/L (0.90 nM) for Hg^{2+} and 0.07 μg/L (0.34 nM) for Pb^{2+}. Compared with the origami device, μCPAD shows a slightly higher Hg^{2+} LOD (0.18 vs 0.056 μg/L) but comparable Pb^{2+} LOD (0.07 vs 0.335 μg/L), illustrating a common trade-off in microfluidic IIP design: mechanical stability and user-friendliness can modestly penalize ultimate sensitivity.

While these optical microfluidic platforms can achieve lower absolute LODs, their reliance on photoluminescent materials necessitates careful design considerations. Sensor stability, photobleaching resistance, and reproducibility across varying environmental conditions remain areas of ongoing research. Nonetheless, all these approaches demonstrate LODs well within environmentally relevant ranges, reinforcing the suitability of IIP-integrated microfluidics for trace metal ion monitoring in portable, field-deployable forms.

1.6. Scientific and technological gaps

A comprehensive review of the literature reveals extensive research on MIP, ISP and IIP sensor technologies. Despite this, critical scientific gaps remain that limit their broader application in microfluidic platforms for water quality monitoring.

1. Limited integration of IIPs in microfluidic electrochemical systems

While IIPs offer high selectivity for target ions, their integration into conventional (non-paper-based) microfluidic systems remains scarce. This is especially true in electrochemical platforms, where the few available studies rely on paper-based devices and optical detection methods [158, 159, 161]. The scientific community lacks a robust understanding of how IIPs behave when incorporated into rigid microfluidic systems using electrochemical readouts, which have advantages such as high sensitivity, selectivity, miniaturization potential, and compatibility with microfabricated electronic components, which enhance portability [149, 162]. Addressing this gap could significantly improve IIP-based sensing performance for metal ion detection in water quality monitoring.

2. Lack of research on free-standing or membrane-form IIPs within microfluidics

A review of current IIP electrochemical sensors indicates that current methodologies involve coupling the IIP layer with an electrode via electropolymerization, in-situ polymerization, particle coating, or film casting [51, 144, 163]. These methods often limit design flexibility, require complex fabrication procedures, pre-treatment steps for electrode modification, and limited control over the polymer morphology/thickness. There is a scientific gap in developing self-supporting, free-standing IIP membranes that can be spatially integrated within a microfluidic chamber without requiring direct bonding to electrodes.

3. Limited knowledge on the effect of synthesis conditions on IIP quality

Key parameters such as solvent selection, polymerization method, photoinitiator concentration, and curing conditions significantly influence the morphology and functionality of imprinted sites. Such influences have been scarcely studied especially in the context of on-chip IIP fabrication, leading to inconsistent performance in prototype devices.

4. Underutilization of flow dynamics to enhance sensing performance

Most existing research prioritize material modification – e.g., using carbon nanotubes (CNTs) or gold nanoparticles (AuNPs) to enhance sensing performance [50, 61, 163]. However, the role of fluid dynamics in enhancing mass transfer to the sensing surface is poorly understood. Optimizing flow channel geometry, membrane placement, and interaction time could significantly enhance detection limits, even with simpler sensing materials

Following these scientific issues, additional technological gaps remain that impede the translation of IIP-integrated sensors into field-deployable systems:

5. Complex and cost-intensive fabrication processes

Electrode modification with IIPs, especially when coupled with nanomaterials, introduces additional steps and cost, limiting scalability. A simplified, integrated fabrication strategy that minimizes the use of expensive materials while ensuring reproducibility is of high interest.

6. Scarcity of in-situ fabrication approaches for both IIPs and electrodes

There is limited evidence of workflows where both the sensing electrode and the IIP membrane are fabricated directly within the device (in-situ), using low-cost techniques. Such integration would significantly reduce variability, improve sensor uniformity, and enable batch production for deployment in water quality applications.

Based on the research gaps above, this dissertation seeks to address several key research questions in the field of IIP-based chemo-sensors for metal ion detection:

- How can an IIP be incorporated into microfluidics for electrochemical detection of metal ions in water?
- Can IIPs be synthesized as a standalone structure like a membrane within a microfluidic chip without coating on or modifying the electrode surface?
- Can both the IIP and electrodes be fabricated *in-situ* using simple and repeatable methods?
- How do different IIP compositions (e.g., template-to-monomer ratios, crosslinking densities) influence sensor performance?
- What is the effect of synthesis conditions (e.g. solvent choice, polymerization method, initiator type) on the functionality of IIPs?

- How do fluidic parameters (e.g., channel design, flow rate) influence analyte-membrane interaction and signal output in the integrated system?
- Can the developed IIP-integrated microfluidic platform be adapted for different target metal ions by modifying only the imprint templates?

1.6.1. Thesis Goals and Objectives

Addressing the identified research gaps and questions, this study aims to develop innovative methods for cost-effective, portable, highly sensitive, and selective detection of metal ions in drinking water. The research integrates IIP technology with microfluidics, leveraging the advantages of microfluidics—such as portability, precise flow control, cost efficiency, and rapid analysis—alongside the capability of IIP to create surface binding sites tailored to specific analytes.

A key innovation of this work is the synthesis and use of IIP as a standalone membrane within the microfluidic device. This approach eliminates the cost- and labor-intensive fabrication processes associated with conventional electrochemical sensors while allowing for precise control over membrane thickness and enhanced sensing performance. The integration of electrical and electrochemical detection is expected to optimally translate the physicochemical interactions between the IIP and target analytes into measurable outputs. Fig. 1-10 provides a schematic overview of the research, structured into three main objectives:

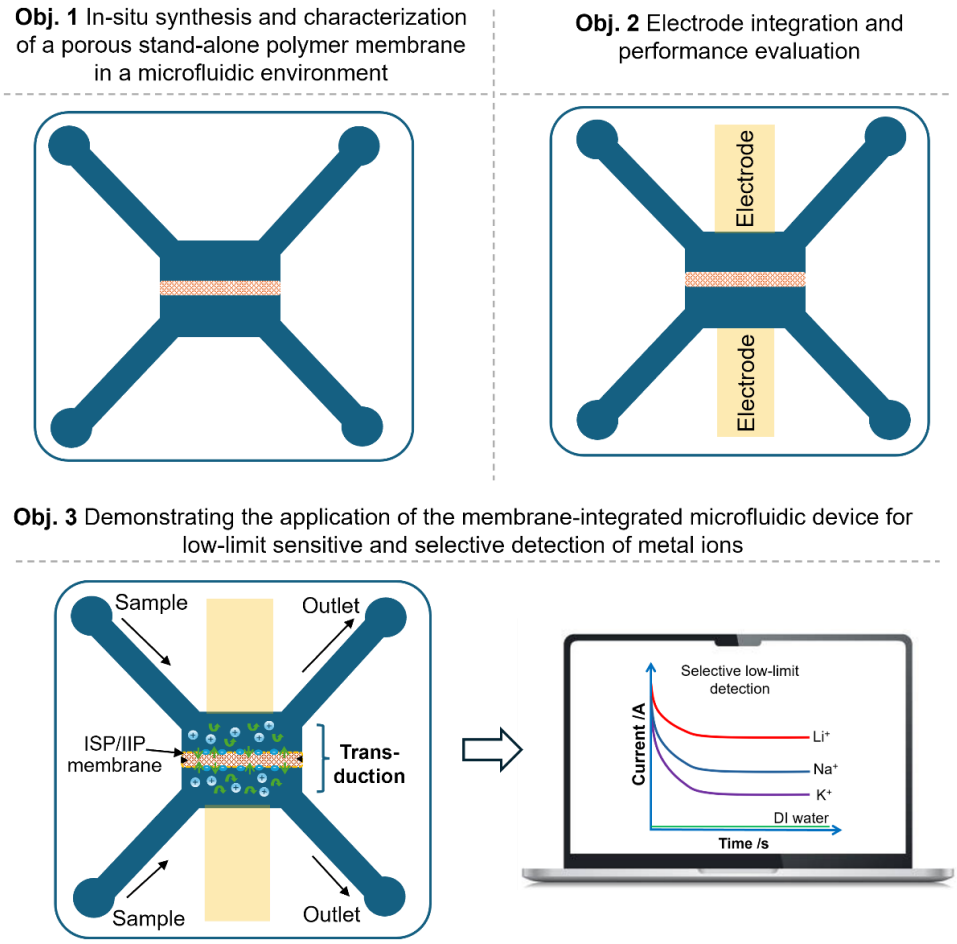

Fig. 1-10 Schematic description of the thesis research objectives.

Objective 1: In-situ synthesis of porous polymeric membranes and surface imprinting in microfluidic environments

This objective integrates the direct polymerization of membranes in microfluidic channels, optimizing their porosity and surface properties for selective permeability and ionic recognition. A key focus is on developing free-standing microporous membranes to allow flow continuity within the microfluidic environment and ensuring that these membranes are effectively incorporated into the microfluidic channels. The membrane will also subsequently be able to facilitate surface imprinting to enhance selective binding to target analytes. The ultimate goal is to test and optimize

these membranes for specific ion-sensing, leveraging their tailored physical and chemical properties for advanced microfluidic sensing applications.

Objective 2: Electrode integration and investigation of flow rate and analyte concentration on electrochemical response.

This phase involves the in-device synthesis of electrodes to ensure consistent electrical signals across the membrane. Systematic tests will be conducted to characterize the electrodes using methods such as voltage-current (C-I) and chronoamperometry characterizations, which will help establish the electrical stability parameters of the system. The study will also systematically assess how different the flow rates of the fluid, and the concentrations of the analyte impact the sensor's electrical and electrochemical behavior. This comprehensive analysis aims to better understand the operational parameters, sensitivity, and range of the sensor, which is critical for improving its reliability and accuracy in applications like water quality monitoring.

Objective 3: Demonstrating the application of the membrane-integrated microfluidic device for sensitive and specific ion detection.

This stage aims to validate the developed technology by demonstrating its application in detecting specific ions such as sodium, lead, and lithium in water. The objective involves rigorous testing and optimization to ensure the device's reliability, sensitivity, and selectivity. By utilizing the tailored properties of the membrane and the microfluidic setup, the goal is to achieve enhanced performance in ion detection, catering to applications such as environmental monitoring or industrial processes. This phase is crucial for verifying the effectiveness of the membrane-

integrated microfluidic device in addressing analytical challenges related to ion detection, with potential applications in environmental monitoring and industrial processes.

1.7. Thesis Outline

This thesis comprises seven chapters:

- **Chapter 1** introduces molecularly imprinted polymers (MIPs), ion-imprinted polymers (IIPs), and chemosensors, followed by a review of conventional IIP sensor platforms for metal ion detection, establishing the foundation for the research.
- **Chapter 2** details the methodologies and materials used to fabricate microfluidic devices and synthesize polymer membranes, including chemical synthesis, data collection, statistical analysis, and performance evaluation.
- **Chapter 3** discusses the in-situ polymer membrane and electrode synthesis, characterization, and performance evaluation for salinity monitoring (Objectives 1 & 2).
- **Chapter 4** transitions from ion-selective membranes to ion-imprinted polymer membranes. It presents the development and testing of a sodium-ion imprinted polymer (Na-IIP) sensor designed for selective sodium detection in water, addressing Objectives 2 and 3.
- **Chapter 5** explores the integration of a lead-ion imprinted polymer (Pb-IIP) membrane into the microfluidic device for the sensitive, selective, and low-limit detection of lead in water (Objective 3).
- **Chapter 6** investigates the incorporation of a lithium-ion imprinted polymer (Li-IIP) membrane into the microfluidic device for lithium detection in water (Objective 3).

- **Chapter 7** provides a summary of the thesis, highlighting its limitations and outlining future research directions.

1.8. Research Contributions

This thesis has produced 5 journal manuscripts co-authored by the Ph.D. candidate, as listed in the following sections. The content of Chapters 3 through 7 were culled from these manuscripts.

The first manuscript involved contributions from Dr. Alireza Zabihihesari (Year 1 mentor) and Dr. Razieh Salahandish (supervisory committee member). Dr. Zabihihesari contributed to conceptualization, methodology, investigation, data curation, formal analysis, validation, and manuscript revision. Dr. Salahandish assisted with methodology and manuscript review.

In the second publication, Dr. Zabihihesari contributed to conceptualization, methodology, data curation and manuscript revision, while Dr. Shapour Jafargholinejad supported investigation and data analysis.

The final three publications were co-authored solely with Prof. Rezai. Across all four works, I was primarily responsible for experimental design, data analysis, visualization, validation, and manuscript writing (original drafts and revisions). Prof. Rezai contributed to conceptualization, project oversight, methodology, investigation, analysis, supervision, manuscript review, funding acquisition, and resource provision.

1.8.1. Journal papers

- A.E. Oseyemi, A. Zabihihesari, R. Salahandish, P. Rezai (2025). Low-Level Salinity Monitoring in Drinking Water Using an Electrochemical Microfluidic Sensor with an Ion-Selective Polymer Membrane, Microchemical Journal 215 (2025) 114497
- A.E. Oseyemi**,** A. Zabihihesari, Shapour Jafargholinejad, P. Rezai (2025). Electrochemical Microfluidic Sensor with Sodium Ion-Imprinted Polymer Membrane for Sensitive and Specific Detection of Sodium in Water, Microchim Acta 192 (2025) 520.
- A.E. Oseyemi and P. Rezai (2025). Microfluidic Electrochemical Sensor with Lead Ion-Imprinted Polymer Membrane for Selective Trace Lead Detection in Water, Journal of Water Process Engineering 77 (2025) 108574.
- A.E. Oseyemi and P. Rezai (2025). Sensitive and Selective Electrochemical Detection of Lithium Using a Low-Cost Ion-Imprinted Polymer Based Microfluidic Sensor, IEEE Sensors Journal 25 (2025) 32074–32083.
- A.E. Oseyemi and P. Rezai (2025). Trace Detection of Perfluorooctanoic Acid in Water Using a Microfluidic Electrochemical Sensor with a Stand-alone Molecularly Imprinted Polymer. *[Submitted, Journal of the Electrochemical Society]*

1.8.2. Conference paper

- A.E. Oseyemi, P. Rezai. Low-Cost Lead-Ion Imprinted Polymer Membrane Microfluidic Sensor for Selective trace lead monitoring in water. *Proceedings from the 23rd International Conference on Solid-State Sensors, Actuators, and Microsystems (Transducers 2025), IEEE Explore 2025.(Peer reviewed)*

1.8.3. Conference presentations

- A.E. Oseyemi, P. Rezai. Low-Cost Lead-Ion Imprinted Polymer Membrane Microfluidic Sensor for Selective trace lead monitoring in water. *The 23rd International Conference on Solid-State Sensors, Actuators, and Microsystems (Transducers 2025). (Peer reviewed)*

- A.E. Oseyemi, A. Zabihihesari, P. Rezai (2025). Low-Cost Electrochemical Microfluidic Sensor with Lead-Ion Imprinted Polymer Membrane for Low-Limit Heavy Metal Detection in Water. *Natural Science and Engineering Research Council of Canada (NSERC), Collaborative Research and Training Experience Program (CREATE) Annual Summit, York University*

- A.E. Oseyemi, A. Zabihihesari, P. Rezai. Low-Cost Membrane-Integrated Microfluidic Electrochemical Sensor for Low-Limit Detection of Specific Salt Ions in Drinking Water. *The 28th International Conference on Miniaturized Systems for Chemistry and Life Sciences (µTAS 2024). (Peer reviewed)*

- A. Zabihihesari, A. Khalili, A.E. Oseyemi, Pouya Rezai. Electrothermal Coating of Bacteria Imprinted Polymer on Metallic Microwires. *The 28th International Conference on Miniaturized Systems for Chemistry and Life Sciences (µTAS 2024). (Peer reviewed)*

- A.E. Oseyemi, A. Zabihihesari, R. Salahandish, P. Rezai (2024). Low-Cost Membrane-Integrated Microfluidic Electrochemical Sensor for Low-Limit Detection of Specific Salt Ions in Drinking Water. *Centre for Research and Applications in Fluidic Technologies (CRAFT) Research Symposium. (Peer reviewed)*

- A.E. Oseyemi, P. Rezai (2024). Innovative Low-cost Lead-Ion Imprinted Polymer Membrane Microfluidic Sensor for Selective Heavy Metal Monitoring in Water. *WaterWise: Graduate Research Event, One WATER, York University. (Peer reviewed)*

- A. E. Oseyemi, A. Zabihihesari, P. Rezai (2024). Ion-selective polymer (ISP) membrane - Based Electrochemical Microfluidic Sensor for Selective Low-limit Water Salinity Monitoring. *31st Annual Conference of the Computational Fluid Dynamics Society of Canada (CSME/CFD2024). (Peer reviewed)*

- A.E. Oseyemi, A. Zabihihesari, P. Rezai (2024). Low-cost Membrane-Integrated Microfluidic Sensor for Low-Limit Detection of Specific Salt Ions in Drinking Water. *Natural Science and Engineering Research Council of Canada (NSERC), Collaborative Research and Training Experience Program (CREATE) Annual Summit, York University*.

- A.E. Oseyemi, A. Zabihihesari, P. Rezai (2024). Low-cost Ion-selective polymer (ISP) membrane – Integrated Electrochemical Microsensor for Low-limit Water Salinity Monitoring. *59th CENTRAL Canadian Symposium on Water Quality Research, Western University. (Peer reviewed)*

- A. E. Oseyemi, A. Zabihihesari, G. Kraft, and P. Rezai (2023). In-Situ Synthesis and Fluid Flow Characterization of Vertical Cell Imprinted Polymer (Cip)-based Membranes in Microchannels for Future Electrochemical Sensing Applications. *The 27th International Conference on Miniaturized Systems for Chemistry and Life Sciences (μTAS 2023). (Peer reviewed)*

- A. E. Oseyemi, A. Zabihihesari, G. Kraft, and P. Rezai (2023). 3D UV-Curable Molecularly Imprinted Polymer (MIP) Membrane for Microfluidic Biosensing Applications. *Micro Flow and Interfacial Phenomena (μFIP 2023) Conference. (Peer reviewed)*

1.8.4. Intellectual property

- P. Rezai, A. Zabihihesari, A. Doostmohammadi, A. E. Oseyemi, J. Brown, "Methods and systems for fabricating microstructures of imprinted polymers and integration with sensors for biological and chemical detection," *Patent Reference No. BIPL 160-031USP*.

1.9. Thesis Novelty and Contributions

This thesis introduces a novel platform that integrates stand-alone IIP membranes into microfluidic electrochemical sensors without requiring electrode surface functionalization. In contrast to conventional MIP/IIP strategies, which rely on direct polymer attachment to electrode surfaces and often involve laborious, time-consuming, and costly surface treatments, the proposed method employs in situ photopolymerization to generate a free-standing IIP membrane within designated sensing chambers. A key novelty of this approach is that separating the membrane from the electrode surface eliminates the formation of a non-conductive barrier layer on the electrode. This enables the use of non-conductive IIPs in electrochemical sensing, which would otherwise require incorporation of conductive polymers if coated directly on electrodes. This design broadens material choices, simplifies fabrication, reduces cost, and supports reproducible, scalable production. The resulting system enables rapid detection through capacitive response modulation and demonstrates adaptability across multiple analytes (Na^+, Pb^{2+}, Li^+) with low detection limits and high selectivity, even in complex sample matrices.

Chapter 2

2. Materials and Methods

In this chapter, we introduce the chemicals used in our experiments and explain the common methodologies between our various experiments. The chapter will continue with the data analysis and statistical tests performed in this thesis.

2.1. Materials

Common materials used for the fabrication of the membrane-integrated microfluidic sensors (Chapters 3 to 6) included polymethyl methacrylate (PMMA) sheets, polycarbonate (PC) sheets, and double-sided pressure-sensitive adhesive (PSA) tape, all procured from McMaster-Carr (Clear Scratch Cast Acrylic Sheet 8560K175, Clear Scratch and Impact-Resistant Polycarbonate 8707K161, and Optically Clear Mounting Tape 7602A58). Blunt dispensing needles and soft plastic tubing were also sourced from McMaster-Carr. Silver conductive paste (DuPont 5025, whose company later changed to Micromax™ 5025) was used for in-situ electrode fabrication and obtained from DuPont (Wilmington, Delaware, USA) or Insulectro (Lake Forest, CA, USA), respectively. The polymer matrix for all sensors was synthesized using methacrylic acid (MAA) as the functional monomer, ethylene glycol dimethacrylate (EGDMA) as the crosslinker, and 2,2-dimethoxy-2-phenyl-acetophenone (DMPA) as the photoinitiator. Dimethyl sulfoxide (DMSO) and acetonitrile were used as solvents. Supporting salts and electrolytes including NaCl, KCl, $NaNO_3$, and KNO_3 were obtained from Sigma Aldrich and used throughout for solution preparation and electrochemical testing.

For the **ISP membrane-integrated microfluidic sensor** (Chapter 3), additional monomers such as acrylamide (AAM), methyl methacrylate (MMA), and N-vinyl pyrrolidone (NVP) were used to enhance polymer structure and performance. Silver Conductor 5025 paste from DuPont was used in this chapter instead of Micromax™ 5025.

The **Na-IIP membrane-integrated microfluidic sensor** (Chapter 4) employed 15-crown-5 ether (15C5) as the ion-recognition ligand for sodium ions. No other unique chemicals beyond those listed in the general section were used.

The **Pb-IIP membrane-integrated microfluidic sensor** (Chapter 5) used AAM and 8-hydroxyquinoline (8-HQ) as part of the prepolymer formulation for Pb^{2+} ion imprinting. Lead nitrate ($Pb(NO_3)_2$) served as the template ion, and cadmium nitrate tetrahydrate ($Cd(NO_3)_2 \cdot 4H_2O$) and zinc nitrate hexahydrate ($Zn(NO_3)_2 \cdot 6H_2O$) were used for interference studies. Ethylenediaminetetraacetic acid (EDTA) was used as an eluting agent during post-polymerization washing.

The **Li-IIP membrane-integrated microfluidic sensor** (Chapter 6) incorporated 12-crown-4 ether (12C4) as the Li^+-specific ionophore. Lithium chloride (LiCl) was used as the imprinting template, and additional salts such as sodium sulfate (Na_2SO_4) were included during selectivity testing. EDTA was also applied during template removal.

2.2. Sample preparation

Stock solutions were prepared by dissolving raw metal salt powders in deionized (DI) water, followed by serial dilution to achieve the desired concentration ranges. For example, salinity test samples (0–800 ppm) were created by dissolving 200 mg of NaCl in 200 mL of DI water to form a 1000 mg/L (ppm) solution. This solution was then serially diluted with DI water while

maintaining a constant dilution factor to obtain concentrations of 800, 400, 200, 100, 80, 60, 40, 20, 10, 5, 1, 0.5, and 0.25 ppm. DI water was used as the blank solution in all experiments. The same methodology was applied for other target analytes (lead and lithium) following standard literature practices [144, 164].

2.3. Design and fabrication of microfluidic device

The microfluidic device comprises two primary components (Fig. 2-1): (i) an X-shaped fluid-handling module, featuring a central chamber for housing the Pb-IIP membrane and microchannels for sample flow, and (ii) two in-situ fabricated silver electrodes positioned on either side of the membrane. The chamber (3.5 × 3.0 mm²) has the membrane at its center, serving as a semi-permeable barrier to facilitate sample-membrane interaction. Anchoring structures ensure structural stability by securing the membrane to the chamber walls.

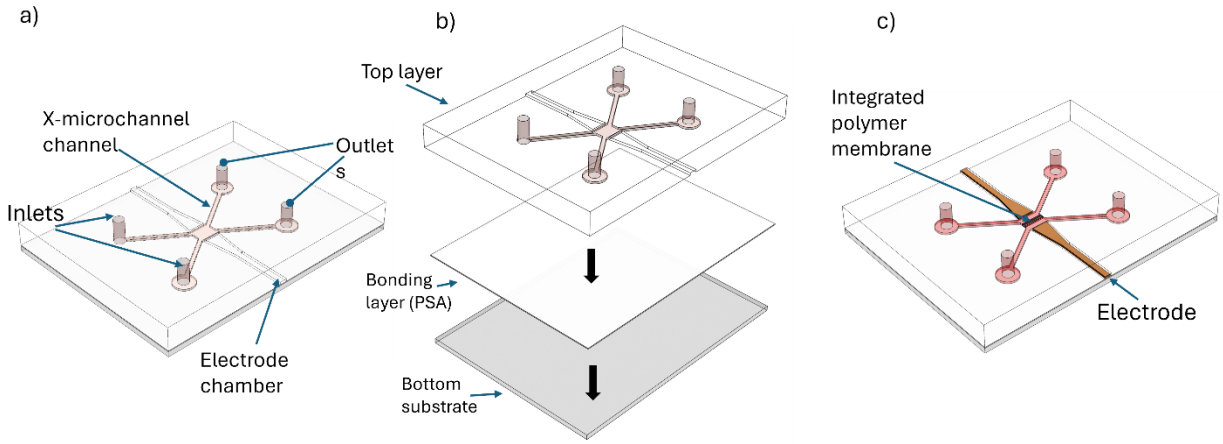

Fig. 2-1 Proposed microfluidic sensor design. (a) CAD model of microfluidic device highlighting key components, (b) exploded view showing structural assembly of individual layers, and (c) fully assembled device illustrating the integration of the polymer membrane with the electrode for sensing functionality.

The fabrication of the microfluidic device follows a systematic process. The device is composed of two primary layers: an upper layer containing microchannel networks and a bottom layer serving as a seal. The upper layer was fabricated from a 1.5 mm thick PMMA substrate, with microchannels milled to a depth of 200 µm using a CNC machine (MIKRON HEM 700U, Agno, Switzerland). PMMA was chosen for its durability, optical transparency, UV permeability, scalability, and chemical compatibility with the IIP membrane synthesis process. Following milling, the PMMA substrates were cleaned with ethanol and air-dried to remove residues before bonding.

Assembly was achieved by bonding the PMMA layer to a PC substrate using clear double-sided adhesive tape, with clamps applied for five minutes to ensure a firm bond. PC was selected for its structural strength and ease of manual handling. It also facilitated the use of PSA tape for sealing, offering a cost-effective alternative to additional PMMA layers that would require laser cutting. Once assembled, the device was integrated with electrodes and the membrane.

2.3.1. Electrode integration into the microfluidic device

The electrode fabrication process, illustrated in Fig. 2-2a, involved manually injecting DuPont™ 5025 (now Micromax® 5025) silver conductive paste [165] into the electrode chamber via designated injection ports. Micropillars (30 µm in diameter, spaced 50 µm apart) at the electrode-channel junction prevented the paste from entering the central microchamber during injection and ensured proper placement during curing. The device was then thermally cured at 75°C for 24 hours. Electrical and electrochemical characterizations of the electrodes are discussed in the results section.

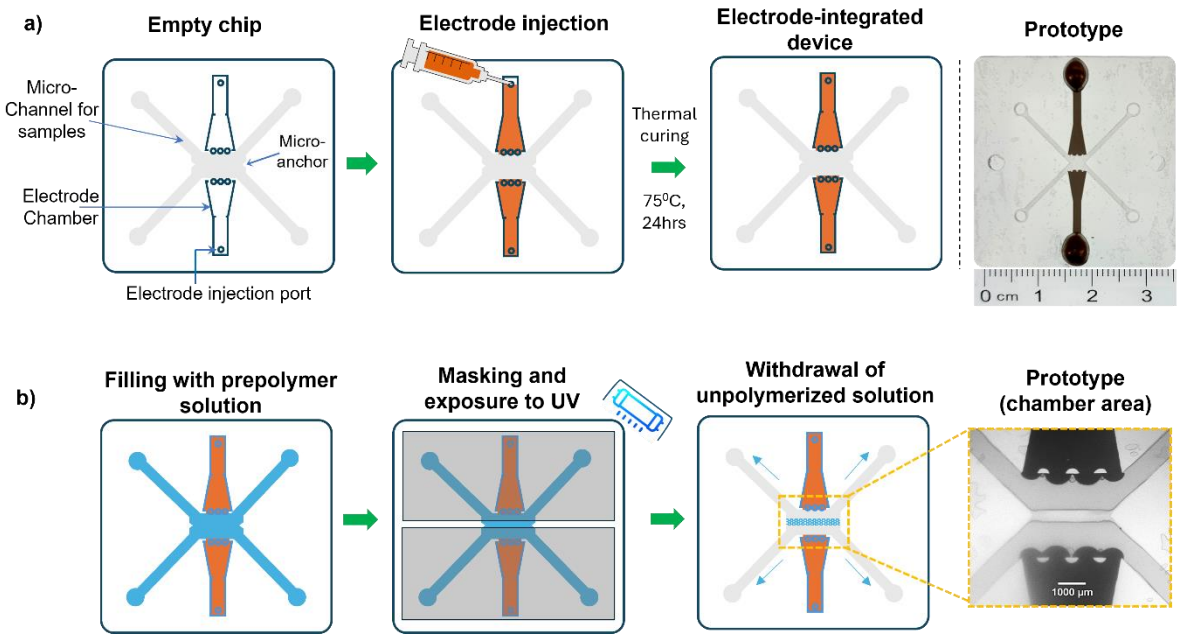

Fig. 2-2 Device fabrication. Sequential in-situ synthesis steps illustrating (a) electrode integration within the microfluidic device, followed by (b) photopolymerization of the ion-selective polymer membrane within the sensing chamber.

2.3.2. Integration of polymer membrane in the microfluidic device

The integration method for the stand-alone ISP/IIP/NIP membranes, while novel in the context of microsensor design, was adapted from a prior study that employed a microfluidic filtration system to isolate extracellular vesicles from blood [166]. The in-situ synthesis process (Fig. 2-2b) began with injecting the prepolymer solution into the channels to fully occupy the chamber. A precisely aligned shadow mask was then positioned over the chip, exposing only the designated membrane thickness to UV light. The chip, with the mask in place, was subjected to 365 nm UV light at an intensity of 15 mW/cm². Following an initial 5-minute UV exposure, the excess unpolymerized solution was carefully extracted using a syringe. A secondary 2-hour exposure ensured complete polymerization. After photopatterning, the device was rinsed with water to

remove residual components. Finalized devices were either immediately used for experimentation or stored filled with water for future use.

With the integration process established, attention was next directed to the formulation and synthesis of the ISP membrane tailored specifically for low-level salinity monitoring.

2.3.2.1. ISP membrane for low-level salinity monitoring.

ISP membrane synthesis involved the careful selection and incorporation of monomers, cross-linkers, porogens, and inhibitors to optimize membrane properties. The prepolymer solution included four monomers: MAA, AAM, NVP, and MMA, along with the cross-linker EGDMA, the photo-initiator DMPA, and a binary porogen system (DMSO and acetonitrile). The monomer (M): crosslinker (C): solvent (S) molar ratio was 1:6:1.2:12.3 (Table 2-1). Hydroquinone was added to inhibit unintended polymerization outside the exposed region, which could occur due to molecular diffusion or heat [167]. The formulation was inspired by prior work on Cell-Imprinted Polymer (CIP) for bacteria detection in water [168].

Table 2-1 ISP Membrane formulation.

	Functional Monomers				**Cross-linker**	**Solvent**	**Initiator**
Monomer	MAA	AAM	VP	MMA	EDGMA	Acetonitrile + DMSO	DMPA
Composition	(µl)	(mg)	(µl)	(µl)	(µl)	(µl)	(mg)
	180	21	4.2	5.2	570	2000	14
Mole (mol)	2.13e-3	2.95e-4	4.156e-5	4.864e-5	3.02e-3	0.03097e-2	5.463-4
Mole ratio (mM)	2.50				3.02	30.98	0.55
Mole ratio	1				1.2	12.3	

Each component in the prepolymer solution played a crucial role in defining both the functionality and structural integrity of the ISP membrane within the sensor. MAA, constituting 85.6% of the monomer composition, contains carboxylic acid (-COOH) groups that ionize in aqueous solutions, forming negatively charged carboxylate (-COO-) ions. These act as ion-exchange sites, facilitating electrostatic interactions with target cations. Methyl methacrylate (MMA), a hydrophobic monomer comprising 2.47% of the composition, provides mechanical strength and stability to the polymer matrix. N-vinylpyrrolidone (NVP), a hydrophilic monomer accounting for 2%, enhances water absorption and swelling properties, improving ion transport interactions. Acrylamide (AAM), making up 9.5% of the composition, contributes to the overall stability of the polymer matrix through its amide (-CONH2) groups, which influence ionic interactions within samples.

In our design, a binary solvent system of dimethyl sulfoxide (DMSO) and acetonitrile (3:1) replaced acetonitrile alone, as the latter caused severe etching of the microfluidic device's PMMA substrate during polymerization. This optimized solvent mixture ensured strong membrane adhesion while maintaining the necessary porosity and surface area. The approach aligns with findings from related studies confirming the ability of DMSO-based binary solvents to generate stable, high-surface-area monolithic polymers [169, 170]. Furthermore, the thermal initiator AIBN used in previous work was replaced with DMPA, a popularly used photo-initiator [98], to enable in-situ by photo-polymerization under UV light. Performance evaluation studies of the ISP membrane-integrated sensor including dose-response characterization (including other design variations of the membrane – e.g. without the MAA & AAM) , specificity, and selectivity tests were conducted on the device. The results of these studies are discussed in chapter 3.

2.3.2.2. Na-IIP membrane synthesis for low-limit specific monitoring of sodium in water

The Na-IIP membrane synthesis also involved the careful material selection, informed by previous studies on potassium (k+) ion-imprinted polymer [114, 171], being the closest available related studies at to our study, a there are very limited reports on Na-IIP. The selection of 15C5 as a ligand for Na^+ was guided by previous studies on sodium ion capture/transport [172, 173]. The IIP synthesis process is shown in Fig. 2-3.

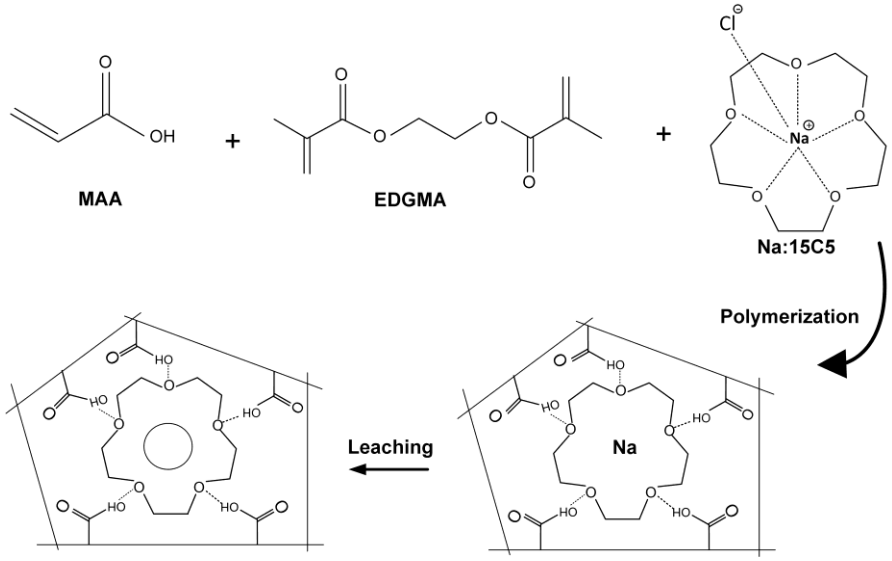

Fig. 2-3 Schematic illustration of the synthesis of Na-IIP.

For the prepolymer solution, 0.2 mmol of NaCl was dissolved in 40 µL of DI water and mixed with 0.2 mmol of 15C5 to form the Na:15C5 complex. This complex was then combined with 2 mmol of MAA, 5.3 mmol of EDGMA, 2.0 mL of DMSO, 0.5 mL of acetonitrile, and 14 mg of the photoinitiator DMPA. To prevent unwanted polymerization due to molecular diffusion or heat, 6.3 mg of hydroquinone was added as a polymerization inhibitor, following the same approach used for the ISP membrane synthesis. The in-situ synthesis of the Na-IIP membrane employed selective photo-polymerization, mirroring the ISP membrane integration method. Additionally, membrane-less and MAA and AAM-based NIP membrane-integrated configurations were fabricated for

comparative performance analysis. Following UV exposure, the imprinted membrane underwent in-situ washing using a syringe pump to infuse ethanol, followed by rinsing with DI water at a controlled flow rate. Elemental analysis of both the imprinted and non-imprinted membranes was conducted to assess structural and compositional characteristics. The performance evaluation of the Na-IIP membrane-integrated sensor included dose-response characterization, specificity, and selectivity assessments, with results detailed in chapter 4.

2.3.2.3. Pb-IIP membrane synthesis for trace detection of lead

The synthesis of the lead-ion imprinted polymer (Pb-IIP) membrane required carefully tailored material composition and an optimized washing solution. The Pb-IIP formulation was designed based on established protocols [174, 175], involving complex formation with 8-hydroxyquinoline (8-HQ) and polymerization with MAA and EDGMA. The synthesis process is illustrated in Fig. 2-4.

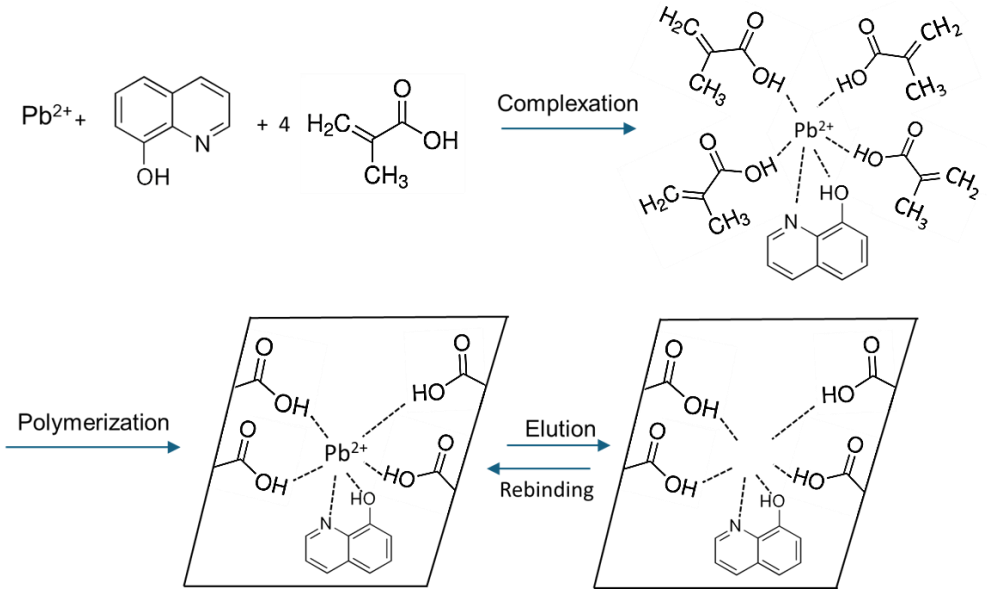

Fig. 2-4 Schematic representation of the Pb-IIP synthesis process.

To prepare the prepolymer solution, 0.1 mmol of $Pb(NO_3)_2$, serving as the template, was dissolved alongside 0.1 mmol of 8-HQ in 2 mL of a binary solvent mixture of DMSO and acetonitrile (3:1 ratio) within a conical tube. Once fully dissolved, 0.4 mmol of MAA as the functional monomer and 320 µL of EDGMA as the cross-linker were introduced. The solution was mixed thoroughly using a vortex mixer (Vortex-Genie 2 Mixer, Scientific Industries, SI-0236) to ensure homogeneity. Following this, 14 mg of the photoinitiator DMPA and 6 mg of a polymerization inhibitor were added, consistent with the procedures followed for the ISP, Na-IIP, and Li-IIP membranes. The solution was vortex-mixed again for approximately one minute until complete dissolution was achieved. To prevent premature photopolymerization, the conical tube was sealed and wrapped in aluminum foil to shield it from light exposure. The prepared Pb-IIP prepolymer solution was then introduced into the microfluidic device and subjected to selective photopolymerization under UV light, forming the imprinted membrane within the chip. Post-polymerization, an in-situ washing process was carried out using 0.5 M EDTA [80] to extract the lead template ions, followed by a DI water rinse to remove any residual organic solvents (Fig. 2-4). The imprinted and non-imprinted membranes were subsequently analyzed for elemental composition, and performance evaluation studies—including dose-response characterization, specificity, and selectivity assessments—were conducted, with results presented in chapter 5.

2.3.2.4. Li-IIP membrane synthesis for trace detection of lithium

The synthesis of the lithium-ion imprinted polymer (Li-IIP) membrane followed a systematic approach similar to that of the Na-IIP and Pb-IIP membranes, requiring careful selection and integration of functional and crosslinking monomers, a complexing ligand, porogens, and polymerization inhibitors to achieve the desired membrane properties. The material selection was

informed by previous research on lithium recovery from aqueous solutions using Li-IIPs [176]. We selected 12-crown-4 (12C4) as the complexing agent for lithium (Li^+), guided by multiple studies demonstrating the superior selectivity of 12C4 and its derivatives—such as benzo-12-crown-4 (B12C4), 2-methylol-12-crown-4 (2M12C4), and 2-(allyloxy)methyl-12-crown-4 (2AM12C4)—due to their cavity sizes, which closely match the ionic radius of lithium [176–180]. The synthesis process is depicted in Fig. 2-5.

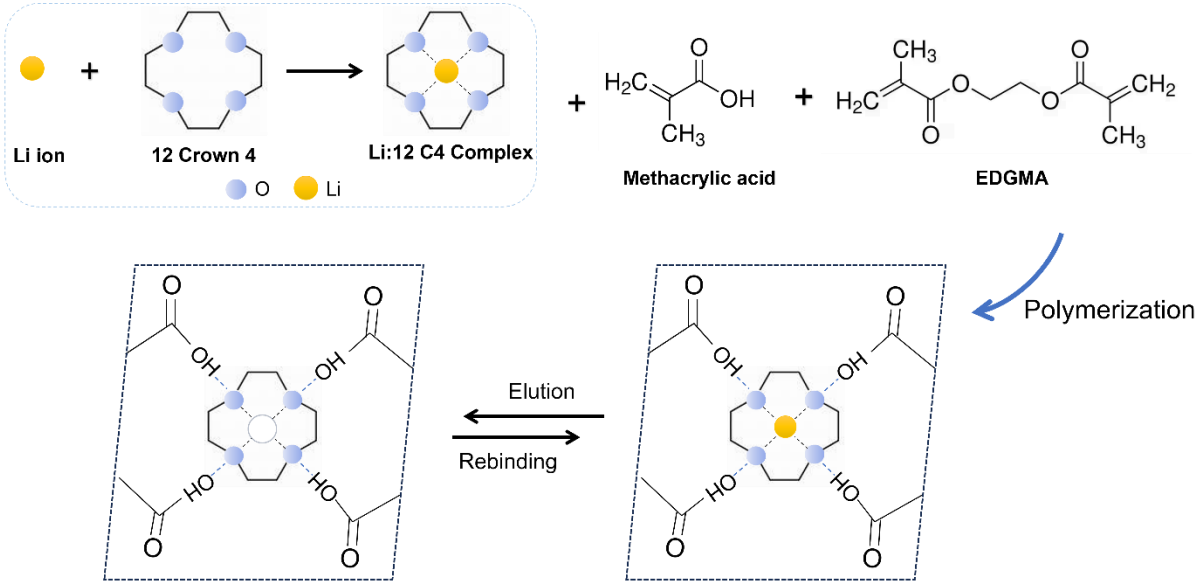

Fig. 2-5 Schematic illustration of the Li-IIP synthesis process

For the preparation of the Li-IIP prepolymer solution, 0.1 mmol of LiCl was dissolved in 2.0 mL of a binary solvent mixture of DMSO and acetonitrile (3:1 ratio). To this solution, 0.5 mmol of MAA as the functional monomer and 2 mmol of EDGMA as the cross-linker were added, maintaining a template:monomer:cross-linker ratio of 1:5:20. Additionally, 29.8 µL of 12C4 was incorporated as the selective lithium-binding ligand.

To facilitate UV-induced polymerization, 14.1 mg of DMPA was added as the photoinitiator, along with 6.3 mg of hydroquinone to suppress undesired polymerization outside the targeted exposure

region [166]. This formulation followed the same photopolymerization protocol as previously described for the ISP and Na-IIP membranes. Following polymerization, the imprinted membrane underwent an in-situ washing process with 0.5M EDTA and DI water to remove template ions and unreacted monomers. The washing procedure involved controlled infusion of ethanol via a syringe pump, followed by a DI water rinse to eliminate any remaining organic residues. Post-washing, elemental analysis of both the imprinted and non-imprinted membranes was performed. Additionally, performance evaluations—including dose-response characterization, specificity, and selectivity tests—were conducted on the integrated sensor, with findings discussed in chapter 6.

2.4. Experimental Setup and Procedures for Electrochemical Measurements

2.4.1. Experimental setup for chronoamperometric measurements

The experimental setup for chronoamperometric measurements is illustrated in Fig. 2-6a. A syringe pump (Legato 110, KD Scientific Inc., USA) was employed to deliver samples at a controlled flow rate into the microfluidic sensor, which was positioned under an upright microscope (Leica M125 C, Leica Inc., Canada). The sensor's outlets were connected to a waste reservoir to ensure proper fluid disposal. A portable potentiostat (PalmSens4, De Indruk, Netherlands) was interfaced with the electrodes of the microfluidic sensor and linked to a computer running the manufacturer’s software (PSTrace) for signal acquisition, control, and analysis. Fig. 2-6b provides a schematic representation of the fluidic and electrical connections, illustrating the integration of the working electrode (WE), reference electrode (RE), and counter electrode (CE)

with the potentiostat and computer system. The setup also included a dual-channel syringe pump to enable simultaneous sample delivery to both inlets of the microfluidic chip.

Electrochemical measurements involved two primary stages: the washing/blank stage and the sample testing stage. The washing stage was essential for sensor stabilization before sample introduction. For ISP membrane-integrated sensors, DI water was continuously flowed through the system to remove any residual, unreacted monomers. In the case of IIP-based sensors, the washing protocol involved an initial rinse with a leaching solution to remove template ions, followed by DI water to eliminate excess reagents. In either case, DI water was allowed to flow for 5–10 minutes until the chronoamperometric current reached a stable baseline close to zero, indicating that the sensor was ready for sample testing.

During the sample testing stage, analyte solutions were introduced in increasing concentrations, starting from the lowest and progressing to the highest. Each concentration was tested in triplicate to ensure reproducibility and accuracy. The collected data was used to construct a dose-response curve, which is discussed in detail in the subsequent section. The same two-stage procedure was followed for additional tests assessing specificity, interference, and selectivity.

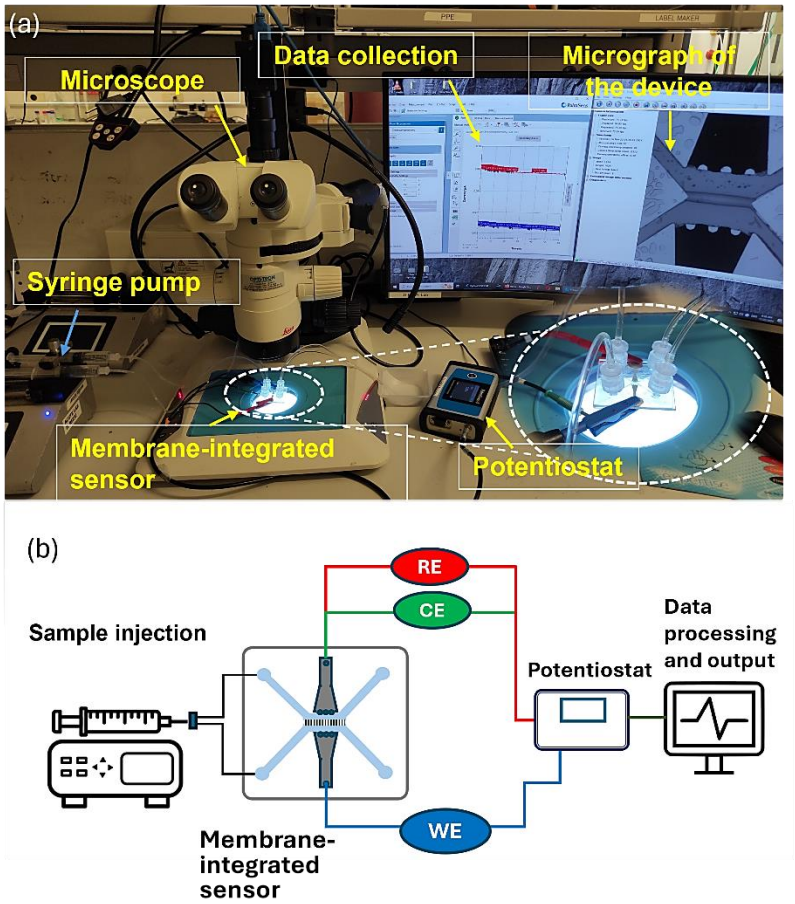

Fig. 2-6 (a) Experimental setup for testing ISP/IIP microfluidic sensors, showing the instruments used for sensor characterization. (b) Schematic of fluidic and electrochemical connections, depicting sample injection, potentiostat integration, and data acquisition.

2.4.2. Data analysis for sensor characterization

Chronoamperometric measurements were performed using a step voltage of 0.6 V, a time interval of 0.1 s, and a total run time of either 60 or 120 s. This method was selected due to its capability to generate precise, time-resolved current measurements, facilitating detailed analysis of the sensor's electrochemical behavior [147, 181]. The 0.1 s time interval ensured frequent and consistent sampling of the current response, capturing the kinetics of the electrochemical

interactions. A 120 s run time allowed sufficient data collection to observe changes in current over an extended period, enabling steady-state conditions to be reached.

All statistical analyses were conducted using Microsoft Excel 365, GraphPad Prism 9.5.1, and Lab Origin 2024. Dose-response curves were plotted as linear x-y graphs or semi-logarithmic (x-log, y-linear) plots, depending on the data characteristics. Where appropriate, standard linear as well as non-linear curve-fitting models, such as the Power Law Model and Power Model, were employed to improve data representation.

The LODs and LOQs were determined using the three-sigma (3σ) and ten-sigma (10σ) methods, respectively, based on the dose-response curve. The LOD was calculated as the blank readout current (I_{DI}) plus three times the standard deviation of the blank measurement (σ_{DI}), while the LOQ was defined as I_{Blank} plus ten times the standard deviation (σ_{Blank}). The corresponding analyte concentrations for these current values were then extrapolated from the dose-response curve, establishing the sensor's detection and quantification limits.

Sensor linearity was assessed by fitting a regression line to the dynamic range of the dose-response curve and analyzing the coefficient of determination (R^2). Specificity, interference, and selectivity studies were visualized using bar charts, with statistical analyses conducted using t-tests and one-way ANOVA to determine significant differences. This comprehensive analytical approach ensured a robust evaluation of the sensor's sensitivity, selectivity, and overall performance in detecting and quantifying target metal ions.

2.4. Working principle of the membrane-integrated microfluidic sensor

The sensing mechanism of the ISP/IIP-integrated microfluidic sensor is hypothetically based on a non-Faradaic capacitive detection principle. We hypothesize that the measured signal arises from three coupled effects: (i) electrokinetic-driven ion transport across the channel width (lateral electromigration), (ii) template-specific interaction within the free-standing polymer membrane, and (iii) modulation of the electrical double layer (EDL) at the electrode–electrolyte interfaces, yielding a transient displacement current.

When a step voltage is applied between the two laterally opposed silver electrodes, an electric field is established across the width of the sensing chamber. This field drives ions laterally: in one chamber ions are pushed toward the membrane, while in the opposite chamber they are driven away from it. Because the bulk solution is homogeneous and the sensing chambers are narrow and straight, no diffusion or pressure-driven gradients are invoked in this description, respectively.

Within the central sensing chamber, the free-standing porous membrane presents recognition sites (templated binding sites and functional groups such as carboxylates from MAA) that preferentially bind the target ion (e.g., Na^+, Pb^{2+}, Li^+). Under the lateral field, selective interaction of target ions with these sites adjusts the local ionic environment adjacent to the electrodes and the membrane. When the voltage step is applied (e.g., 0.6 V), EDL charging dominates, and a transient capacitive current is produced that can be expressed as:

$$I\ (t) = C.\frac{dV}{dt}$$

Where C = total effective capacitance (dominated by EDL) and $^{dv}/_{dt}$ is rate of change of voltage over time.

This transient capacitive current is highly sensitive to ion concentration and the local ionic environment near the membrane, enabling selective, non-Faradaic detection of the target analyte.

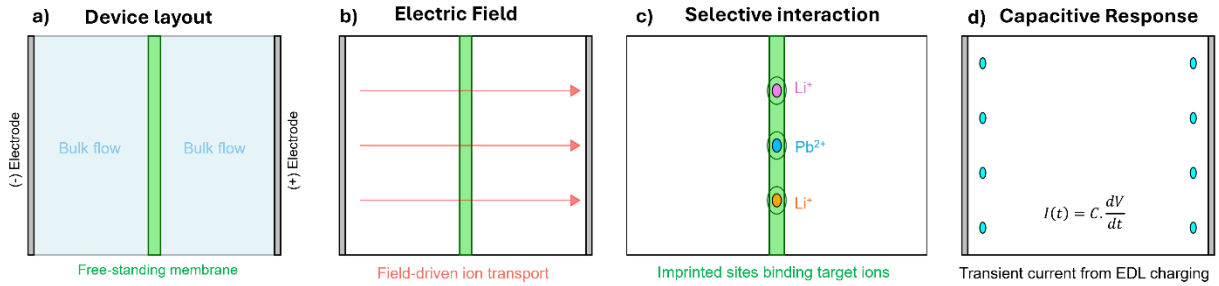

Fig. 2-7 Working principle of the membrane-integrated microfluidic sensor. (a) Device layout showing laterally opposed silver electrodes and a free-standing ion-selective polymer membrane in the central sensing chamber. (b) Application of a step voltage generates an electric field across the channel width, driving ions laterally. (c) Target ions (e.g. Na^+, Pb^{2+}, Li^+) selectively interact with templated recognition sites. (d) Redistribution of charges at the electrode–electrolyte interface leads to electrical double layer (EDL) charging, producing a transient capacitive current.

The illustration summarizes how the applied electric field laterally drives ions across the sensing chamber toward or away from the stand-alone membrane. Within the membrane, recognition sites selectively interact with the target analyte, influencing the local ionic environment at the electrode interfaces. This interaction alters the effective capacitance of the electrical double layer, giving rise to the transient displacement current. The schematic complements the preceding description by visually linking field-driven transport, selective capture, and capacitive signal generation in the integrated sensor.

This hypothetical mechanistic framework, which requires future validations, underpins the sensor performance demonstrated in later chapters and provides the foundation for evaluating material choices, device fabrication, and experimental results.

Chapter 3

Low-Level Salinity Monitoring in Drinking Water Using an Electrochemical Microfluidic Sensor with an Ion-Selective Polymer Membrane[1]

3.1 Introduction

This chapter entails the first, second, and third objectives of this thesis, covering the design, fabrication, characterization, and application of an electrochemical microfluidic sensor integrated with an ion-selective polymer (ISP) membrane for low-level salinity monitoring in drinking water. The ISP membrane, synthesized in situ within a PMMA-based chip, enables selective detection of Na^+ ions through functional group interactions that modulate the electrochemical signal. Chronoamperometry was used to evaluate the sensor's sensitivity, selectivity, and detection limits across different salts and concentration ranges, with and without the ISP membrane. By comparing performance metrics and validating the sensor using municipal tap water, this chapter demonstrates the feasibility of using ISP-integrated microfluidic platforms for sensitive, low-cost, point-of-need salinity testing.

[1] The contents of this chapter are adapted from our first manuscript: A.E. Oseyemi, A. Zabihihesari, R. Salahandish, P. Rezai. Low-Level Salinity Monitoring in Drinking Water Using an Electrochemical Microfluidic Sensor with an Ion-Selective Polymer Membrane, Microchemical Journal 215 (2025) 114497

3.2 Results and Discussion

3.2.1 Localized photopolymerization of the ISP membrane

We characterized the fabrication process of the ISP membrane in devices made of PMMA (Fig. 3-1). Using photomasks of different opening sizes ranging from 100 µm to 600 µm in width, we aimed to achieve the target corresponding membrane widths.

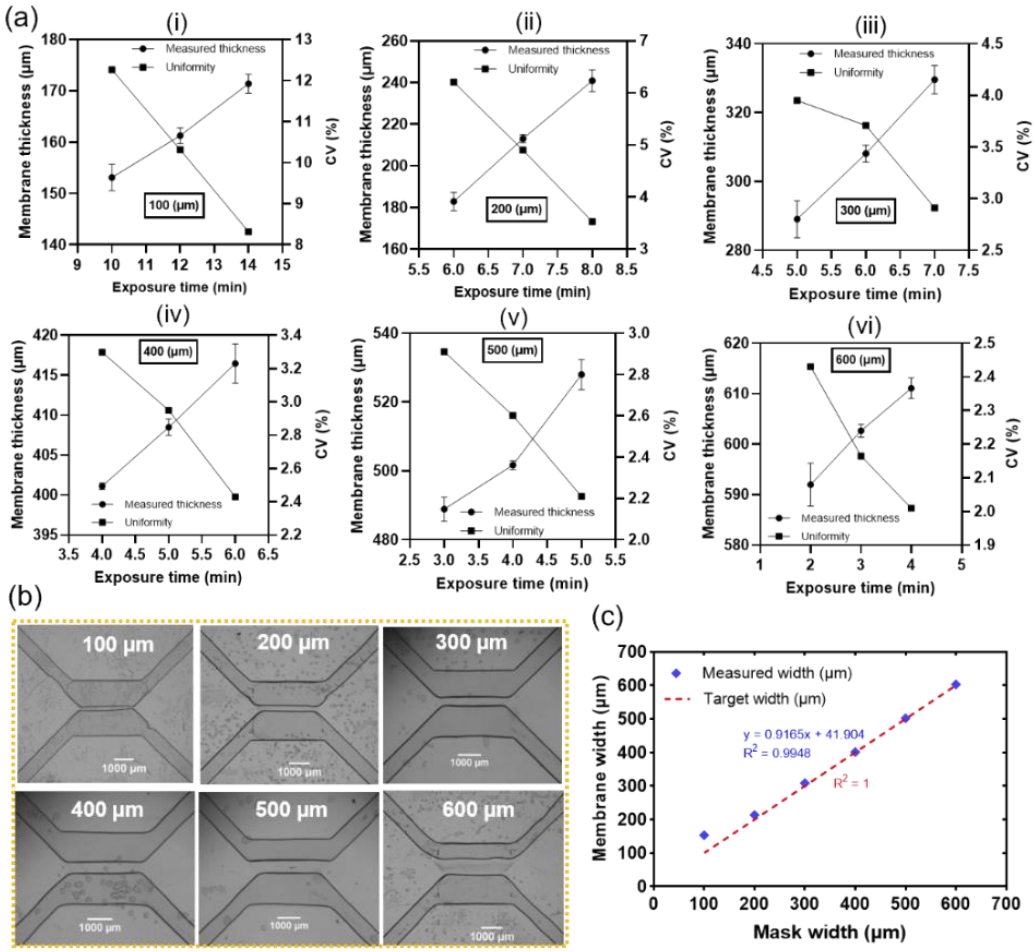

Fig. 3-1 Characterizing the localized photopolymerization of the ISP membrane in the microfluidic device. (a) Exposure time and uniformity characterization; (b) Fabricated membranes with different widths in the range of 100 to 600 µm; (c) Comparison of measured and targeted membrane thicknesses.

Initially, we investigated the minimum time required to achieve a full anchor-to-anchor length of the membrane in the chamber (Fig. 3-1a). For a target membrane thickness of 100 μm, we found that a minimum of 10 minutes was necessary, followed by 6, 5, 4, 3, and 2 minutes for membrane widths of 200, 300, 400, 500, and 600 μm, respectively, as summarized in Fig. 3-1a i-vi. The observed decrease in required exposure time with increasing membrane widths can be explained by improved light diffusion and intensity over larger surface areas, enhancing uniform polymerization. Additionally, enhanced cross-linking dynamics from better light penetration and a slight increase in local temperatures due to larger exposed areas contribute to faster curing. Conversely, narrower widths may encounter shadowing effects, where light scattering at the edges lowers curing efficiency, necessitating longer exposure times. These insights highlight the necessity to tailor UV exposure times to optimize the polymer curing process according to membrane width, ensuring robust mechanical stability and material integrity in different sensor designs.

We also investigated the correlation between the photomask and membrane widths, observing minimal variations ($< 7\%$) for mask widths ≥ 200 μm (Fig. 3-1b and 4c). However, larger variations were noted for 100 μm mask width (Fig. 3-1b) such that the resulting membrane had a thickness of 153±19 μm. This demonstrated an improved control over the membrane width with increasing membrane thickness. We attempted a smaller membrane thickness with a 50 μm mask width but could not obtain a full anchor-to-anchor membrane length across the chamber even under long exposure times.

We quantified the thickness uniformity of membranes synthesized using different mask widths (Fig. 3-1a). A lower CV% suggests that measurements are less variable, indicating greater uniformity and control over the synthesized membrane thickness. The thinnest membrane with a mask width of 100 μm (membrane width of 153±19 μm) exhibited the lowest uniformity

(maximum variation in thickness) with $\mathrm{CV} = 12\%$. It was observed that thicker membranes displayed better uniformity, as evidenced by the 600 μm thick membrane having the lowest variation ($\mathrm{CV} = 2\%$). Based on these results, we selected the 300 μm membranes for further experiments, as it offered an optimal balance of structural reproducibility and functional suitability for ion exchange and electrochemical detection (more discussion in the following section).

3.2.2. Effect of flowrate on sensor's electrochemical response at different salt levels

The research aimed to observe how the interplay between the dominance of diffusive or convective flow of sample ions influences the stability of electrochemical behavior. Higher flow rates can enhance convection and suppress diffusion in microfluidic devices. Therefore, we investigated the impact of different flow rates on the electrochemical behavior of the ISP membrane-integrated microfluidic device at various NaCl salt concentrations. Using chronoamperometry readouts for NaCl concentrations ranging from 1 to 100 ppm at total flow rates ($Q_{total} = Q_{inlet1} + Q_{inlet2}$) ranging from 100 to 1600 μL/min, we determined the optimal flow rate that ensured the most reliable and efficient detection, highlighting the intricate relationship between fluid behavior and electrochemical response within the device. We defined our optimal flow rate as the minimum required to obtain negligible readout signal deviation, across all concentrations.

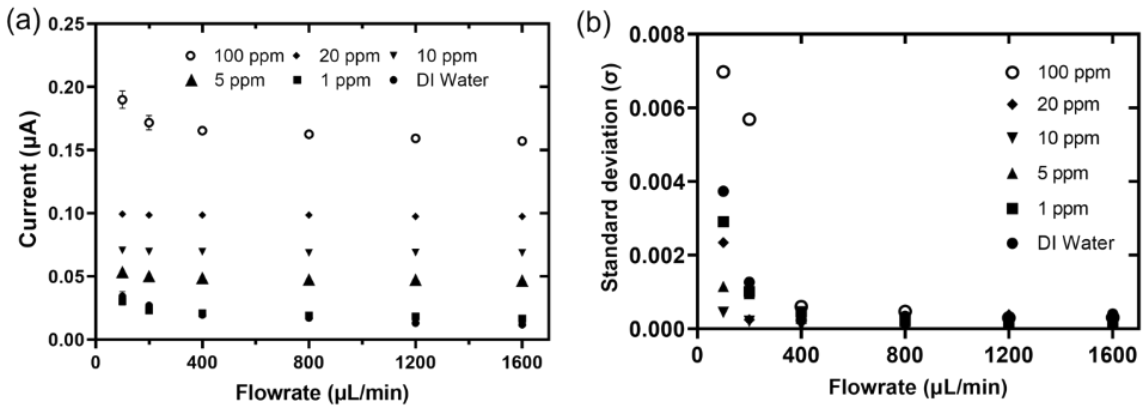

Fig. 3-2 Effect of flowrate on (a) the chronoamperometry current readout, and (b) readout stability defined as standard deviation (SD) of current across different flow rates, highlighting the optimal flow rate range that minimizes signal deviation for reliable electrochemical detection. Legends show NaCl concentrations.

The results depicted in Fig. 3-2a, expectedly demonstrate a significant decrease in current output with a reduction in salt concentration, with the minimum readout (0.02-0.04 μA) obtained with DI water, and maximum (0.16-0.19 μA) for 100 ppm NaCl concentration. Furthermore, at each concentration, there was a noticeable decline in current as the flow rate increased from 100 μl/min to approximately 800 μL/min. Beyond this point, the current became relatively stable and reached a plateau, defined by standard deviations of the current being less than 0.001 (Fig. 3-2b). This suggests a relative insensitivity to further increases in the flow rate, even up to the maximum of 1600 μL/min. Stability at the highest salt concentration, i.e., 100 ppm, was achieved at a minimum flow rate of 800 μL/min, which was selected as the testing flow rate for subsequent experiments.

At higher flow rates, the improved ion transport reduces the influence of the diffusion layer on sensor response [182]. However, at very high concentrations (e.g., 100 ppm), the current shows a slight but continuous decrease. This suggests that the rate of ion consumption in the electrochemical reaction might exceed the rate of ion replenishment, though the overall mechanism

remains unaffected by significant redox interference. Thus, optimizing flow rates is crucial for balancing diffusion and convection effects to ensure consistent and reliable current responses. Shao et al. [183], investigated the electrical characteristics of an Electrical Field Flow Fractionation (EFFF) system using chronoamperometry and electrochemical impedance spectroscopy. Their chronoamperometric measurements demonstrated that increasing the flow rate led to a decrease in current, attributed to enhanced ion transport and reduced boundary layer thickness. In our study, we observed a similar decrease in capacitive current with increasing flow rate. However, this behavior can be attributed to the reduced residence time of ions within the ISP membrane at higher flow rates, leading to diminished ion accumulation at the electrode interface. These differing observations underscore the distinct mechanisms at play in membrane-integrated chronoamperometric systems compared to EFFF-based systems.

The electrochemical sensor operates in a non-faradaic chronoamperometric mode, in which step voltage generates capacitive current through ion accumulation at the electrode–electrolyte interface. The current is attributed to electric double-layer formation and not redox processes, as indicated by cyclic voltammetry experiments that detected no faradaic peaks [184].

3.2.3. Evaluating ISP membrane impact on sensor performance for salt detection

Our goal was to confirm the potential of the ISP membrane in augmenting the sensor's proficiency for salt detection. We tested two sensor configurations, namely the membrane-less and ISP membrane-integrated devices, to assess their effectiveness in detecting salt concentrations in water samples ranging from 0.25 to 800 ppm NaCl. We measured the chronoamperometry response

(Fig. 6a i-ii) of each concentration at a total flow rate of 800 µL/min (based on the flowrate study described earlier) with 3 replicate devices, each tested three times to ensure repeatability. For the ISP membrane-integrated sensor, we selected a membrane thickness of 300 µm due to its fabrication accuracy (Fig. 3-1c) and superior performance compared to thinner and thicker membrane thicknesses [184]. The study suggests that a 300 µm thick membrane provides an optimal balance between minimizing membrane resistance and maximizing trans-membrane ion conductivity, thus enhancing the sensor's overall effectiveness in salt detection.

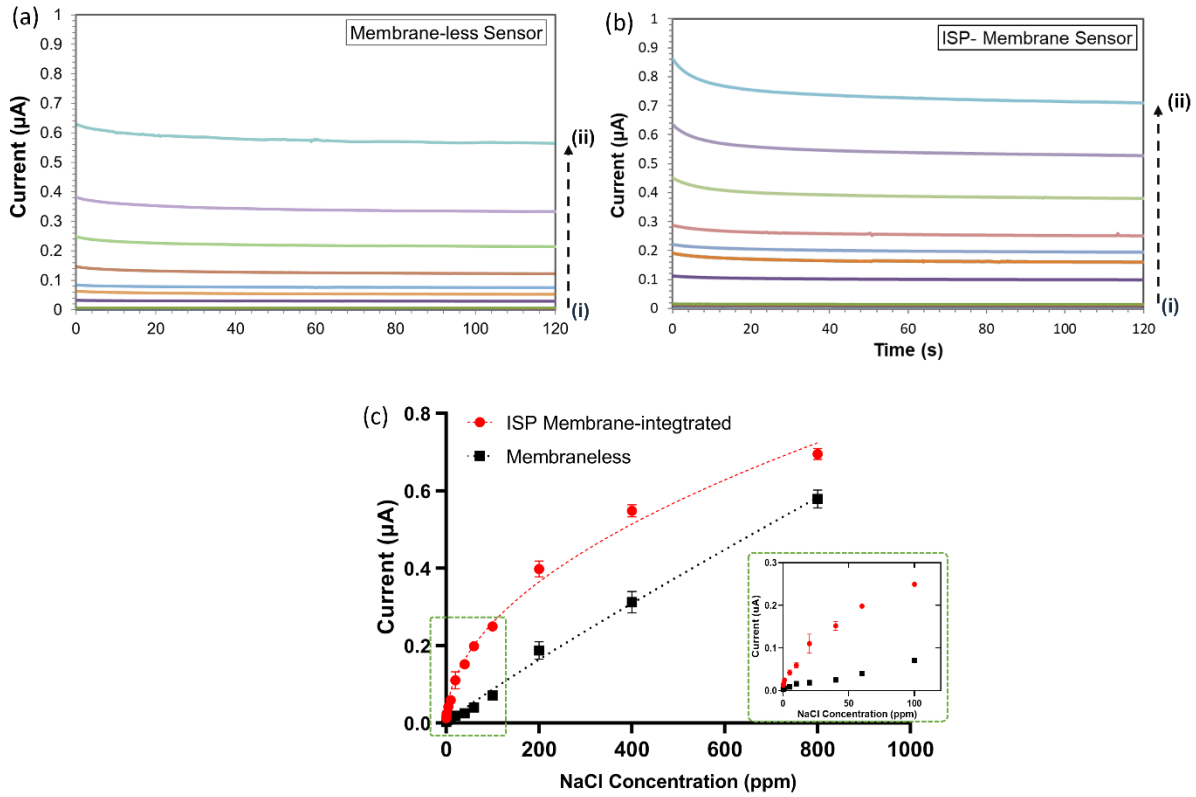

Fig. 3-3 Dose-Response of Microfluidic Salinity Sensor. Chronoamperometric response of the microfluidic salinity sensor to NaCl concentrations ranging from (i) 0 to (ii) 800 ppm NaCl, shown for (a) the membrane-less sensor and (b) the ISP membrane-integrated sensor. (c) Dose-response curves comparing the response of both the membrane-less and ISP membrane-integrated sensors. Each sample tested three times in three replicate devices, with error bars representing SD

The stabilized chronoamperometric currents at t=120s (Figs. 3-3 a-b) show that the ISP membrane-integrated sensor consistently exhibited higher current responses across all concentrations compared to the membrane-less variant. The incorporation of an ISP membrane further enhances the sensor response by selectively enriching Na^+ ions at the electrode surface. This is made possible through electrostatic interaction between Na^+ and carboxylate (COO^-) functional groups, which are incorporated via MAA in the membrane. The functional groups possess a preferential affinity towards Na^+ over competitive cations such as K^+ based on differences in hydration energy, charge density, and ionic radius [185, 186]. Further detailed theoretical explanation of the sensing mechanism is presented in our manuscript[1] .

In Fig. 3-3c, dose-response curves based on the chronoamperometric readings reveal the pronounced impact of the ISP membrane on the sensor's performance characteristics. The ISP membrane-integrated sensor demonstrated a non-linear sensor function of $I(x)=0.02882 \cdot x^2 - 0.00641$ ($R^2 = 0.993$) (I and x being the current and NaCl concentration, respectively). The membrane-less sensor behaves linearly with a function of $I(x)=0.0007x + 0.006$ ($R^2 = 0.995$). Notably, the ISP membrane-integrated sensor achieved a limit of detection (LOD) of 0.45 ppm, representing a 86.7% improvement over the membrane-less sensor's LOD of 3.39 ppm. Similarly, the LOQ for the ISP membrane sensor was 0.49 ppm, showing a 91.6% reduction compared to the membrane-less sensor's LOQ of 5.84 ppm.

The inclusion of the ISP membrane significantly enhanced the sensor's sensitivity as well. The ISP membrane-integrated sensor demonstrated a sensitivity of 20.1 nA/ppm at the LOQ concentration, surpassing the membrane-less sensor's sensitivity of 0.7 nA/ppm, showcasing an improvement of approximately 29-folds over the membrane-less sensor.

The ISP membrane enables a higher recorded current in the sensor due to its porous nature and electrochemical enhancement properties. Its significant porosity facilitates efficient ion transport, while the negatively charged carboxyl groups from methacrylic acid selectively attract cations, intensifying ionic interactions and transport near the electrode surfaces (see next section for more details). This interaction generates a concentrated ion flux at the electrodes, resulting in an amplified current response. Conversely, in the membrane-less configuration, ion transport is less efficient, as convection predominantly moves the ions parallel to the electrodes, into and out of the sensing chamber, leading to lower ionic concentration and current at the electrode surfaces.

Our device demonstrates highly competitive limits of detection and quantification compared to those reported in previous studies on water salinity detection [183, 187–193]. As summarized in Table S2, the most comparable results are from Farshchi Heydari et al. [193] which reported LOD and LOQ values of 0.31 ppm and 0.44 respectively. While the ISP membrane-integrated sensor in the present study achieved comparable values—0.45 ppm (LOD) and 0.49 ppm (LOQ), it offers a substantially broader dynamic range (1–800 ppm vs. 1–120 ppm) and enhanced sensitivity (20.1 nA/ppm), enabling more responsive detection at low concentrations. Notably, the current sensor also introduces selective detection capability through its integrated ISP membrane, allowing for ion differentiation, as will be discussed in the following section.

3.2.4. Impact of key ion-exchanging monomers on ISP membrane-integrated sensor performance

We hypothesized that the improved performance of the ISP membrane-integrated sensor results from the presence of ion-exchanging functional groups within the composition of the ISP

membrane and their interaction with salt ions. To test our hypothesis and confirm the significance of ion-exchanging monomers in the ISP membrane's effectiveness, we conducted a control experiment involving the synthesis of a membrane without the MAA and AAM functional monomers, which contribute the carboxylic acid and amide functional groups, respectively. The results, encompassing measurements within the same 0-800 ppm NaCl concentration range as in the previous section, revealed a stark difference in the response of the sensors (Fig. 3-4).

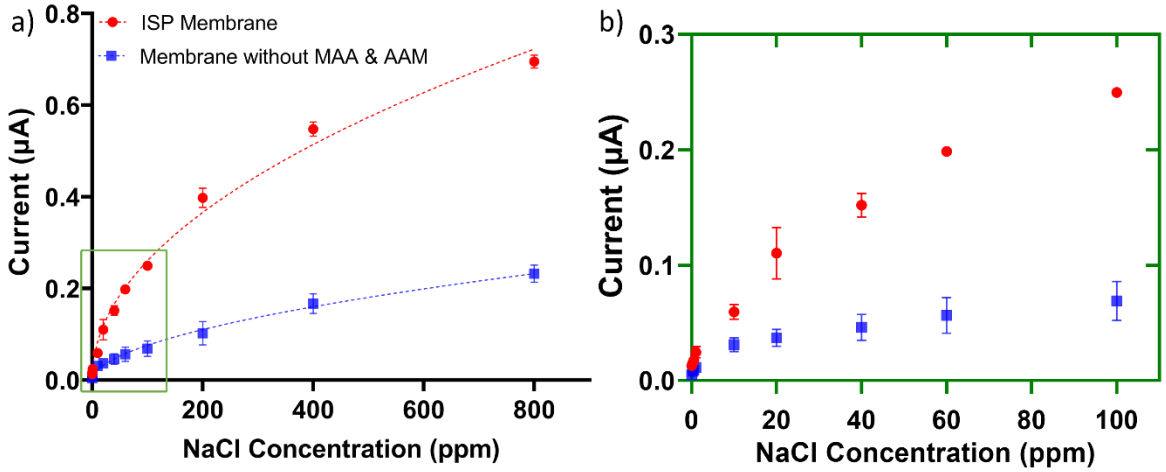

Fig. 3-4 Dose-response curves for the ISP membrane-integrated sensor and the sensor with the membrane lacking the ion-exchanging monomers, for (a) concentrations of 0–800 ppm and (b) an inset showing 0–100 ppm concentrations. Each sample tested three times in three replicate devices, with error bars representing SD.

As depicted in Fig. 3-4, the sensor with the membrane lacking the ion-exchanging monomers exhibited a low current response profile, indicating inferior sensitivity compared to its functional monomer-integrated counterpart. This substantial difference in sensitivity is evident from the steeper slope and greater current response of the ISP membrane-integrated sensor across the entire concentration range. Specifically, the ISP membrane-integrated sensor's sensitivity measured at 20.1 nA/ppm at an LOD of 0.45, significantly outperforming the 2.75 nA/ppm sensitivity of the sensor without the functional groups-representing a 7.3-fold improvement in sensitivity.

Previously, ISEs have been widely used for water quality monitoring, using crystalline and polymeric membranes to detect various metal ions through electrochemical techniques [194, 195]. Our device builds upon these advances by separating the ISP membrane from the electrodes, allowing for independent membrane fabrication without the need for surface treatment, while retaining high sensitivity. ISE-based sensors can experience challenges such as electrode fouling and passivation, which may require periodic calibration and rejuvenation. Crystalline ISEs require surface repolishing, while polymeric ISEs may need new membranes. Integrating ISEs with flow injection or continuous flow analysis can reduce fouling by desorbing adsorbed substances, though additional calibration and cleaning are often still necessary. Traditional liquid-contact ISEs, using internal filling solutions, can encounter issues such as solution evaporation and handling complexity. Solid-state ISEs, developed for better stability, reproducibility, and handling, include substrates like coated-wire electrodes (CWE) [196], and modified glassy carbon [197, 198]. They are prone to issues such as interior water film formation and irreproducibility of electrode potential. To further enhance performance, to further advanced ion-to-electron transducers have been introduced, incorporating materials like ionophores [199], and IIPs [123, 200]. These approaches expand functionality, though they can involve additional fabrication steps and specialized materials.

3.2.5. Evaluation of sensor sensitivity and selectivity

To further assess the performance of our sensor, we first examined its sensitivity to two closely related salt ions, K^+ and Na^+, taking into account their inherent mobility differences. Potassium salts were used as sodium-free controls due to their comparable ionic strength, charge, and hydration radius relative to sodium., allowing for a more precise assessment of sodium selectivity.

This approach ensured that any observed differences in sensor response could be attributed to the intrinsic selectivity of the ISP membrane rather than disparities in ionic properties.

First set of experiments were conducted using the two sensor configurations i.e., the membrane-less sensor, where detection primarily relies on ion transport to the electrode surface; and the ISP membrane-integrated sensor, where the membrane, owing to its functional group charge, interacts with the sample and concentrates counter ions, thereby enhancing the transmembrane signal. Previous studies have shown that membranes containing carboxylate functional groups can exhibit preferential sensitivity towards Na^+ and K^+ ions [185]. Therefore, we tested KCl and NaCl samples across concentrations ranging from 0.25 to 800 ppm, maintaining a consistent optimal flow rate of 800 µl/min, as in previous tests. Our findings are summarized in Fig. 3-5.

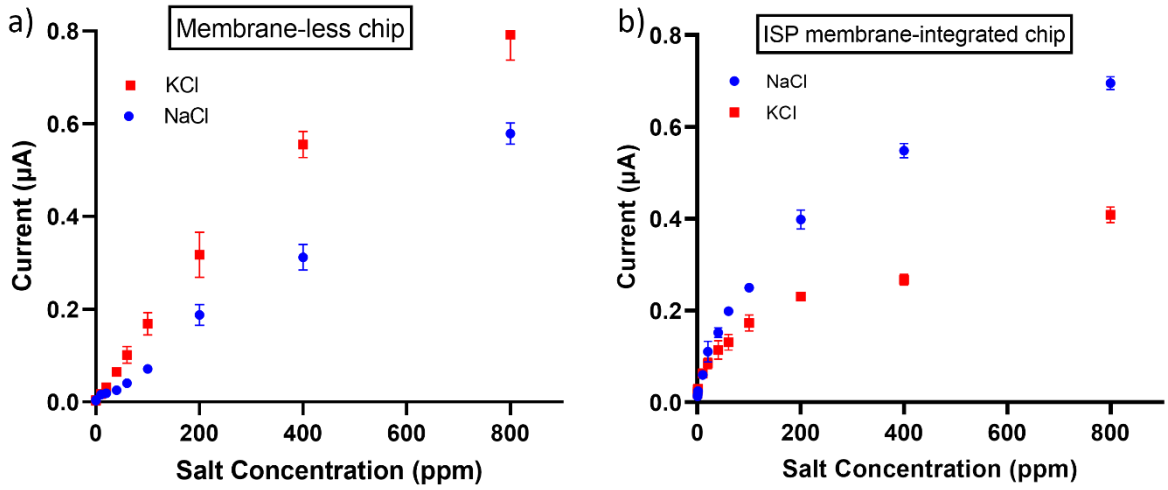

Fig. 3-5 Sensitivity of the sensors. Dose-response curves for NaCl and KCl are compared for (a) the membrane-less sensor and (b) the ISP membrane-integrated sensor. Each sample was tested three times, with error bars representing SD.

As shown in Fig. 3-5 a-b, for concentrations up to 20 ppm, both sensors showed similar responses to either salt, indicating minimal differences at lower concentrations. However, beyond this threshold, the divergent response patterns of both sensor configurations become increasingly

apparent, predominantly highlighted by the slopes of the curves. Notably, the membrane-less device exhibited a sensitivity of 1.05 nA/ppm for NaCl and 0.7 nA/ppm for KCl, with a NaCl:KCl sensitivity ratio of approximately 0.666. This indicates a higher sensitivity to KCl, which can be attributed to the greater ionic mobility of K^+ ions compared to Na^+. The higher mobility of K^+ ions facilitates more efficient ion transport and electrochemical interaction within the sensor, resulting in a stronger response in the membrane-less configuration. Conversely, the membrane-integrated sensor demonstrated a sensitivity of 20.1 nA/ppm for NaCl and 7.05 nA/ppm for KCl, yielding a switch in sensitivity and NaCl:KCl sensitivity ratio of approximately 2.85. This suggests a higher sensitivity to NaCl in the presence of the ISP membrane, potentially correlated with the membrane's higher affinity for Na^+ ions as supported by the literature [202, 203]. They highlight the higher selectivity of carboxylate group-based membranes towards Na^+ compared to K^+, which could be attributed to the lower activation energy for ion transfer associated with Na^+ (10.21 kcal/mol) compared to K^+ (12.33 kcal/mol). This lower energy barrier suggests a higher rate of ion exchange at the membrane interface, enabling more rapid and efficient transport of Na^+ within the membrane matrix, promoting enhanced transport toward the electrode surface. This behavior contributes to the stronger electrochemical response to NaCl observed in the ISP membrane-integrated sensor.

Furthermore, we conducted studies to evaluate the sensor's selectivity by measuring its differential response to sodium chloride in multi-ion mixtures (Fig. 3-6). In all experiments, total salt concentration was maintained at 100 ppm, with equal contributions from each salt in multi-salt mixtures. These experiments aimed to explore how the sensor's response to sodium ions changed in the presence of competing ions, using potassium-based salts due to their relevance in similar applications and their distinct ionic properties.

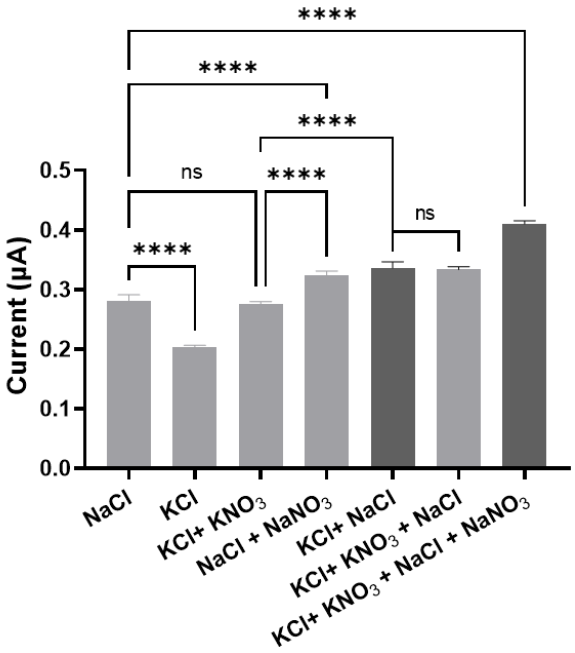

*Fig. 3-6 Sensor sensitivity characteristics in duplex and multi-plex sample mixtures. Each sample was prepared with a total salt concentration of 100 ppm, using equal concentrations of each component. Duplex mixtures included KCl+KNO₃, NaCl+NaNO₃, and KCl+NaCl. Multiplex mixtures included KCl+KNO₃+NaCl and KCl+KNO₃+NaCl+NaNO₃. Error bars are SDs and ns: nonsignificant; *: p-value < 0.05; **: p-value < 0.01; and ***: p-value < 0.001.*

In singleplex studies, KCl and NaCl were used as negative and positive controls, respectively, to establish a reference for multiplex samples. As shown in Fig. 3-6, the NaCl solution exhibited a significantly higher response compared to KCl, with a 37.8% increase in current ($P<0.0001$), underscoring the sensor's lack of pure selectivity but heightened sensitivity towards sodium ions as described before. The observed baseline signal for potassium is attributed to non-specific ionic interactions and capacitive effects at the electrode surface. Three duplex solutions were then tested, i.e., one fully potassium-based ($KCl+KNO_3$), one fully sodium-based ($NaCl+NaNO_3$), and another containing both sodium and potassium (KCl+NaCl). The $KCl+KNO_3$ mixture exhibited a response nearly identical to the NaCl alone (p=ns). The significantly higher response in duplex sodium-

containing mixtures emphasizes the selective interaction and enhanced sensitivity of the ISP membrane towards sodium ions. This is why in the $NaCl+NaNO_3$ and KCl+NaCl samples, the signal was enhanced by 15.2% and 19.8% compared to the NaCl baseline ($P<0.0001$ for both), respectively.

Building on the duplex results, multiplex studies evaluated the sensor's performance in more complex mixtures. The sodium-free baseline ($KCl+KNO_3$) was compared to two sodium-containing mixtures. The $KCl+KNO_3+NaCl$ mixture demonstrated a 20.9% increase in current relative to the $KCl+KNO_3$ baseline ($P < 0.001$). Notably, the $KCl+KNO_3+NaCl+NaNO_3$ mixture exhibited a 22.9% higher response compared to the $KCl+KNO_3+NaCl$ mixture and a 48.7% increase relative to the potassium-only ($KCl+KNO_3$) baseline ($P<0.0001$ for both). These results demonstrate the ISP membrane sensors' capacity to maintain elevated sensitivity towards sodium ions even amidst competing ions in multiplex configurations.

While this study evaluated the sensor's behavior in equimolar Na^+ and K^+ mixtures, future work will include full calibration of NaCl response in the presence of a fixed KCl background to further quantify ion-specific selectivity under competitive conditions. Notably, although some current differences between salt mixtures may appear visually modest, statistical analysis consistently confirms significantly elevated responses for Na^+-containing solutions relative to K^+-only mixtures. This supports the ISP membrane's ion-exchange-driven preference for Na^+. The effect is more pronounced in binary (duplex) configurations (Fig. 3-5), whereas competitive uptake in multiplex systems naturally compresses the magnitude of response differentials.

3.2.6. Real Water Sample Test

To evaluate the applicability of the ISP membrane-integrated electrochemical sensor under realistic conditions, a recovery study was performed using unfiltered municipal tap water collected from the York University campus. To bring the sample's conductivity within the low region linear dynamic range of the sensor, the water was diluted 1:20 with deionized water, creating the working matrix referred to as RW-20. The diluted water samples were spiked with NaCl at concentrations of 10, 20, and 40 ppm. The calibration curve fit established in Fig. 3-3 was used to convert the measured chronoamperometric currents into corresponding NaCl concentrations. Table 3-1 summarizes the test results including the recovery performance and relative standard deviation (RSD), calculated from three replicate measurements at each concentration.

Table 3-1 Recovery analysis of NaCl-spiked RW-20 municipal tap water samples using the ISP membrane-integrated sensor.

Added **NaCl (ppm)**	**Measured (ppm)**	**Recovered (ppm)**	**Recovery (%)***	**SD (μA)**	**RSD (%)**
0	5.45	–	–	0.00235	3.98
10	13.92	8.47	84.7%	0.00906	9.39
20	28.86.	23.41	117.1%	0.00793	5.67
40	47.45	41.99	104.99%	0.00350	1.95

$* Recovery\ (\%) = \left(\frac{C_{measured} - C_{baseline}}{C_{spiked}}\right) \times 100$*; where* $C_{measured} = \left(\frac{I_{measured} - c}{slope}\right)$ *from the calibration fit established in Fig. 3-3.* $C_{baseline}$*: calculated baseline concentration of NaCl in tap water,* C_{spiked}*: known added NaCl concentration. C, I and c denote concentration, current and y-intercept, respectively.*

As shown in Table 3-1, recovery values ranged from 84.7% to 105%, with relative standard deviations (RSD) below 10%, indicating reliable precision and acceptable accuracy in a real water matrix. For completeness, a comparative calibration plot is provided in the Supplementary File of our manuscript[1], showing sensor responses for NaCl-spiked samples in DI water and undiluted

municipal tap water. While both systems exhibit a linear trend, the undiluted tap water condition shows higher baseline and overall current, attributed to the inherent ionic content of the matrix. This observation highlights the influence of matrix conductivity and emphasizes the importance of baseline correction or matrix-matched calibration when applying the sensor in practical scenarios.

3.3. Conclusion

In this chapter, an electrochemical microfluidic sensor integrated with an in-situ synthesized ISP membrane was successfully designed, fabricated, and evaluated for trace-level salinity monitoring in drinking water. The standalone ISP membrane, incorporating carboxylic and amide functional groups, enabled selective interaction with sodium ions, resulting in measurable changes in electrochemical current under chronoamperometric conditions. Performance evaluation revealed that the ISP membrane significantly enhanced the sensor's detection capability. The membrane-integrated sensor achieved a sensitivity of 20.1 nA/ppm, an LOD of 0.45 ppm, and an LOQ of 0.49 ppm. In contrast, the membrane-less device demonstrated a lower sensitivity of 0.7 nA/ppm, with an LOD and LOQ of 3.39 ppm and 5.84 ppm, respectively—highlighting improvements of approximately 28-fold in sensitivity and over 85% in detection limits due to membrane integration. Further tests showed that excluding the ion-exchanging monomers from the membrane composition led to a marked decrease in performance, confirming the critical role of functional groups in enabling selectivity. When tested with diluted municipal tap water, the sensor produced recoveries between 84.7% and 105%, with relative standard deviations (RSDs) below 10%, demonstrating its reliability under realistic conditions. Overall, this work demonstrates that the ISP membrane-integrated sensor provides a sensitive, low-cost, and scalable

approach for point-of-need detection of sodium ions in water. These findings lay the groundwork for further adaptation of the platform to detect additional ions and water quality parameters in subsequent chapters.

Chapter 4

Electrochemical Microfluidic Sensor with Sodium Ion-Imprinted Polymer Membrane for Sensitive and Specific Detection of Sodium in Water [2]

4.1 Introduction

This chapter addresses the third objective of this thesis by advancing the integration of a sodium ion-imprinted polymer (Na-IIP) membrane into a microfluidic electrochemical sensor for selective sodium detection in water. The Na-IIP membrane, synthesized in situ using 15-crown-5 as the ionophore and carboxylic monomers as functional groups, was embedded within a PMMA-based chip to enable direct and selective interaction with sodium ions. The sensor's performance was assessed across a wide concentration range and demonstrated strong specificity towards Na^+ compared to K^+ ions. Validation using multi-ion mixtures and spiked tap water further confirmed the sensor's applicability in realistic conditions. This chapter details the Na-IIP membrane formulation, fabrication process, and electrochemical evaluation, emphasizing the advantages of ion imprinting in enhancing selectivity, simplifying sensor architecture, and supporting future point-of-need application.

[2] A.E. Oseyemi, A. Zabihihesari, Shapour Jafargholinejad, P. Rezai. Electrochemical Microfluidic Sensor with Sodium Ion-Imprinted Polymer Membrane for Sensitive and Specific Detection of Sodium in Water, Microchim Acta 192 (2025) 520.

4.2 Results and Discussion

4.2.1 Na-IIP membrane characterization

This section details the morphological and elemental characteristics of the Na-IIP and NIP membranes, analyzed with SEM, EDS, and FTIR techniques.

4.2.1.1. Morphology and elemental composition

The SEM images of the NIP, unwashed Na-IIP, and washed Na-IIP are presented in Fig. 4-1. The morphology of the NIP surface (Fig. 4-1ai) appears rough with minimal porosity. The unwashed Na^+-IIP (Fig. 4-1bi), which retains the template ions, displays a relatively plain surface without visible pores or cavities. In contrast, the SEM image of the washed Na-IIP (Fig. 4-1ci) reveals a porous structure with well-defined pores that are expected to facilitate enhanced interaction between target Na^+ ions and the imprinted binding sites within the polymer matrix. This confirms that the imprinting and washing steps play a crucial role in developing accessible binding sites for improved ion interaction within the Na-IIP matrix. The observed morphology aligns with prior studies on similar ion-imprinted polymers [114, 171], supporting the polymer's suitability for the intended application by ensuring sufficient surface area and accessibility for ion detection.

In Fig. 4-1, while some pore formation may result from template ion removal, the observed porosity could also be attributed to phase separation, polymer network rearrangement during solvent exchange, or localized fragmentation induced during the washing steps. These additional mechanisms offer a plausible explanation for the larger pore structures seen in the SEM and complement the understanding of morphological evolution in ion-imprinted membranes.

The elemental composition of the polymers was analyzed using EDS (Fig. 4-1aii, bii, cii). EDS analysis of the NIP (Fig. 4-1aii) shows only the presence of C and O, with no detectable Na^+,

indicating the lack of template ions in the non-imprinted polymer. In contrast, the unwashed Na-IIP (Fig. 4-1bii) displays both Na^+ and Cl^- ions, confirming their incorporation into the polymer matrix during the imprinting process. Following the washing step, the EDS of the washed Na-IIP (Fig. 4-1cii) reveals the absence of Na^+ and Cl^- ions, verifying successful leaching.

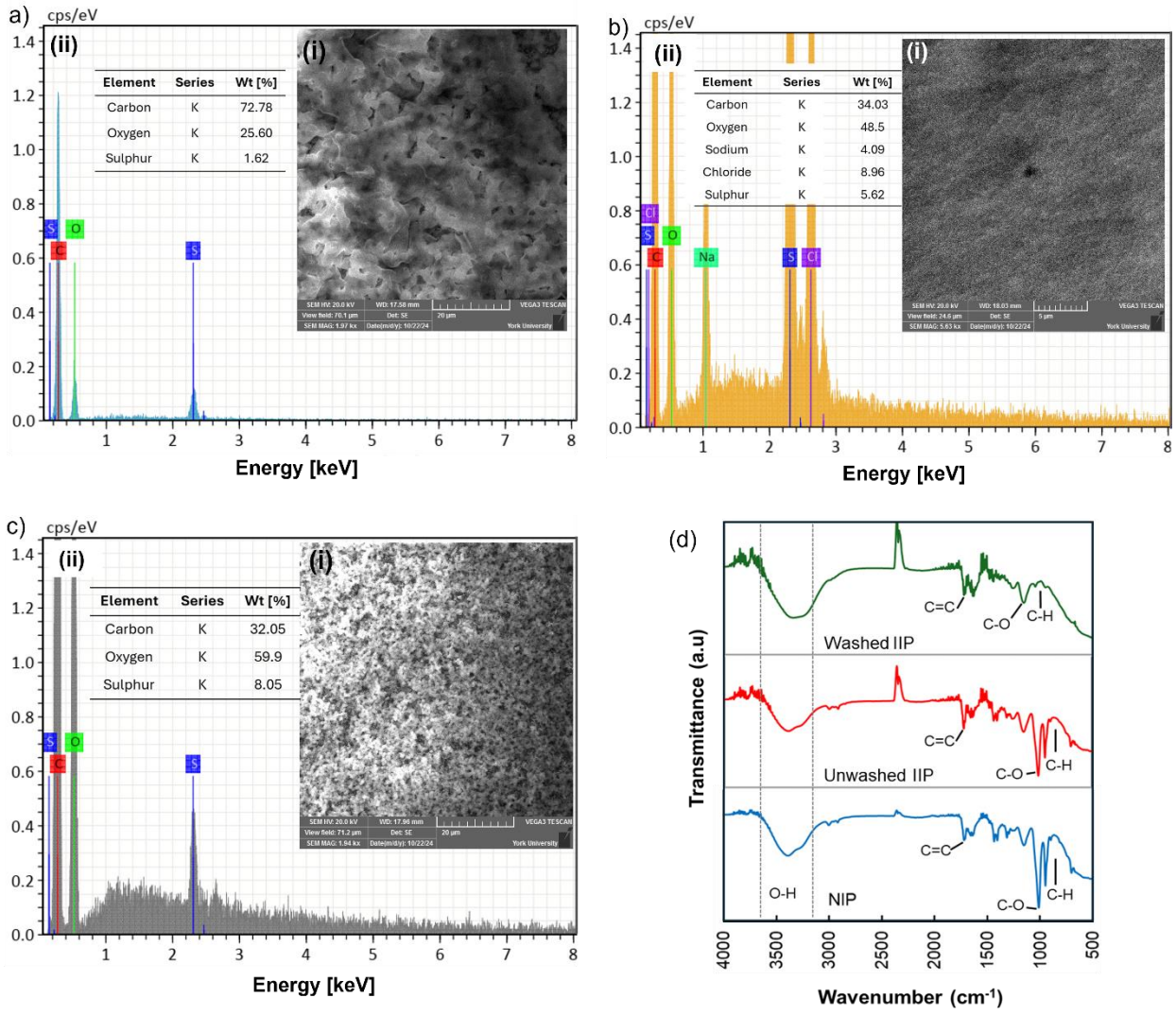

Fig. 4-1 Characteristics of the non-imprinted and Na^+ imprinted polymers. SEM image (i) and EDS analysis (ii) of the (a) NIP, (b) unwashed Na-IIP, and (c) washed Na-IIP are shown. (b) FTIR spectra of the leached and unleached IIP as well as the NIP membranes.

4.2.1.2. FTIR analysis

The FTIR spectra (Fig. 4-1b) revealed characteristic peaks indicative of various functional groups within the polymer. Specifically, the spectrum displayed peaks associated with C=O, C-O, and C=C bonds, which correspond to the ester functional groups in EDGMA and the carboxylic acid and olefin functional groups in MAA [204]. The strong bond observed at 1084 cm^{-1} indicated C-O stretching, primarily associated with the ester groups in EDGMA, while the peak at 1728 cm^{-1} corresponded to the C=O stretching of the ester groups. Additionally, the C=O stretching vibration of the carboxyl group from MAA appears around 1700–1725 cm^{-1}. The broad band observed in the range of 3600–3400 cm^{-1} is attributable to free hydroxyl (-OH) groups [114]. Notably, the presence of a broad absorption peak between 3600 and 2700 cm^{-1} is also indicative of the intramolecular hydrogen bonding [205]. A comparison with the FTIR spectrum of the NIP reveals similar functional group peaks, affirming that both NIP and Na^{+}-IIP polymers contain the same foundational chemical structure. However, the Na-IIP spectrum shows slightly reduced peak intensities for functional groups associated with the template binding, suggesting that imprinting introduces some level of structural variation within the polymer matrix. Overall, the similarity between the IR spectra of un-leached and leached IIPs suggests that the leaching process does not significantly affect the different functional groups in the polymeric network [114, 153].

4.2.2 Effect of flowrate on sensor's electrochemical response

To determine the flowrate for effective sample-membrane interaction, we evaluated NaCl samples at varying concentrations (0 - 200 ppm) across a range of flowrates (50-1200 µL/min) in the sensor. The results are shown in Fig. 4-2. The desired flowrate is identified as the point where the output current stabilizes and shows minimal change (less than 2%) with further increases in

flowrate, consistent across all tested concentrations. The current values used in Fig. 4-2 represent plateau currents extracted from the final 10 seconds of each 60-second chronoamperometry measurement.

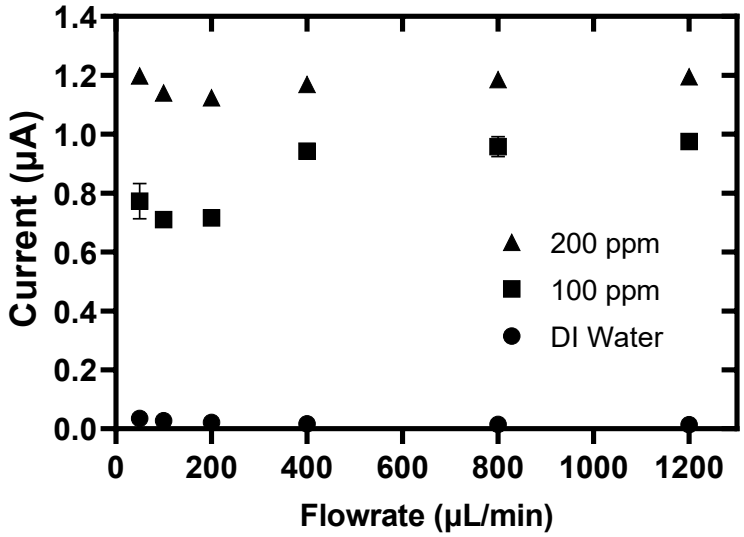

Fig. 4-2. Effect of sample flowrate on the chronoamperometry current readout of the device for different NaCl concentrations. Error bars indicate the standard deviation (SD).

The observed trends in current response at different flowrates highlight critical dynamics in ion transport and sensor functionality. Specifically, at flow rates between 0 and 200 μL/min, the current for both 100 ppm and 200 ppm NaCl concentrations initially decreases. This decline can be attributed to suboptimal mass transport, which hampers the sensor's ability to generate a robust current response. As the flow rate increases from 200 to 400 μL/min, the current begins to rise again. This increase suggests that at this range, the flow rate enhances the mass transfer of ions toward the binding sites, thereby facilitating improved interaction with the membrane. The dynamics shift as the system achieves a balance between the influx of ions and the membrane's capacity to interact with them, allowing for an effective sensing response. Beyond 400 μL/min, the current stabilizes and exhibits minimal fluctuation. This stabilization indicates that the sensor reaches a steady state where the rate of ion flow is suitable for consistent current output.

4.2.3 Quantitative detection of NaCl using the microfluidic sensor

The effectiveness of the Na-IIP membrane in the microfluidic sensor for detecting sodium salts was investigated, specifically comparing its performance to that of the NIP membrane across a wide range of NaCl concentrations from 0 to 1000 ppm. The chronoamperometry response for each concentration was measured (Fig. 4-3) at an optimized flow rate of 400 µL/min, as determined in the previous section. Each test was conducted using three replicate devices, each tested three times to ensure consistency and repeatability. The sensor exhibited high reproducibility across independent devices (RSD < 8%) and stable short-term performance over five consecutive runs with less than 5% signal variation under continuous flow.

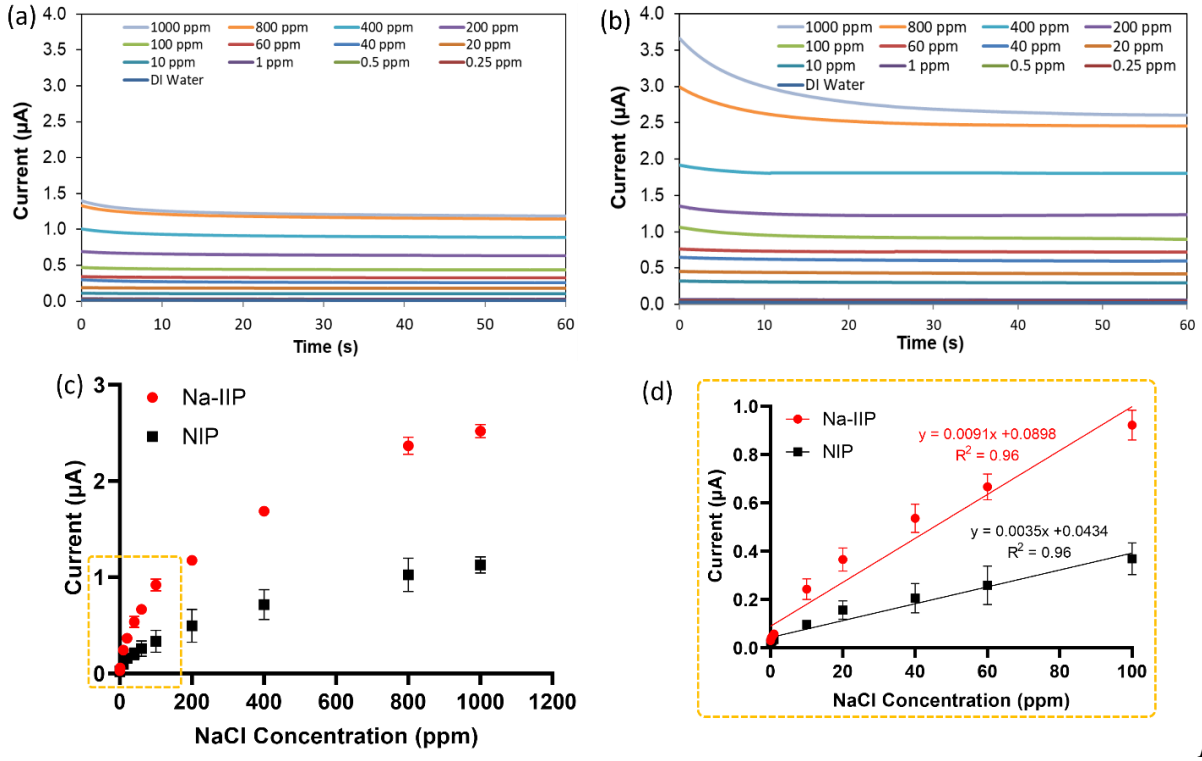

Fig. 4-3 Chronoamperometry response of (a) NIP-based membrane sensor and (b) Na-IIP-based membrane sensor across NaCl concentrations ranging from 0 to 1000 ppm. (c) Dose-response curves comparing both sensor configurations. (d) Extracted dose-response curve focusing on the 0–100 ppm range from panel (c) Each experiment was conducted three times across three replicate devices. Error bars indicate the SD.

In Fig. 4-3a, the chronoamperometry response of the NIP membrane-integrated sensor is shown, revealing plateau currents that range from 23 nA to 1.32 µA for NaCl concentrations between 0 and 1000 ppm. Similarly, Fig. 4-3b depicts the response of the Na-IIP membrane sensor, which exhibits plateau currents ranging from 35 nA to 2.87 µA over the same concentration range. In the NIP sensor, the plateau current was achieved within 5 seconds of chronoamperometry at the highest NaCl concentration of 1000 ppm, while the Na-IIP sensor needed a maximum of about 30 seconds to reach steady state at this salt concentration. This difference can be attributed to the distinct mechanisms of ion interaction in the two sensors. The NIP sensor relies primarily on non-specific interactions, which allow ions to bind and unbind more freely, resulting in faster current stabilization. In contrast, the Na-IIP sensor depends on specific binding to the binding sites, which requires more time to saturate due to the stronger and more selective interactions. Fig. 4-3c-6d compare the plateau currents at various NaCl concentrations, i.e., the dose-response curves, of the two sensors, clearly demonstrating a stronger response from the Na-IIP sensor compared to the NIP sensor.

From the dose-response curves, the NIP sensor demonstrated a LOD of 170 ppb and LOQ of 920 ppb, with a sensitivity of 3.5 nA/ppm. In contrast, the integration of the Na-IIP led to a significantly lower LOD of 58 ppb (a 66% improvement) and a LOQ of 190 ppb (a 79% improvement). Additionally, the sensitivity of the Na^+-IIP sensor is 9.1 nA/ppm, which is over 160 % higher than that of the NIP sensor. Although the NIP sensor's performance is comparatively lower, its response remains noteworthy due to the presence of the carboxylic group in the functional monomer MAA, which facilitates ion exchange and enhances its detection capabilities. Overall, the Na-IIP sensor configuration proves to be significantly more sensitive and precise in detecting Na^+ salts across the tested concentration range. The enhanced performance of the Na-IIP

sensor highlights its superior ability to detect and quantify sodium ions at low concentrations, offering significant improvements in sensitivity. These findings are further supported by the sensor's good repeatability, reproducibility, and operational stability. This underscores the effectiveness of molecular imprinting in creating highly selective and responsive sensor membranes, making the Na-IIP sensor a promising tool for sodium ion detection in various applications.

In comparison to the literature, our Na-IIP sensor shows a significantly lower LOD and LOQ as well as a higher sensitivity in the 0-100 ppm range. For instance, Lim et al. [206] presented an Ion-Selective Electrode system based on an ISP for the selective detection of sodium, measuring in the range of 10^{-4} – 1 M (5.84 to 58,440 ppm), with a sensitivity of 56.1 mV/decade. Giovannitti et al. [207], reported an optical ion sensing method using Na^+ and K^+ ion-selective conjugated CE-based polymer for Na^+ detection. This approach measured concentrations from 0.2×10^{-3} to 10^{-3} M (11.67 to 58.44 ppm), presenting a peak sensitivity at 0.4 mM and a LOD of 10^{-3} M (58.44 ppm). Similarly, Ozer et al. [208] developed a microfluidic-based ion-selective thermoplastic electrode (TPE) array for point-of-care detection of K^+ and Na^+ ions. This TPE array, which featured two working electrodes—one modified with carbon black nanomaterial and the other with an ion-selective membrane—demonstrated a sensitivity of 54 mV/decade to Na^+ in the range of 1 - 10^{-3} M (58,440 to 58.4 ppm) with a LOD of 10^{-4} M (5.84 ppm). This demonstrates the enhanced selectivity and sensitivity of our molecular imprinting approach for precise sodium ion detection.

4.2.4 Specificity and selectivity of the Na-IIP sensor

The Na-IIP sensor was evaluated for specificity by comparing its responses to NaCl, KCl, and KNO_3 solutions. KCl was selected because it contains the cation K^+, which is chemically similar

to Na^+, allowing us to assess how well the sensor discriminates between Na^+ and K^+ ions, which is critical for the sensor's selectivity in mixed-ion environments. KNO_3 was also involved because it also contains the K^+ ion but with a different anion (NO_3^-) compared to NaCl (Cl^-), providing insight into whether the sensor's response is influenced by the anion or primarily by the cation. We hypothesized that the sensor would exhibit a significantly higher response to NaCl compared to the other salts. The dose-response results of the specificity study are presented in Fig. 4-4.

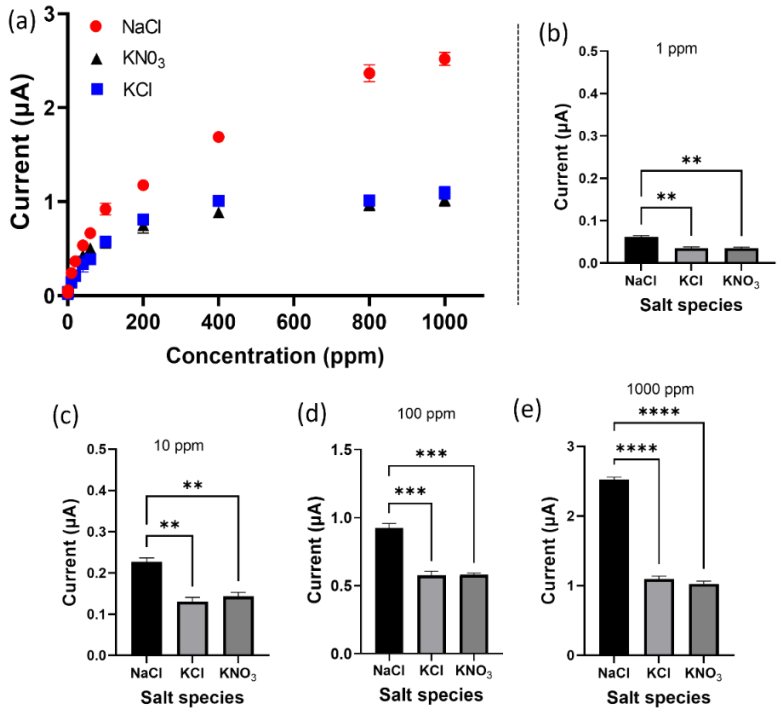

*Fig. 4-4. Specificity study of the proposed microfluidic sensor. (a) Dose response curves of the Na^+-IIP sensor for NaCl, KCl, and KNO_3 across a 0 – 1000 ppm concentration range (template used to fabricate the IIP membrane in all conditions was NaCl). Sample comparison of sensor responses for NaCl, KCl, and KNO_3 are shown at (b) 1 ppm, (c) 10 ppm, (d) 100 ppm, and (e) 1000 ppm, with differences annotated by statistical significance levels: * $p < 0.05$, ** $p < 0.01$, *** $p < 0.001$, and **** $p < 0.0001$. Experiments were conducted in triplicate. Error bars are SDs.*

In Fig. 4-4a, dose-response curves are displayed for each salt across a concentration range from 0 to 1000 ppm. Each dose-response curve exhibits linearity from 0 to 100 ppm, highlighting the

sensor's consistent sensitivity within this range. Notably, the NaCl dose-response curve in the 200–1000 ppm range maintains a positive slope, although less steep than in the linear region, indicating the sensor's sustained sensitivity even at higher concentrations. By contrast, the non-specific responses for KCl and KNO_3 due to interactions with the electrodes reach a plateau in the 200–1000 ppm range, reflecting a limited interaction of these ions with the membrane, which lacks specific binding sites for K^+ ions.

Figs. 4-4 b–e provide a comparative response of the sensors to the three salts at 1, 10, 100, and 1000 ppm concentrations. Quantitative comparisons revealed that at 1 ppm, the response to NaCl was 74.5% higher than KCl and 59.3% higher than KNO_3 ($p < 0.01$). At 10 ppm, similar trends were observed with NaCl responses exceeding KCl and KNO_3 by 74.5% and 59.3%, respectively ($p < 0.01$). At 100 ppm, the sensor's response to NaCl was 60.1% and 58.4% greater than KCl and KNO_3, respectively ($p < 0.001$). Notably, at 1000 ppm, the NaCl response was 129.7% and 146.1% higher than KCl and KNO_3, respectively ($p < 0.0001$). The elevated response to NaCl across all concentrations highlights the Na^+-IIP membrane's tailored binding sites, optimized for Na^+ recognition. This specificity, although not completely exclusive to Na^+, underscores the sensor's design efficiency and its capability to differentiate NaCl from closely related salts like KCl and KNO_3.

While K^+ salts induce low baseline capacitive responses due to non-specific double-layer charging at the electrode, the significantly higher response to NaCl—e.g., a 74.5% increase at 1 ppm ($p < 0.01$)—highlights the contribution of specific binding interactions with the imprinted polymer matrix. These results emphasize that the sensor's sensitivity arise from selective Na^+ recognition, not from general ionic strength effects.

Note on unit consistency: In the above specificity experiments, comparisons between Na^+ and other cations were performed at equal concentrations in ppm. However, due to differences in molar mass (e.g., Na^+ = 23 g/mol, K^+ = 39 g/mol), this means that the number of moles of Na^+ per ppm is greater than that of K^+. Consequently, selectivity analysis in ppm may slightly favor lighter ions like Na^+. While ppm-based comparison is more practical for field-relevant scenarios, future studies may complement this with molarity-based trials to isolate binding preference more precisely.

For selectivity testing, we conducted experiments to evaluate the sensor's differential response to sodium chloride in multi-ion mixtures (Fig. 4-5). In all cases, the total salt concentration was maintained at 100 ppm, with equal contributions from each salt in mixed solutions. These tests aimed to assess how the sensor's response to sodium ions is influenced by competing ions, particularly potassium-based salts, which are relevant in similar applications due to their distinct ionic properties.

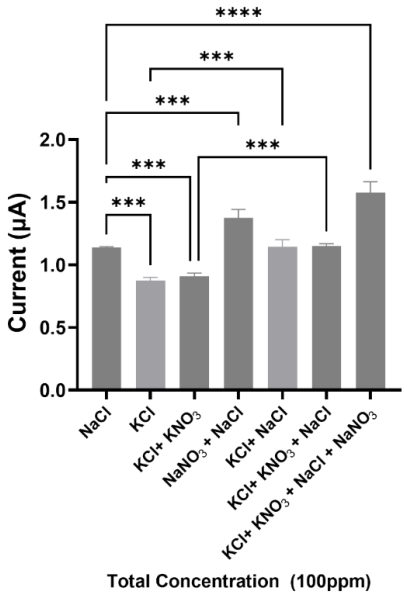

*Fig. 4-5 Selectivity characteristics of the Na^+-IIP sensor with duplex and multiplex mixtures of total 100 ppm concentrations. Experiments were conducted in triplicate. Error bars represent SDs with * indicating p-value <0.05, ** p-value < 0.01, *** p-value < 0.001, and **** P<0.001.*

In singleplex studies, we tested 100 ppm solutions of NaCl and KCl as positive and negative controls, respectively. As shown in Fig. 4-5, the response to NaCl alone was 30% higher than that of KCl ($P<0.001$), confirming the sensor's heightened sensitivity to sodium ions. Three duplex solutions were then analyzed: (1) a fully potassium-based mixture ($KCl+KNO_3$), (2) a fully sodium-based mixture ($NaCl+NaNO_3$), and (3) a mixed sodium-potassium solution ($KCl+NaCl$). The $KCl+KNO_3$ mixture produced a 26% lower response compared to KCl+NaCl and a 52% lower response compared to $NaCl+NaNO_3$ ($P < 0.0001$). These results reinforce the sensor's selective sensitivity to sodium ions across different environments. The residual signal from KCl solutions is attributed to baseline ionic conductivity contributions, included as negative controls to validate sodium selectivity. Notably, the $NaCl+NaNO_3$ and KCl+NaCl mixtures exhibited signal enhancements of 20% and 30.6%, respectively, relative to their NaCl and KCl baselines ($P < 0.001$ for both), further emphasizing the Na-IIP membrane's selective interaction with sodium ions.

In multiplex studies, sodium-free baseline result ($KCl+KNO_3$) was compared to two sodium-containing mixtures: (1) $KCl+KNO_3+NaCl$ and (2) $KCl+KNO_3+NaCl+NaNO_3$. The addition of NaCl to the baseline resulted in a 31% increase in response ($P < 0.01$), while the fourplex solution ($KCl+KNO_3+NaCl+NaNO_3$) exhibited a 51% higher response ($P<0.0001$). These results demonstrate the Na-IIP membrane sensors' capacity to maintain elevated sensitivity towards sodium ions, even in the presence of competing ions in complex environments.

While the primary focus of this study was on establishing proof-of-concept with monovalent ion selectivity, future work will expand the evaluation to include common water constituents such as Ca^{2+}, Mg^{2+}, SO_4^{2-}, and Br^- to further assess interference tolerance. This consistency in sodium-

specific signal, even in the presence of competing ions, suggests limited interference from other ionic species commonly found in real water sources.

4.2.5 Performance evaluation in tap water samples

To evaluate the real-world applicability of the Na-IIP microfluidic sensor, a recovery study was conducted using municipal water collected from public tap on York University campus. The samples were spiked with NaCl at concentrations of 10, 50, and 100 ppm, and all experiments were performed under identical flow and electrochemical conditions as those used for DI water tests. Each concentration was measured in triplicate using independent replicates. A matrix-matched linear calibration curve was generated using the measured currents in tap water samples. The results confirmed strong linearity across the tested concentration range and a stable electrochemical response. Table 1 summarizes the recovered Na^+ concentrations, calculated recovery percentages, and precision metrics.

Table 4-1 Recovery of sodium ions in tap water samples using the Na-IIP sensor.

Added Na (ppm)	Recovered Na (ppm)	Recovery (%)*	SD (µA)	RSD (%)*
0	0.00	-	0.0063	-
10	11.45	114.53	0.0220	1.20
50	53.00	106.00	0.0302	1.45
100	98.46	98.46	0.0435	1.86

$* \ Recovery\ (\%) = \left(\frac{C_{recovered}}{C_{spiked}}\right) * 100$, *where* $C_{recovered} = \left(\frac{I_{measured} - I_{baseline}}{Slope}\right)$ *from the matrix-matched dose-response linear fit in Fig S5; C and I denote concentration and current, respectively.*

 # RSD: Relative standard deviation.

The sensor demonstrated precise and reproducible detection of Na^+ in tap water, with recovery rates ranging from ~114% at 10 ppm to ~98% at 100 ppm, and RSD values consistently below 2%.

The slightly elevated recovery values at lower concentrations likely reflect the presence of trace native sodium in the unspiked tap water. These results indicate good matrix tolerance and validate the Na-IIP sensor's suitability for real-sample analysis.

For completeness, recovery was also assessed using the direct calibration model established in DI water (Fig. 4-3). As presented in the supplementary file section 4, this approach showed some deviations, particularly at lower concentrations, attributable to matrix effects such as ionic strength and inherent sodium content. This emphasizes the significance of matrix-matched calibration for accurate quantification in real water samples. Overall, the results confirm good repeatability and validate the sensor's ability to perform in untreated water samples. Meanwhile, the stable performance observed in untreated tap water (pH ~7.4–7.6) suggests that the sensor maintains functionality within near-neutral pH conditions.

Several studies have explored different approaches to sodium ion detection, each with distinct advantages and challenges. Samreen et al. [209] developed a Cu-doped ZnO nanoparticle (Cu-ZnONP) electrode for Na^+ detection in water samples. The Cu-ZnONPs were synthesized via a solution-based process and integrated into a glassy carbon electrode (GCE) for electrochemical sensing. This sensor demonstrated high sensitivity, strong selectivity, and a linear response to Na^+, with a detection limit of 0.1 ppm. However, the complex synthesis process of the Cu-ZnONPs may be labor-intensive, time-consuming, and challenging for scalability. Cho et al. [210] introduced a sodium ion sensor featuring a Na-ionophore X-based sodium-selective membrane as the extended gate (EG) sensing element, combined with a dual-gate (DG) silicon nanowire (SiNW) field-effect transistor (FET) as the transducer. The sensor exhibited good electrical performance with a sensitivity of 1464.66 mV/dec toward NaCl solutions, and a reasonable LOD of 10^{-4} M (5.84 ppm). Besides all advantages, its complexity, potential ion interference, and reliance on dry etching for

silicon substrate fabrication may pose challenges for large-scale application. Similarly, Cazale et al. [211], developed a sodium ion-selective field-effect transistor (pNa-ISFET) with fluoropolysiloxane-based sensitive layers. It also demonstrated a LOD of 10^{-4} M (5.84 ppm) and a sensitivity of 57 mV/pNa, with a selectivity coefficient (log K_{na}/K_{+}) of -3, indicating limited potassium interference. However, its inkjet-printed membrane requires precise deposition control, complicating mass production. Additionally, the need for robust pre-calibration may reduce its practicality for real-time, point-of-care applications.

4.3. Conclusion

In this chapter, a Na-IIP membrane was successfully synthesized and integrated into a microfluidic electrochemical sensor for the selective detection of sodium ions in water. The in-situ fabricated Na-IIP membrane incorporated crown ether-based ionophores and carboxylic functional groups to create selective binding sites, enabling enhanced analyte–membrane interactions and direct electrochemical readout. Experimental results confirmed the improved performance of the Na-IIP sensor compared to the non-imprinted (NIP) counterpart. The Na-IIP sensor achieved a sensitivity of 9.1 nA/ppm, an LOD of 58 ppb, and an LOQ of 190 ppb, outperforming the NIP sensor, which recorded an LOD of 170 ppb, LOQ of 920 ppb, and a sensitivity of 3.5 nA/ppm. Specificity tests further demonstrated a consistent and significantly stronger response toward Na^+ ions over K^+ in both binary and multi-ion mixtures, with NaCl responses exceeding those of KCl and KNO_3 by up to 146% at higher concentrations. Validation in spiked tap water samples confirmed the sensor's applicability in real-world settings. Matrix-matched calibration improved accuracy, yielding recoveries between 98.5% and 114.5% and RSDs below 2%. The standalone membrane architecture simplified fabrication and eliminated the need for electrode surface

modification, offering a scalable and cost-effective approach for selective ion sensing. These findings demonstrate the potential of Na-IIP-integrated microfluidic sensors for point-of-need water monitoring and set the stage for further development of multi-ion detection platforms with tailored membrane compositions.

Chapter 5

Microfluidic Electrochemical Sensor with Lead Ion-Imprinted Polymer Membrane for Selective Trace Lead Detection in Water[3]

5.1 Introduction

This chapter addresses the fourth objective of this thesis by presenting the development of a microfluidic electrochemical sensor integrated with a lead ion-imprinted polymer (Pb-IIP) membrane for the selective detection of trace lead in water. The Pb-IIP membrane was synthesized in situ using methacrylic acid and 8-hydroxyquinoline as functional monomers, with Pb^{2+} serving as the template ion, and embedded between unmodified electrodes within a PMMA-based microfluidic platform. The sensor was evaluated across a range of Pb^{2+} concentrations and tested in both single-ion and complex multi-ion environments. Compared to membrane-less and non-imprinted polymer (NIP) configurations, the Pb-IIP sensor demonstrated significantly enhanced sensitivity and selectivity toward lead ions. Validation using unfiltered municipal tap water confirmed the sensor's accuracy and repeatability in realistic conditions. This chapter details the membrane formulation, device fabrication, and sensor performance, demonstrating the potential of IIP-based microfluidic platforms for reliable, low-cost environmental monitoring of heavy metals.

[3] A.E. Oseyemi and P. Rezai. Microfluidic Electrochemical Sensor with Lead Ion-Imprinted Polymer Membrane for Selective Trace Lead Detection in Water, Journal of Water Processing Engineering 77 (2025) 108574.

5.2 Results and Discussion

5.2.1 Effect of Membrane Integration on Sensor Performance for Lead Detection

We hypothesized that integrating the Pb-IIP membrane into the microfluidic sensor would enhance its sensitivity and selectivity for Pb(II) detection by providing both chemical affinity mechanisms and physical binding sites tailored for lead ions. Specifically, the Pb-IIP membrane offers three primary mechanisms of affinity for Pb(II), i.e., monomer affinity, ligand affinity, and imprinted site affinity. Monomer affinity arises from the carboxylic acid groups of the MAA functional monomer which can attract Pb(II) ions through electrostatic interactions binding [212, 213]. Ligand affinity relates to the use of 8-HQ in the polymer composition while imprinted site affinity is achieved through the formation of spatially selective binding sites in the IIP matrix during synthesis, which are capable of rebinding Pb(II) ions selectively even in the presence of other ions.

To systematically assess the roles of these affinity mechanisms and understand the Pb-IIP membrane's contribution to sensor performance, we tested four different sensor configurations containing Pb-IIP membrane, MAA-based NIP membrane, AAM-based NIP membrane, or no membrane at all (Fig. 5-1). The Pb-IIP membrane contained MAA with carboxylic acid groups, 8-HQ ligands, and lead ion-imprinted sites, hypothetically resulting in high-specificity towards Pb(II). In contrast, the MAA-NIP membrane, synthesized with the same chemical composition but without the lead template, included MAA and 8-HQ but lacked the specific lead-binding sites, allowing us to evaluate the effects of the ligands and the functional monomers. Finally, the AAM-NIP membrane contained the neutral AAM monomer without carboxylic acid groups. This substitution

of MAA with AAM allowed us to test the effectiveness of 8-HQ ligands in Pb binding without any carboxylic acid functionality and binding sites. For each of these configurations, we measured the chronoamperometric response across various Pb(II) concentrations. This approach allowed us to capture consistent response patterns across different sensor configurations and provided robust data for each concentration level.

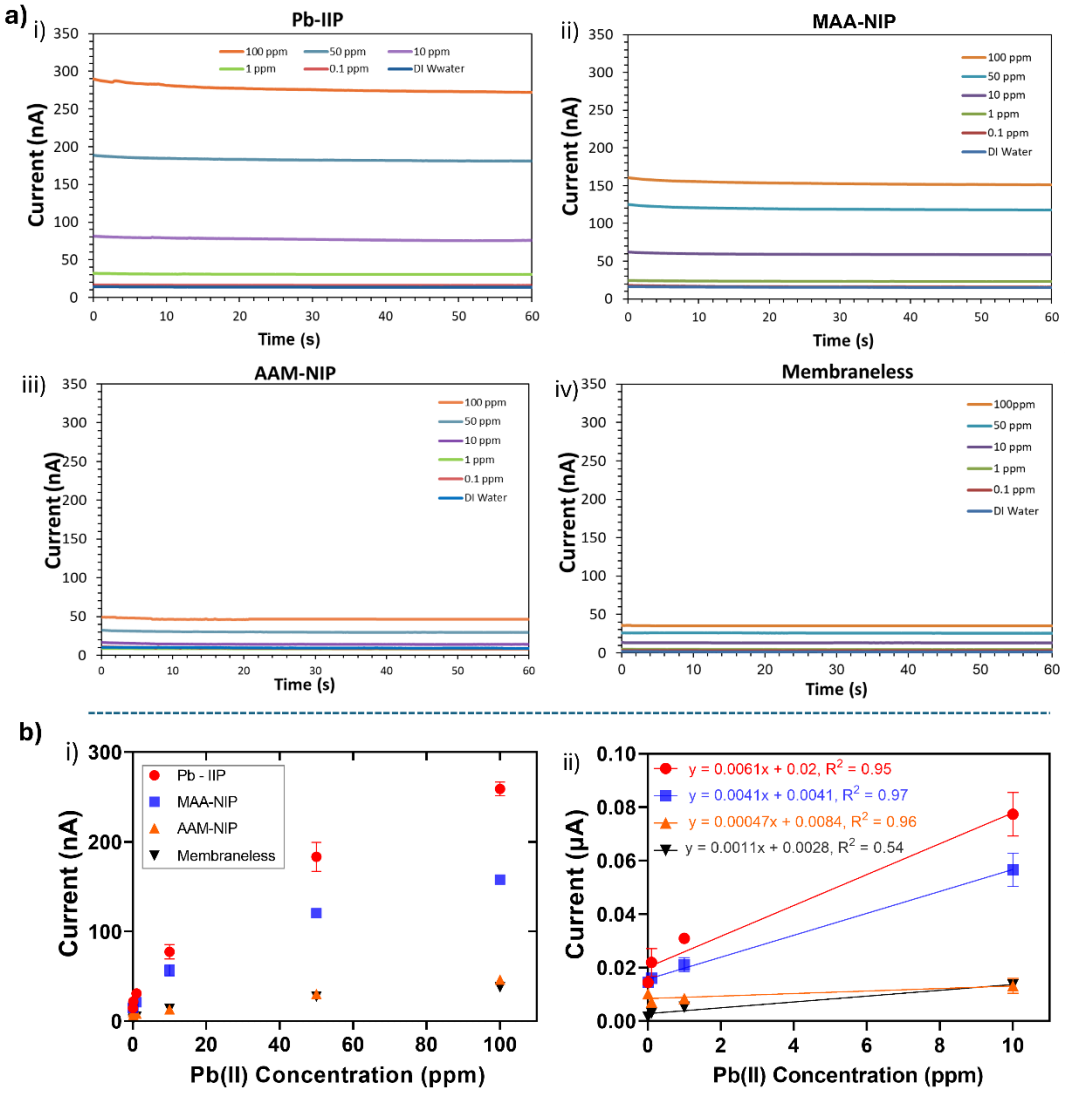

Fig. 5-1 Chronoamperometric responses of various sensors to lead nitrate (0–100 ppm) in DI water. (a) Responses from (i) Pb-IIP, (ii) MAA-NIP, (iii) AAM-NIP, and (iv) membraneless sensors. (b) Dose–response curves from stabilized current at 60 s, shown for (i) full range (0–100 ppm) and (ii) 0–10 ppm region. Flow rate: 400 µL/min; samples tested in triplicate across three devices. Error bars = SD.

The results revealed distinctive performance characteristics for both the membrane-integrated and membrane-less sensor configurations. Each configuration exhibited unique stabilization patterns and current ranges, reflecting the varying affinities and binding characteristics associated with their respective membrane compositions. The Pb-IIP membrane sensor demonstrated the highest sensitivity, with an output current ranging from 14 to 272 nA and stabilization times of approximately 30 s to 1 s for Pb(II) concentrations of 100 to 0.1 ppm, respectively. The longer stabilization time at higher concentrations may be attributed to the increased availability of Pb(II) ions interacting with the imprinted sites, leading to a more gradual equilibrium. In contrast, the MAA-NIP membrane, synthesized without the lead template, exhibited a reduced current range of 16 to 151 nA, stabilizing at 15 s to 1 s for the respective concentrations. Interestingly, the MAA-NIP sensor showed a relatively strong response, supporting the hypothesis that carboxyl groups in MAA might act as ion exchangers, similar to previously reported findings [212, 213]. To further investigate this, MAA was replaced with the neutral monomer AAM, which lacks carboxyl functionality. The resulting AAM-NIP membrane exhibited a much lower current range of 8 to 46 nA, stabilizing at 9 s to 1 s. This significant reduction, despite the availability of 8-HQ, in response suggests that the removal of carboxyl groups diminished Pb(II) interactions, reinforcing the ion-exchange role of MAA. The membrane-less sensor displayed the lowest response, with a current range of 2.9 to 35 nA and rapid stabilization at less than 5 s. The immediate stabilization across all concentrations indicates a simple diffusion-limited response, underscoring the critical role of membrane integration in enhancing Pb(II) detection sensitivity and selectivity.

The current ranges in Fig. 5-1a provided a comparative view of sensor performance under controlled flow conditions, highlighting the importance of both functional monomers and template-driven selectivity in enhancing Pb(II) detection sensitivity. The stabilized current values

at t = 60 s, the point at which all sensors' currents reached a plateau, were then used to construct dose-response curves of each configuration in Fig. 4b, using three replicate devices, with each device tested three times to ensure the repeatability and reliability of our findings.

Fig. 5-1(b) and Table 1 highlight the performance variations among different sensor configurations, reinforcing the effectiveness of IIP membranes for selective Pb(II) detection. The Pb-IIP sensor exhibited the highest sensitivity (6.1 nA/ppm, based on Fig. 5g-1bii) and the lowest LOD (12 ppb), underscoring the advantage of selective binding sites. In contrast, the MAA-NIP sensor, despite lacking imprinted sites, still displayed moderate sensitivity (4.1 nA/ppm), attributable to carboxyl functional groups acting as ion exchangers, as previously mentioned. However, the LOD increased by an order of magnitude in the MAA-IIP sensor showing the importance of the imprinted sites in Pb(II) detection. The AAM-NIP membrane, designed to eliminate the polymeric functional groups, resulted in a dramatic loss of sensitivity (0.47 nA/ppm) and significantly higher LOD (13.16 ppm), confirming the importance of monomer chemistry in Pb(II) interactions. The membrane-less sensor, though slightly better than AAM-NIP, exhibited poor sensitivity (1 nA/ppm), emphasizing the necessity of a selective membrane for optimal Pb(II) detection. These results emphasize the critical role of functional monomers and ion-imprinting in achieving high-performance sensing for lead detection. The sensor reproducibility, evaluated across three replicate devices with triplicate measurements per condition, demonstrated good precision, with a mean coefficient of variation of 5.4%. Furthermore, consistent responses observed across repeated measurements on the same device (up to five uses) showed no significant signal drift, with intra-device variation remaining below 6%, hence supporting the reusability of the sensor under the tested flow and cleaning conditions.

Table 5-1 Performance comparison of microfluidic sensors of Fig. 4b for Pb(II) detection.

Sensor Type	LOD (ppb)	LOQ (ppb)	Sensitivity (nA/ppm)	Fold increase in LOD	Fold increase in LOQ	Sensitivity reduction (%)
				Compared to the Pb-IIP sensor		
Pb-IIP	12	13.9	6.1	—	—	—
MAA-NIP	290	560	4.1	24.1×	40.3×	32%
AAM-NIP	13,160	16,600	0.47	1,096×	1,194×	92%
Membrane-less	67	350	1.0	5.6×	25.2×	84%

5.2.2. Effect of Electrolyte on Lead Detection

To understand the role of supporting electrolytes in enhancing lead detection, we investigated potassium nitrate (KNO_3) and potassium chloride (KCl) based on their distinct ionic properties and widespread use in electrochemical studies [214, 215]. Both electrolytes are commonly employed for their potential to influence ion availability and signal stability. Their effects on electrochemical response characteristics—specifically on charge stabilization and interference reduction—are crucial considerations for optimizing Pb(II) detection. KNO_3, due to its weaker ion-pairing tendency compared to KCl [216], may facilitate improved ion mobility and charge transfer at the electrode surface, leading to enhanced signal stability and detection efficiency. To explore these differences, we assessed the performance of both KNO_3 and KCl in membrane-less and Pb-IIP membrane-integrated sensors across a lead concentration range of 0 to 100 ppm, with a fixed 1 ppm concentration of the chosen electrolyte. Chronoamperometric measurements were conducted using the same parameters as in previous tests, with dose-response curves constructed to compare the sensor performance under each electrolyte condition, as illustrated in Fig. 5-2.

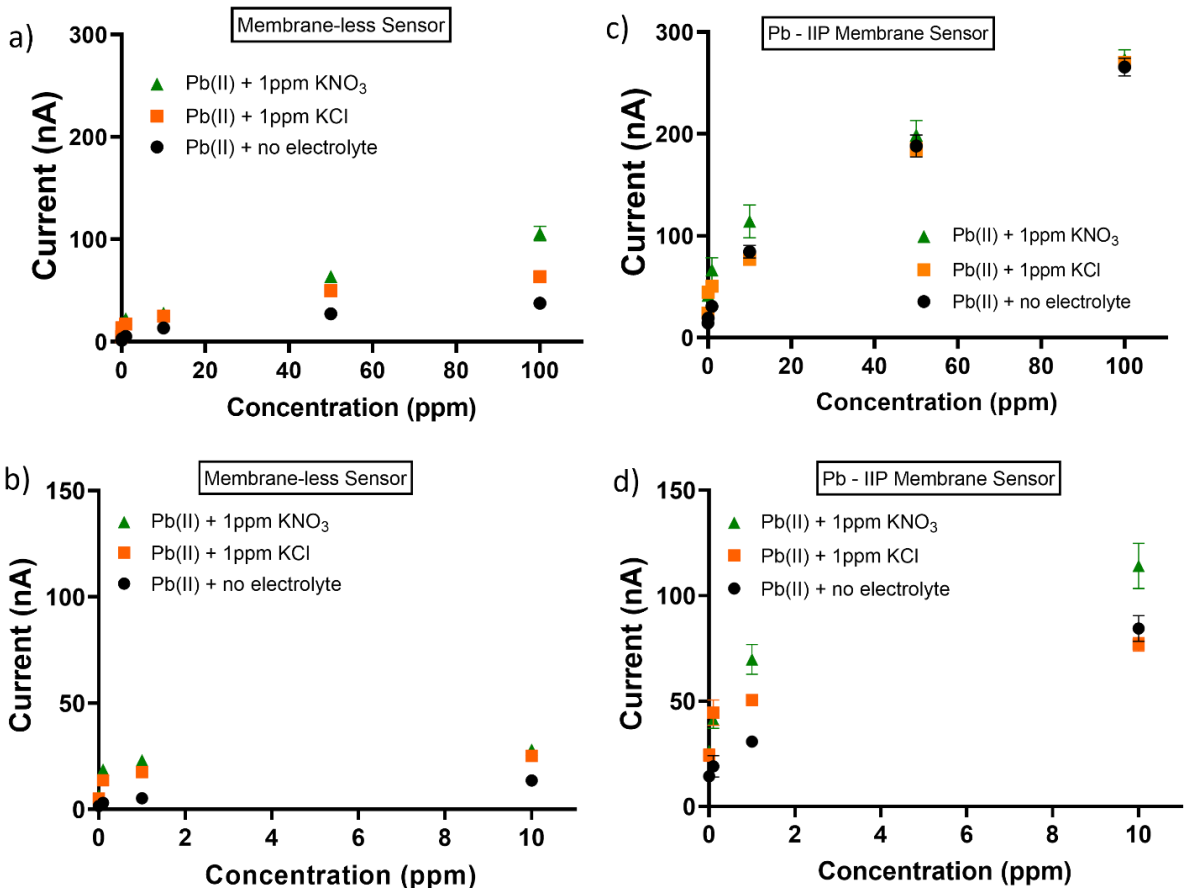

Fig. 5-2 Effects of 1 ppm KNO_3 and KCl electrolytes on lead detection in DI water using (a-b) membrane-less and (c-d) Pb-IIP membrane-integrated microfluidic sensors. Experiments were conducted with each sample tested in triplicate across three replicate devices. Error bars represent SD.

As shown in Fig. 5-2, both electrolytes enhance lead response in both sensor configurations, with KNO_3 demonstrating a greater impact than KCl. This difference may be due to the varying ionic strengths of the electrolytes, which might influence the mobility of lead ions more significantly in the absence of a membrane. In contrast, while the Pb-IIP membrane-integrated sensor still exhibits electrolyte-dependent variations, its selective binding properties help stabilize ion exchange processes, reducing the extent of these variations compared to the membrane-less sensor. This is desirable in moving towards more realistic samples in the future where the presence of electrolytes and other impurities will be prominent.

Table 5-2 summarizes the influence of the electrolyte choice in sensor optimization. The results indicate that KNO_3 provides the best detection capabilities, with the lowest LOD and highest sensitivity across both membrane-less and Pb-IIP membrane-integrated sensors. In contrast, KCl resulted in a moderate decline in performance, likely due to competing chloride interactions affecting Pb(II) binding. Notably, the absence of an electrolyte significantly reduced sensitivity, emphasizing the importance of ionic strength in facilitating efficient electron transfer and Pb(II) interactions at the sensor interface.

Table 5-2 Effect of electrolyte choice on microfluid sensor performance

Sensor Configuration	Electrolyte	LOD (ppb)	LOQ (ppb)	Sensitivity (nA/ppm)
Membrane-less	KNO_3	15	48	0.9
	KCl	22.2	78.2	0.54
	None	67.2	354	0.31
Pb-IIP Membrane	KNO_3	7.3	56	2.2
	KCl	31	170	2.3
	None	12	140	2.4

Overall, these findings emphasize the critical role of supporting electrolytes in optimizing sensor performance. KNO_3, with its higher ionic strength, enhances sensitivity and lowers detection limits, particularly in the membrane-less sensor. However, the Pb-IIP membrane provides an added advantage by stabilizing ion exchange processes, thereby minimizing the variability introduced by different electrolytes. This capability ensures that the Pb-IIP membrane sensor delivers more consistent, and reliable performance, highlighting its advantage over the membrane-less configuration.

5.3.3 Sensor Specificity for Lead Detection

To evaluate the specificity of both the Pb-IIP membrane and membrane-less sensors, we assessed their response to sources of cadmium (Cd(II)), zinc (Zn(II)), and lead (Pb(II)) ions, with DI water as the base fluid. The Pb-IIP membrane sensor was hypothesized to demonstrate a significantly higher response to Pb(II) due to its tailored binding sites, while the membrane-less sensor was anticipated to exhibit less consistent specificity, if any. Fig. 5-3 presents the specificity results across different concentrations (0.1, 1, 10, and 50 ppm) of these ions.

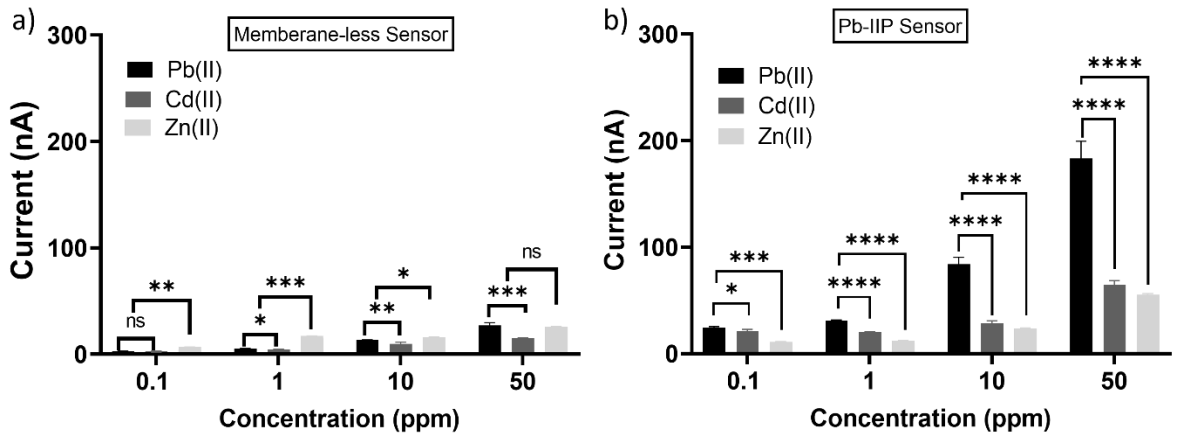

*Fig. 5-3 Sensors' specificity characterization towards lead. Responses of the a) membrane-less and b) Pb-IIP membrane integrated sensor to lead, cadmium, and zinc are demonstrated at concentrations of 0.1, 1, 10, and 50 ppm. Error bars represent SD and statistical significances are noted with *p-value < 0.05, **p-value < 0.01, ***p-value < 0.001, and ****p-value < 0.0001.*

The membrane-less sensor exhibited no consistent specificity towards Pb(II) compared to Cd(II) and Zn(II). At all concentrations, the response to Zn(II) was higher than Pb(II), while Cd(II) produced the weakest signal. These results highlight the membrane-less sensor's challenges in maintaining specificity, as its responses to zinc were often higher than lead, particularly at lower concentrations, likely due to zinc's higher mobility. Responses to cadmium, however, showed less consistent trends, suggesting potential variability in ion-sensor interactions.

In contrast, the Pb-IIP sensor consistently exhibited a higher response to Pb(II) than to Cd(II) and Zn(II), highlighting its specificity. At a 0.1 ppm concentration, the sensor's response to Cd(II) and Zn(II) was 12.5% and 54.2% lower than to Pb(II), respectively, with statistical significance achieved ($p<0.05$ and $p<0.001$, respectively). At 1 ppm, the differences became more pronounced, with responses to Cd(II) and Zn(II) being 35.5% and 61.3% lower than to Pb(II), both with a high level of statistical significance ($p<0.0001$). This trend persisted at 10 ppm, where Pb(II) responses exceeded Cd(II) and Zn(II) by 64.2% and 70.3%, respectively ($P < 0.0001$). At 50 ppm, the Pb(II) response remained higher by 63.9% and 69.4% compared to Cd(II) and Zn(II), respectively, maintaining strong statistical significance ($p < 0.0001$).

The Pb-IIP membrane sensor demonstrated consistent and reliable specificity for lead, with markedly higher responses and greater statistical significance across all tested concentrations. The sensor’s ability to maintain a strong and consistent response to Pb(II), while minimizing responses to non-Pb ions, reflects the critical role of the Pb-IIP membrane in its performance.

5.3.4 Pb-IIP Sensor Selectivity for Lead Detection

To evaluate the selectivity of the Pb-IIP sensor, we conducted experiments measuring its differential response to Pb(II) ions in multi-ion mixtures containing closely related Cd(II) and Zn(II) ions (Fig. 5-4). Three scenarios were simulated with multiplex ion solutions, i.e., (i) equal proportions (Pb:Cd:Zn at 10 ppm in a 1:1:1 ratio), (ii) Pb-dominant (Pb:Cd:Zn at 10 ppm in a 2:1:1 ratio), and (iii) a competitive environment (Pb:Cd:Zn at 10 ppm in a 1:2:2 ratio). The individual responses of Pb(II), Cd(II), and Zn(II) at equivalent concentrations served as controls. This approach allows assessment of the sensor's selectivity in varying, multi-ion water conditions, where competition among ions could impact detection accuracy.

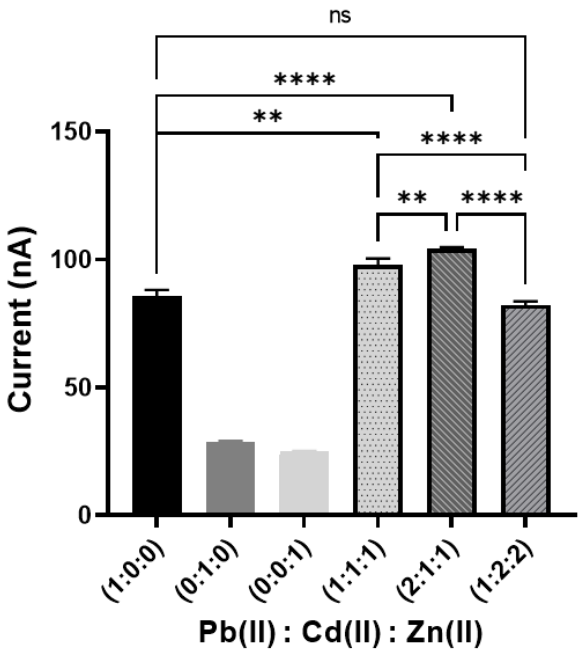

*Fig. 5-4 Selectivity characteristics of the Pb-IIP membrane sensor tested in 10 ppm solutions of Pb(II), Cd(II), and Zn(II) in ratios of 1:1:1, 2:1:1, and 1:2:2. Error bars represent SDs and statistical significances are noted with *p-value < 0.05, **p-value < 0.01, ***p-value < 0.001, and ****p-value < 0.0001.*

For individual ions, the Pb-IIP sensor's response to Pb(II) alone was 195% higher than Cd(II) and 240% higher than Zn(II), demonstrating strong specificity for lead ions ($p < 0.0001$), while the responses to cadmium and zinc were not significantly different (ns). In the 1:1:1 mixture (equal proportions), the sensor exhibited a 16.5% higher response than Pb(II) alone, suggesting a minimal increase due to the presence of non-target ions. Moreover, the response was 19.2% higher compared to the competitive solution (1:2:2), underscoring the sensor's ability to maintain selectivity even when the concentrations of competing ions were twice that of Pb(II). In contrast, the competitive solution (1:2:2) showed a 14.7% lower response than the equal proportion solution ($p<0.05$), highlighting the impact of increased interfering ion concentration on sensor performance. Meanwhile, the Pb-dominant solution (2:1:1) produced a 26.8% higher response than

the competitive solution (1:2:2) ($p < 0.0001$), further confirming the sensor's strong preference for Pb(II).

Overall, the elevated response to Pb(II) across all tested scenarios underscores the Pb-IIP membrane's strong selectivity for Pb(II), even in the presence of potential interfering ions. Although Cd(II) and Zn(II) produced measurable signals in all conditions, these signals likely resulted from weak, nonspecific interactions with the imprinted polymer matrix and simultaneous capacitive charging of the electrode. These effects, however, did not compromise the sensor's selectivity. The Pb-IIP membrane's ability to reliably distinguish Pb(II) in complex ion mixtures highlights its potential for reliable lead detection in real-world water monitoring applications such as the ones shown in the next section.

Our sensor maintains its performance advantages when compared to conventional ion-selective electrodes (ISEs) that have been employed for heavy metal detection, using crystalline or polymeric membranes. Despite their sensitivity, these sensors often face challenges such as electrode fouling, signal instability, and maintenance requirements like membrane replacement or surface repolishing [55, 194, 196, 217]. While integrating ISEs with flow-based systems helps reduce fouling, issues such as water layer formation and potential drift persist, particularly in solid-contact configurations like coated-wire electrodes and modified glassy carbon electrodes [198, 218]. Efforts have been made to improve performance through ion-to-electron transducers or IIP-functionalized membranes [123, 199, 218–220], but these typically involve complex and costly surface treatments. In contrast, the architecture of our Pb-IIP sensor decouples the IIP membrane from the electrode, enabling independent membrane fabrication without the need for electrode surface modification. This simplifies manufacturing, enhances scalability, and preserves high selectivity and sensitivity, as demonstrated in both multiplex and real-water recovery validation

studies. A cost analysis supporting the sensor's economic viability is provided in the Supplementary File Section 5 of our manuscript[3] .

5.3.5. Lead Detection in Real Water Sample using the Pb-IIP Sensor

To evaluate the applicability of the Pb-IIP sensor in realistic conditions, a recovery study was performed using unfiltered municipal tap water collected from the York University campus. The water samples were spiked with $Pb(NO_3)_2$ at concentrations of 1, 2, and 5 ppm. A comparison between the dose-response curves of the sensor and their linear regression analysis using real water and DI water is shown in Supplementary File Section 6 of our manuscript[3]. A matrix-matched linear calibration curve was generated using the tap water matrix, and sensor responses were used to calculate the recovered Pb(II) concentrations. Table 5-3 summarizes the recovery results, including the recovered concentrations and the associated precision in terms of standard deviation and relative standard deviation (RSD) across three replicate measurements per concentration level.

Table 5-3 Pb(II) Recovery from Spiked Municipal Water Samples

Spiked Pb, C_{spiked} (ppm)	**Recovered Pb, $C_{recovered}$ (ppm)**	**Recovery (%)***	**SD (ppm)**	**RSD (%)**
0	-0.08	-	0.20	
1	0.97	96.6%	0.02	2.4%
2	2.18	109.0%	0.04	2.1%
5	4.94	98.7%	0.32	6.5%

* $Recovery\ (\%) = \left(\frac{C_{recovered}}{C_{spiked}}\right) * 100$, where $C_{recovered} = \left(\frac{I_{measured} - I_{baseline}}{Slope}\right)$ was measured from the dose-response curve in Fig S6 of manuscript[3].

As shown in Table 5-3, the sensor demonstrated good accuracy and precision across all tested concentrations, with recoveries ranging from 96.6% to 109% and RSD values below 7%. These

performance metrics fall within accepted analytical criteria for trace metal detection in environmental samples. Overall, the results confirm the Pb-IIP sensor's robustness and suitability for Pb(II) detection in municipal water, particularly when supported by matrix-matched calibration strategies.

5.4 Conclusion

In this chapter, a lead ion-imprinted polymer (Pb-IIP) membrane was successfully integrated into a microfluidic electrochemical sensor for trace Pb^{2+} detection in water. The in-situ synthesized membrane, incorporating methacrylic acid and 8-hydroxyquinoline, enabled selective lead binding and direct electrochemical readout between unmodified electrodes. The Pb-IIP sensor achieved a LOD of 12 ppb, LOQ of 13.9 ppb, and a sensitivity of 6.1 nA/ppm—representing an 84% sensitivity improvement over the membrane-less sensor. Among NIP controls, the MAA-based NIP outperformed the AAM-based variant, highlighting the role of carboxylic groups in enhancing ion interaction. KNO_3 as a supporting electrolyte further reduced the LOD to 7.3 ppb, while KCl showed diminished performance. Specificity tests confirmed significantly higher responses for Pb^{2+} over Cd^{2+} and Zn^{2+} across all concentrations. Multi-ion selectivity studies reinforced this preference, with Pb-dominant mixtures yielding up to 26.8% stronger signals. Validation in municipal tap water showed excellent recoveries (96.6–109.0%) and precision (RSD <7%).These findings demonstrate the sensor's high selectivity, sensitivity, and suitability for low-cost, real-world lead monitoring, supporting future adaptation toward portable, field-deployable platforms.

Chapter 6

Sensitive and Selective Electrochemical Detection of Lithium Using a Low-Cost Ion-Imprinted Polymer Based Microfluidic Sensor[4]

6.1 Introduction

This chapter addresses the third and fourth objectives of this thesis by introducing a lithium ion-imprinted polymer (Li-IIP) membrane integrated into a microfluidic electrochemical sensor for the selective and sensitive detection of lithium in water. The Li-IIP membrane, synthesized in situ using methacrylic acid as the functional monomer and 12-crown-4 as the ionophore, was embedded within a PMMA-based microfluidic chip to enable direct interaction with Li^+ ions. The sensor's performance was evaluated across a range of lithium concentrations (< 50 ppm) and under interference from competing salts. Compared to membrane-less and non-imprinted configurations, the Li-IIP sensor demonstrated significantly improved sensitivity and specificity. Validation in spiked tap water further confirmed its practical applicability. This chapter details the membrane formulation, sensor fabrication, and performance evaluation, highlighting the potential of the Li-IIP platform for low-cost lithium monitoring in environmental and health-related applications.

[4] A.E. Oseyemi and P. Rezai. Sensitive and Selective Electrochemical Detection of Lithium Using a Low-Cost Ion-Imprinted Polymer Based Microfluidic Sensor., IEEE Sensors Journal 25 (2025) 32074–32083

6.2 Results and Discussion

6.2.1 Characterization of NIP and Li-IIP membranes

As mentioned earlier, the imprinted polymer membrane composition was informed by a previous study [176], which reported high adsorption capacity and favorable kinetics for Li^+ capture. The optimal molar ratio of template:monomer:crosslinker (1:5:20) and the use of 12-crown-4 as the complexing ligand were adopted accordingly. To ensure comparability across membrane characterizations and electrochemical tests, all experiments were conducted under controlled pH and ionic strength conditions. Fourier Transform Infrared (FTIR) spectroscopy and Scanning Electron Microscopy (SEM) were employed to analyze the NIP and Li-IIP membranes (washed and unwashed) (Fig. 6-1). FTIR confirmed the imprinting process and the structural integrity of the polymer throughout the washing process, while SEM provided insights into the surface morphology of the non-imprinted and imprinted membranes under different conditions.

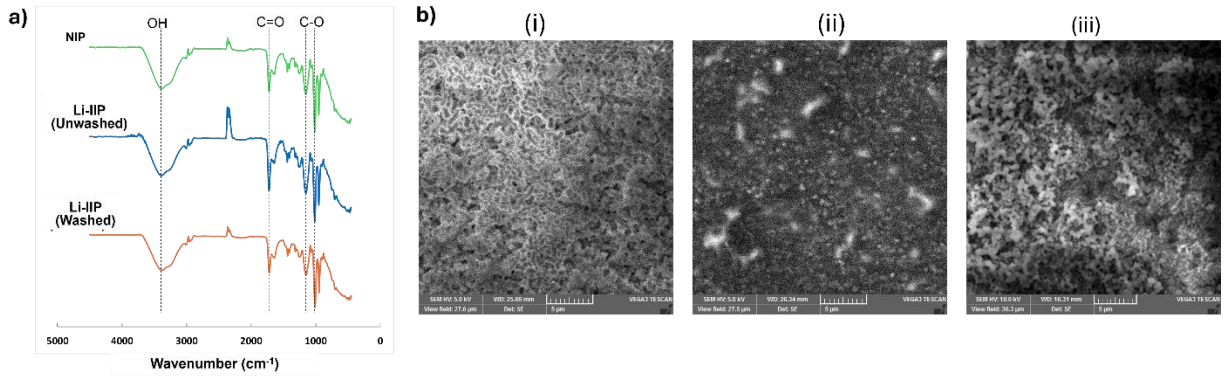

Fig. 6-1 NIP and Li-IIP membrane characterization. (a) FTIR spectra of the NIP, and the unwashed and washed Li-IIPs. (b) SEM images showing the surface morphologies of (i) NIP, (ii) unwashed Li-IIP, and (iii) washed Li-IIP membranes.

The FTIR spectra verified the successful synthesis of both Li-IIP and NIP membranes, with similar profiles across all samples, confirming the retention of the polymer backbone structure, including the complexing ligand 12C4. Key absorption peaks observed include 3307.8 cm^{-1}, corresponding to stretching vibration of the −OH group as well as 1001.2 cm^{-1} and 1227.2 cm^{-1}, corresponding to stretching vibrations of the C−O group. These peaks are indicative of the presence of the functional groups associated with 12C4 in both Li-IIP and NIP membranes. Notably, the 3401.2 cm^{-1} peak observed in the Li-IIP spectra was broader and more intense compared to the NIP. This broadening suggests the formation of hydrogen bonds, which is a typical feature of successful imprinting. Furthermore, the absorption peak at 1729.3 cm^{-1} observed in the Li-IIP spectra corresponds to the C=O stretching vibration, signifying the presence of the carboxyl group from MAA and the ester group from EGDMA. A distinct peak around 2300 cm^{-1} was notably higher in the unwashed Li-IIP membrane but diminished after washing, suggesting its association with residual template molecules or unreacted monomers. These peaks confirm the successful polymerization of the Li-IIP structure, as well as the successful integration of the imprinting components (MAA, EGDMA, and 12C4) into both the imprinted (Li-IIP) and non-imprinted (NIP) polymers. These results are consistent with previous studies [176, 221].

SEM imaging revealed notable differences in the surface morphology of the NIP, unwashed Li-IIP, and washed Li-IIP membranes. The NIP surface appeared smooth and homogeneous, reflecting a uniform polymer structure. In contrast, the unwashed Li-IIP membrane showed a dense and irregular surface structure, likely due to residual template molecules and unreacted monomers. After washing, the Li-IIP membrane displayed a more defined and porous appearance, a hallmark of reacting monomers and effective template removal.

6.3.2 Effect of membrane integration in the microfluidic sensor on Li detection

We hypothesized that incorporating the Li-IIP membrane into the microfluidic sensor would enhance its sensitivity and selectivity for Li-ion detection. This enhancement could hypothetically be attributed to the combined effects of electrostatic interactions with the carboxylic acid groups of MAA, specific binding to 12C4 ligands through crown-ether complexation [222], and or capturing within the imprinted binding sites [178, 179, 222].

To systematically evaluate the contributions of the above Li-capturing mechanisms and assess the role of the Li-IIP membrane in sensor performance, we tested three distinct membrane configurations, i.e., Li-IIP membrane, MAA-NIP membrane, and AAM-NIP membrane. The Li-IIP membrane provided all three mechanisms of Li-capturing. In contrast, the MAA-NIP membrane was synthesized with the same chemical composition as the Li-IIP membrane but without the Li-ion template, allowing for evaluating the effects of monomer and ligand binding in the absence of template-induced binding sites. Finally, the AAM-NIP membrane was synthesized by replacing MAA with AAM, a neutral monomer lacking carboxylic acid groups. This configuration without monomer- and cavity-based binding enabled isolation of the effect of 12C4 ligand binding. Chronoamperometric measurements (Fig. 6-2) were performed for each configuration across various LiCl concentrations using three replicate devices, with triplicate measurements for each device to ensure reliability. This approach allowed us to capture consistent response patterns across different sensor configurations and provided robust data for each concentration level. All tests were conducted at a flowrate of 200 μL/min, based on an optimization study (Supplementary File Section 4 of manuscript[4]) that showed that it provided consistent responses with minimal variation under all tested flow conditions.

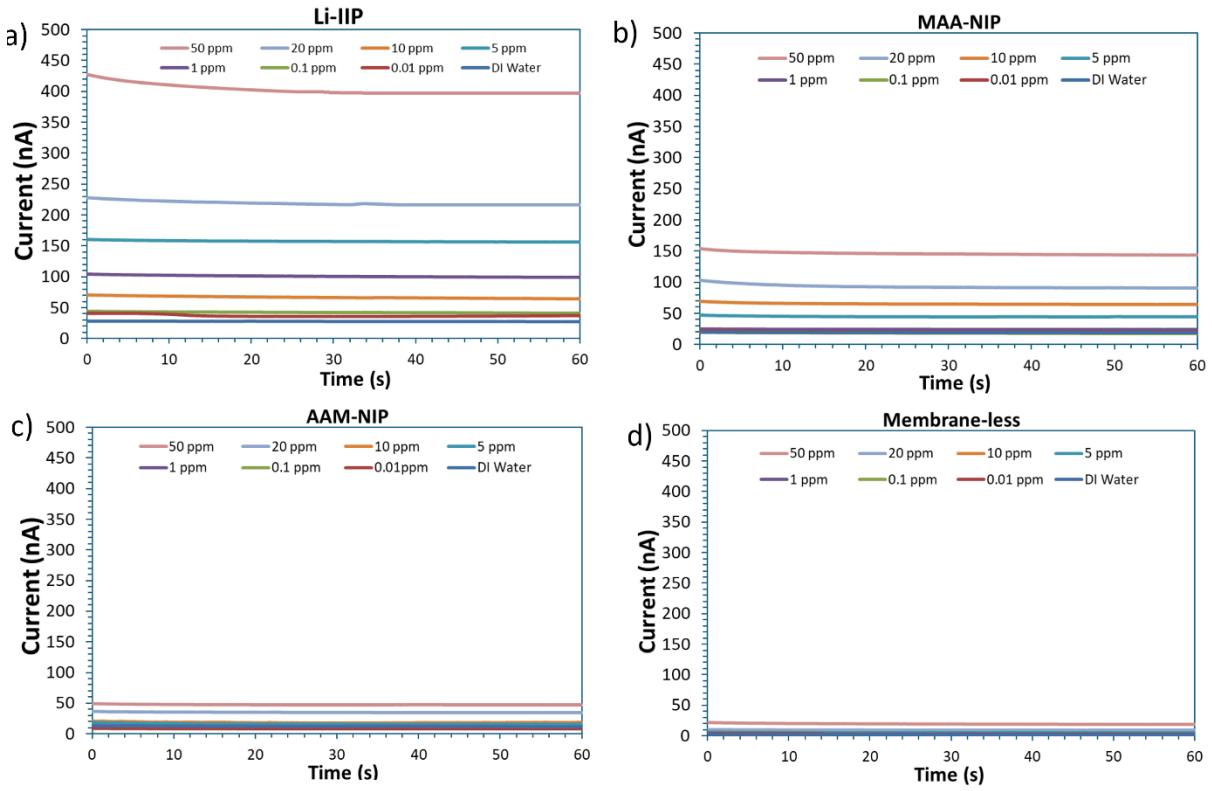

Fig. 6-2 Chronoamperometric responses of different microfluidic sensors to lithium chloride. Chronoamperometric responses of devices containing (a) Li-IIP membrane, (b) MAA-NIP membrane, and (c) AAM-NIP membrane is compared to that of (d) membrane-less sensors. Water samples containing 0–50 ppm concentrations of LiCl as shown in legends were used.

Each device configuration in Fig. 6-2 exhibited a distinct stabilization behavior and current response ranges, reflecting the differences in Li ion affinity and binding mechanisms. The Li-IIP membrane demonstrated the strongest response, stabilizing within 30 s at the highest LiCl concentration. It exhibited a stabilized current response range of 27 to 400 nA, indicating heightened sensitivity to Li ions, even at low concentrations. This performance is attributed to the combined effects of monomer affinity from MAA, contribution from 12C4 capturing ligands, and the selective binding sites created during the imprinting. The relatively long stabilization time is

due to the need for Li ions to diffuse into the imprinted sties and interact with the polymer matrix before reaching equilibrium.

In contrast, the membrane-less sensor stabilized more quickly within 3s, with a response range of 2.4 to 18 nA. This rapid stabilization suggests that Li ions interact primarily with the electrode surface rather than a structured binding network as in the membrane-integrated configuration. This very low current response to Li ions in the membrane-less sensor, even lower than the NIP membranes, underscores the importance of membrane integration in enhancing ion exchange and improving sensitivity. The low response in the membrane-less sensor can be attributed to the lack of specialized binding sites, leading to weaker ion adsorption and lower charge transfer efficiency. The MAA-NIP membrane, synthesized without Li-ion templating, stabilized at ~12 s at the highest LiCl concentration and exhibited a current response range of 14 to 150 nA. This response was notably lower than that of the Li-IIP membrane, underscoring the role of template-induced binding site formation in improving sensor performance. However, the MAA-NIP membrane still outperformed the membrane-less sensor, suggesting that Li-ion interaction was facilitated by electrostatic attraction from the carboxyl groups of MAA and weak crown ether affinity from residual 12C4 ligands. This observation prompted an investigation into the role of the carboxylic acid groups in MAA, which might be acting as ion-exchange sites, as previously reported in related studies [223]. To explore this hypothesis, we replaced MAA with AAM, a neutral monomer, lacking carboxylic acid groups. The resulting AAM-NIP membrane stabilized around within 3.5s at the highest LiCl concentration, and exhibited a current response range of 8 to 48 nA-similar to the membrane-less sensor. The significantly reduced current response suggests that removing the carboxyl functionality drastically weakened Li-ion interactions, reinforcing the role of MAA as a key ion-exchange component in the sensor's design.

The current ranges presented in Fig. 6-2 provide a comparative view of sensor performance under controlled flow conditions, underscoring the importance of functional monomers and template-driven selectivity in enhancing the sensitivity of LiCl detection. The stabilized current values at t = 60 s, the point at which each sensor's response reached a plateau, were used to construct the dose-response curves in Fig. 6-3 to illustrate the dose-dependent responses of each configuration.

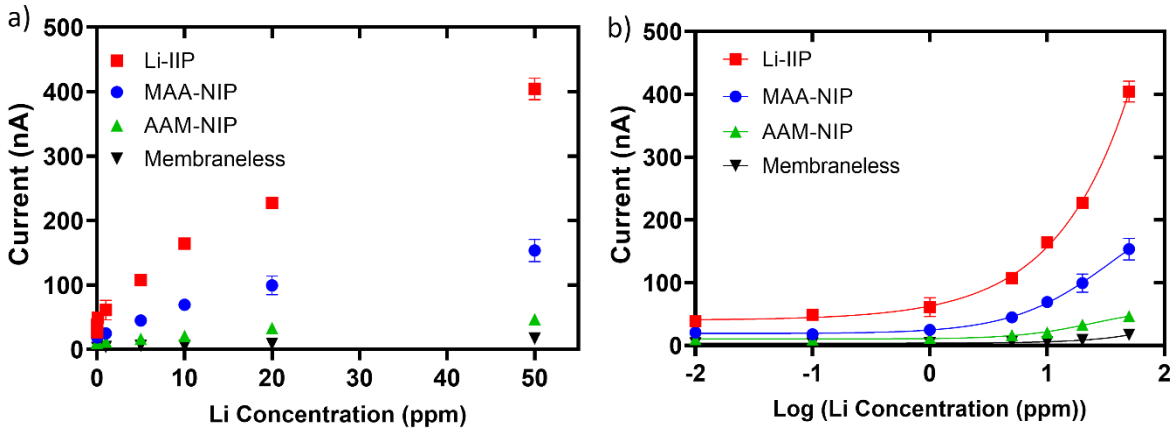

Fig. 6-3 Lithium dose-response curves of various microfluidic sensors using LiCl in water samples. Chronoamperometric currents as a function of Li ion concentration are shown in (a) x-y linear format in 0-50 ppm LiCl concentration, and (b) x-log, y-linear format at lower concentrations. Data was collected from four microfluidic sensor configurations: Li-IIP, MAA-NIP, and AAM-NIP-membraned ones and control membrane-less sensors. Each experiment was performed in triplicate using three replicate devices. Error bars represent the standard deviation (SD).

Table 6-1 presents a comparative summary of the detection performance of the Li-IIP, MAA-NIP, AAM-NIP, and Membrane-less sensors, highlighting differences in their LOD, LOQ, sensitivity, and goodness of fit (R^2).

Table 6-1. Performance metrics of microfluidic Li ion sensor configurations based on Fig. 6-3

Sensor	**I(x) fit to dose-response curve*** **(nA)**	**R^2 of I(x)**	**LOD (ppb)**	**LOQ (ppb)**	**Sensitivity # (nA/ppm)**
IIP	$70.89\ (x - 0.08395)^{0.38988}$	0.995	168	185	11.6
MAA-NIP	$17.99 + 8.87(x - 0.1)^{0.70943}$	0.973	277	856.8	5.4
AAM-NIP	$13.65\ +\ 1.46\ (x)^{0.78213}$	0.998	2690	13288	1.3
Membrane-less	$2.16\ (1 + x)^{0.50746}$	0.926	1140	1638	0.5

* I is the sensor's current output in nA and x is Li ion concentration in ppm

Sensitivities of these non-linear functions were measured using linear fits across 0.1–5 ppm.

The Li-IIP sensor exhibited the lowest LOD (168 ppb) and LOQ (185 ppb), along with the highest sensitivity (11.6 nA/ppm), demonstrating its superior detection capability. The sensor reproducibility assessed via testing three devices per condition in triplicate measurements also showed a high precision with a maximum coefficient of variation of 4.1%. This performance is attributed to the presence of ion-imprinted binding sites that enhance Li selectivity. Further investigation into the role of 12C4 in enhancing ion recognition and binding within the Pb-IIP membrane is presented in Supplementary Section 5 of our manuscript[4] . In contrast, the MAA-NIP sensor showed a 64.9% higher LOD, a 4.6-fold higher LOQ, and a 53.4% lower sensitivity compared to the Li-IIP, emphasizing the role of imprinting in improving Li detection. The AAM-NIP sensor performed even worse, with a 16-fold higher LOD, a 71.8-fold higher LOQ, and an 88.8% lower sensitivity, indicating the crucial role of carboxyl groups in Li detection. The membrane-less sensor, lacking both imprinting and functional monomers, had a 6.8-fold higher

LOD and an 8.9-fold higher LOQ than the Li-IIP, with sensitivity reduced by 95.7%, demonstrating the necessity of both molecular imprinting and monomer affinity for effective detection.

These results underscore the advantages of the Li-IIP membrane, which combines imprinting-induced selectivity with functional monomer interactions to achieve high sensitivity and low detection limits. Its strong performance in Li detection highlights its potential for real-world water quality monitoring applications.

6.3.3. Specificity and Selectivity Characteristics of the Li-IIP Membrane Sensor

6.3.3.1. Specificity Study

To evaluate the specificity of the Li-IIP membrane-integrated sensor, we assessed its response to closely related salt ions, namely NaCl and KCl, under the same conditions as the LiCl quantification studies. NaCl and KCl were selected due to their structural and ionic similarities to LiCl, including comparable ionic radii and charge states, which make them ideal for benchmarking specificity [224]. We hypothesized that the sensor would demonstrate a significantly higher sensitivity to LiCl than to NaCl and KCl due to the tailored binding sites in the ion-imprinted polymer membrane. The results of this investigation for various analyte concentrations are summarized in Fig. 6-4.

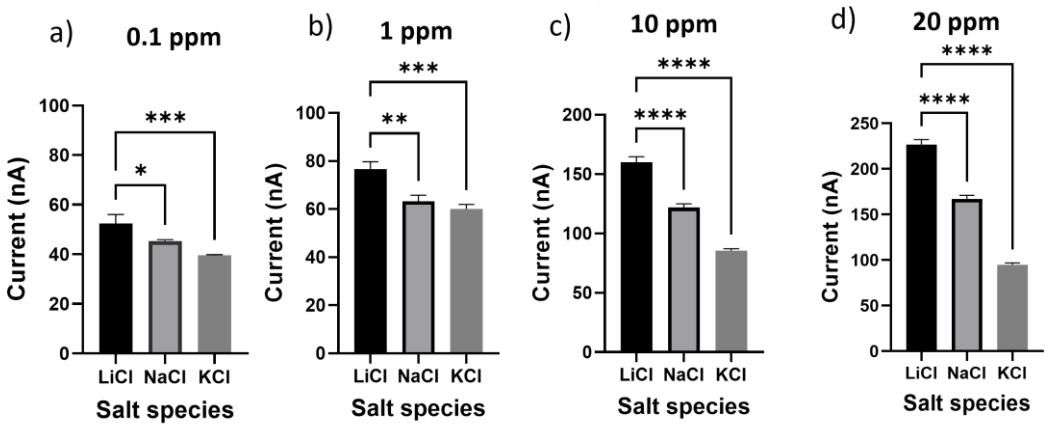

*Fig. 6-4 Specificity of the Li-IIP microfluidic sensor. Comparison of sensor responses to LiCl, NaCl, and KCl at concentrations of (a) 0.1 ppm, (b) 1 ppm, (c) 10 ppm, and (d) 20 ppm, with statistical significance indicated as follows: * ($p < 0.05$), ** ($p < 0.01$), *** ($p < 0.001$), and **** ($p < 0.0001$).*

At 0.1 ppm (Fig. 6-4a), the sensor's response to LiCl was 15.4% higher than that of NaCl ($p < 0.05$) and 29.3% higher than that of KCl ($p < 0.001$). At 1 ppm, the response to LiCl was 13.7% higher than that of NaCl ($p < 0.01$) and 19.6% higher than that of KCl ($p < 0.001$). At this low concentration, the differences in current responses are relatively modest. This can be attributed to the low binding site saturation in the imprinted polymer, where the competition between Li^+, Na^+, and K^+ for the active sites is minimal due to the low ion availability. Additionally, at such low concentrations, even non-imprinted polymer regions may facilitate non-specific adsorption, leading to small differences in responses among the three ions.

At 10 ppm, the LiCl response was 31.5% higher than that of NaCl ($p < 0.0001$) and 86.8% higher than that of KCl ($p < 0.0001$). The increase in specificity relative to 0.1 and 1 ppm can be attributed to more significant ion–polymer interactions as a larger number of Li^+ ions interact with the imprinted sites. The superior interaction of Li^+ relative to Na^+ and K^+ at this concentration indicates the increased utilization of ion-imprinted recognition sites, which have a higher binding affinity for Li^+ due to the imprinting process.

At 20 ppm, the response to LiCl was 35.5% higher than that of NaCl ($p < 0.0001$) and 138.8% higher than that of KCl ($p < 0.0001$). At this concentration, the imprinted polymer achieves optimal specificity as the binding sites are fully utilized. This result underscores the critical role of the ion-imprinting process, as the Li-IIP membrane demonstrated a clear preference for Li^+ ions compared to its closely related counterparts. The significant differences in sensor responses at higher concentrations reflect the saturation of non-specific sites for Na^+ and K^+, while the imprinted sites continue to exhibit high affinity for Li^+. The carboxylic acid groups in the Li-IIP membrane contribute to non-specific ion exchange with Na^+ and K^+, influencing their observed current responses. However, the imprinted sites exhibit a far greater affinity for Li^+, leading to significantly higher selectivity. These results confirm the effectiveness of the ion-imprinting process in creating selective recognition sites for Li ions.

Overall, the specificity study demonstrates that the Li-IIP membrane sensor exhibits significantly higher responsiveness to Li^+ than to Na^+ and K^+, particularly at higher concentrations. Although some interactions with Na^+ and K^+ occur due to non-specific ion exchange, their responses remain substantially lower than that of Li^+, reinforcing the membrane's selectivity for Li detection.

6.3.3.2. Selectivity Study

To evaluate the selectivity of the Li-IIP sensor, we conducted experiments measuring its differential response to Li^+ ions in multi-ion mixtures containing LiCl, NaCl, and KCl ions. Three scenarios were simulated with multiplex ion solutions: (i) equal proportions (LiCl: NaCl: KCl at 10 ppm total concentration in a 1:1:1 ratio), (ii) Li-dominant (LiCl: NaCl: KCl at 10 ppm total concentration in a 2:1:1 ratio), and (iii) a competitive environment (LiCl: NaCl: KCl at 10 ppm total concentration in a 1:2:2 ratio). The Li-IIP sensor responses to 10 ppm LiCl, NaCl, or KCl alone served as control for comparative analysis. This approach allowed for an assessment of the sensor's

selectivity in varying, multi-ion water conditions, where competition among ions could impact detection accuracy. The results of the study are summarized in Fig. 6-5.

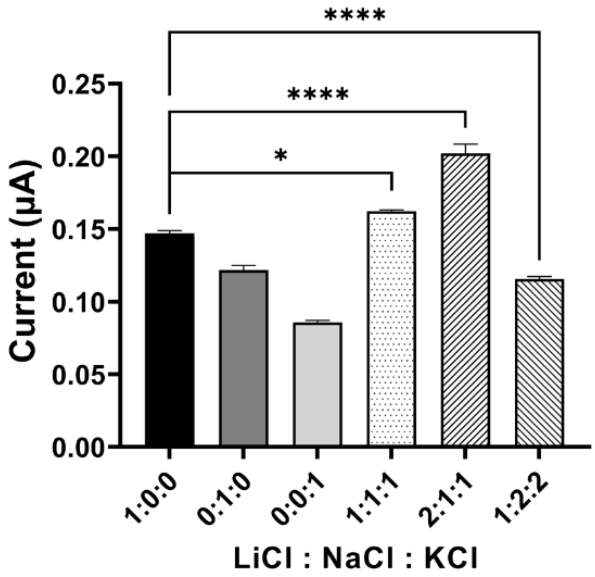

*Fig. 6-5 Selectivity of the Li-IIP microfluidic sensor. Solutions of LiCl, NaCl, and KCl in ratios of 1:1:1, 2:1:1, and 1:2:2 were tested, with a total concentration of 10 ppm. Error bars represent standard deviations, and statistical significance indicated as follows: * ($p < 0.05$), ** ($p < 0.01$), *** ($p < 0.001$), and **** ($p < 0.0001$).*

In the 1:1:1 mixture (equal proportions), the sensor exhibited an 11% higher response than LiCl alone, suggesting an increase due to the presence of non-target ions. This increase is likely attributed to the cumulative contribution of non-specific binding and the partial saturation of the imprinted polymer sites by competing ions. Conversely, in the Li-dominant solution (2:1:1), the sensor demonstrated a 37% higher response than Li^+ alone ($p < 0.0001$) and a 25% higher response than the equal proportion solution. This marked increase reflects the greater availability of Li^+ ions, resulting in enhanced binding interactions within the imprinted polymer binding sites and higher sensor response. In the competitive solution (1:2:2), the sensor showed a 21% lower response than Li^+ alone, and a 29% lower response than the equal proportion solution. The attenuated response is

attributed to the elevated concentration of interfering ions (Na^+ and K^+), which likely compete for non-specific binding sites within the polymer matrix, thereby reducing the sensor's overall sensitivity to Li^+.

Overall, the elevated response to Li^+ across all tested scenarios underscores the Li-IIP membrane's selectivity for Li^+, even in the presence of potential interfering ions. Although Na^+ and K^+ produced measurable signals in all conditions, these signals likely resulted from weak, nonspecific interactions with the imprinted polymer matrix and simultaneous capacitive charging of the electrode. These effects, however, did not compromise the sensor's selectivity. The Li-IIP membrane's ability to reliably show heightened response in the LiCl-dominant scenario and reduced response in the competitive ion-dominant scenarios within complex ion mixtures highlights its potential for Li detection in real-world water monitoring applications. Further information on the attenuation characteristics of other competing ions, in an interference study, can be found in Supplementary File Section 6 of our manuscript[4].

6.3.4. Li Detection in Real Water

To evaluate the performance of the Li-IIP microfluidic sensor under realistic water matrix conditions, water samples were collected from a public tap on York University's campus and used without further filtration or purification. To reach the sensor's dynamic response range, LiCl was spiked into diluted tap water samples at concentrations of C_1=20, 30, and 40 ppm, following the same chronoamperometry measurement protocol as described for DI water testing. The I(x) fit to the dose-response curve of the Li-IIP sensor in Table 1 was then used to determine the detected concentration of Li^+ (C_2). Experiments were repeated in triplicate and the sensor's recovery percentage was calculated as shown in Table 6-2.

Table 6-2 Recovery of lithium ions from spiked tap water samples using the Li-IIP microfluidic sensor

Spiked Li^+ Concentration C_1 (ppm)	Detected Li^+ Concentration C_2 (ppm)	Standard Deviation (ppm)	Recovery* (%)	RSD # (%)
0	7.33	0.0015	N/A	N/A
20	21.04	0.0046	68.53	1.98
30	29.61	0.0045	74.25	1.70
40	44.77	0.0094	93.60	3.00

* $Recovery\ (\%) = \frac{C_2 - C_{1,Blank}}{C_1} \times 100$, *where* $C_{1,Blank} = 7.33\ ppm$ *(baseline).*
 # RSD: Relative standard deviation.

As shown in Table 6-2, the sensor demonstrated recoveries of ~69 to 94% across the spiking range, with RSD values consistently below 3%. These results show that the Li-IIP sensor maintains reliable performance in real tap water matrices and is capable of detecting lithium ions in the presence of common background ions.

6.4. Conclusion

In this chapter, a lithium ion-imprinted polymer (Li-IIP) membrane was successfully integrated into a microfluidic electrochemical sensor for selective detection of lithium in aqueous environments. The membrane was synthesized in situ via UV photopolymerization using methacrylic acid and 12-crown-4, forming selective recognition sites that enabled direct Li^+–membrane interaction without electrode surface modification. The Li-IIP sensor demonstrated a sensitivity of 11.6 ± 0.1 nA/ppm, an LOD of 168 ppb, and an LOQ of 185 ppb—marked improvements over MAA-NIP, AAM-NIP, and membrane-less controls. Specificity studies

confirmed enhanced responses to Li^+ compared to Na^+ and K^+, while selectivity tests in multi-ion mixtures showed up to 37% stronger responses under Li-dominant conditions. Interference studies indicated minimal suppression from background salts, with KCl and KNO_3 causing the highest but manageable signal reductions. Validation in unfiltered tap water yielded recovery rates between 69% and 94% for 20–40 ppm Li^+ spikes, with RSD below 5%, confirming the sensor's reliability in real water matrices. These results demonstrate the potential of the Li-IIP microfluidic platform for accurate, low-cost lithium detection in environmental and industrial contexts. Future work will focus on optimizing membrane formulation and expanding detection capabilities to additional target ions.

Chapter 7

Summary of Thesis and Prospects

7.1 Thesis Summary

This thesis focused on the development of low-cost, stand-alone IIP membrane-integrated electrochemical microfluidic sensors for the selective and sensitive detection of target ions, namely sodium (Na^+), lead (Pb^{2+}), and lithium (Li^+), in water. The principal objective was to design, fabricate, and characterize stand-alone membrane-based sensors that address some of the challenges associated with conventional electrode-modified systems, thereby contributing to more reproducible, scalable, and portable sensing platforms for real-world applications.

7.1.1 ISP Membrane Integration and Proof-of-Concept for NaCl Detection

A non-imprinted ion-selective polymer (ISP) membrane sensor was first developed to demonstrate the feasibility of integrating a polymer membrane between electrodes within a microfluidic chip. This proof-of-concept study established that the membrane platform allows for robust electrochemical detection of NaCl, showing improved signal intensity and sensitivity compared to membrane-less configurations. This chapter validated the design and fabrication processes, including electrode injection, photopolymerization, and channel layout, and demonstrated that ion diffusion through the membrane can generate measurable and reproducible chronoamperometric responses. These results confirmed the technical viability of the membrane-integrated sensing platform for low-concentration salt detection (Chapter 3).

7.1.2 Sodium Ion-Imprinted Polymer (Na-IIP) Sensor

Building on the previous design, a sodium-selective IIP membrane was synthesized in-situ using 15-crown-5 and methacrylic acid to form selective binding sites for Na^+ ions. The sensor exhibited a limit of detection (LOD) of 58 ppb and a sensitivity of 9.1 nA/ppm, significantly outperforming the NIP and membrane-less controls. Specificity tests revealed sodium responses exceeded those for KCl and KNO_3 by up to 129.7% at 1 ppm. Validation in tap water showed reliable recoveries using matrix-matched calibration. This study demonstrated the potential of IIP-enhanced microfluidic sensors for selective ion monitoring in complex ionic backgrounds, fulfilling the third objective of the thesis (Chapter 4).

7.1.3 Lead Ion-Imprinted Polymer (Pb-IIP) Sensor

A Pb^{2+}-selective IIP membrane was synthesized using methacrylic acid and 8-hydroxyquinoline as functional monomers and ligands, respectively. The sensor demonstrated high performance with an LOD of 7.3 ppb and a sensitivity of 6.1 nA/ppm, surpassing the membrane-less and NIP counterparts by 6.1- to 13-fold. Statistical analysis confirmed superior specificity for Pb^{2+} compared to Cd^{2+} and Zn^{2+}. In spiked tap water, recovery values ranged from 96.6% to 109.0% with RSDs <7%. This chapter showcased the potential for scalability and selectivity of the Pb-IIP sensor for environmental lead detection (Chapter 5).

7.1.4 Lithium Ion-Imprinted Polymer (Li-IIP) Sensor

The final study introduced a Li^+-specific IIP membrane formed with methacrylic acid and 12-crown-4, tailored for lithium detection in both simple and complex matrices. The Li-IIP sensor

achieved an LOD of 168 ppb, an LOQ of 185 ppb, and a sensitivity of 11.6 nA/ppm. It significantly outperformed AAM-NIP, MAA-NIP, and membrane-less configurations. Specificity and selectivity analyses showed Li^+ responses were 25–74% higher in Li-dominant mixtures compared to mixed-ion conditions. Recovery studies in unfiltered tap water returned values of 68.5–93.6%, confirming real-world applicability. This final study further extended the platform's adaptability to a wider range of critical contaminants (Chapter 6).

7.2 Thesis Prospects

This thesis establishes a novel, stand-alone IIP membrane-integrated microfluidic sensor architecture for sensitive and selective detection of metal ions in water. While the platform demonstrates strong potential across various analytes, continued optimization is essential to extend its utility across more complex real-world matrices, ensure broader adaptability, and support scalable deployment.

7.2.1 Thesis Prospects

Despite the promising outcomes demonstrated by the ISP and IIP-based sensor platforms, several limitations and challenges must be acknowledged:

First, although the use of in-situ synthesized, stand-alone polymer membranes circumvents the complexities of electrode surface modifications, it still requires precise control of UV photopolymerization conditions and membrane formulation. Small deviations in curing time, monomer ratios, or chamber alignment can introduce variability in membrane thickness and ion-

binding site density, potentially impacting reproducibility across devices. Future studies should explore real-time fabrication monitoring and closed-loop process control to minimize such variations.

Second, while the selectivity of each IIP membrane was successfully validated against specific interfering ions and municipal tap water, broader interference studies involving complex matrices such as industrial wastewater or seawater will be needed for environmental applications. These matrices may introduce unpredictable fouling agents, pH fluctuations, or ionic competition that could affect membrane stability or alter electrochemical responses. Future work should incorporate antifouling coatings, pH buffers, or pretreatment modules to improve robustness.

Third, although chronoamperometry was effective for signal acquisition, it does not offer major molecular-level insight into binding kinetics or thermodynamics. Complementary characterization techniques such as electrochemical impedance spectroscopy (EIS) or surface plasmon resonance (SPR) could provide deeper understanding of binding mechanisms and guide membrane design optimization.

Fourth, current designs target one analyte per sensor membrane. While this simplifies interpretation, it also limits throughput and versatility. Future efforts could pursue spatial multiplexing by integrating multiple IIP membranes into distinct chambers on the same chip, each tailored to a different ion, enabling simultaneous multi-analyte detection.

Lastly, transitioning from laboratory validation to field deployment will require integrating the sensor chip into a fully functional Point-of-Need (PoN) platform. This includes coupling with portable electrochemical readers, microfluidic flow controllers, wireless data logging, and robust

packaging for field resilience. Low-cost manufacturing methods such as roll-to-roll or injection molding could be investigated for large-scale production.

In summary, while the proposed platform has proven highly effective for trace ion detection in controlled and tap water conditions, future research should prioritize enhancing device reproducibility, interference resilience, multiplexing capabilities, and real-world integration to support widespread deployment in environmental, industrial, and healthcare settings.

References

1. Ateia M, Wei H, Andreescu S (2024) Sensors for Emerging Water Contaminants: Overcoming Roadblocks to Innovation. Environ Sci Technol 58:2636–2651. https://doi.org/10.1021/acs.est.3c09889

2. Fernández-Luqueño F, López-Valdez F, Gamero-Melo P, et al (2013) Heavy metal pollution in drinking water - a global risk for human health: A review. African Journal of Environmental Science and Technology 7:567–584

3. Water pollution | Definition, Causes, Effects, Solutions, Examples, & Facts | Britannica. https://www.britannica.com/science/water-pollution. Accessed 29 Jul 2023

4. Manoiu V-M, Kubiak-Wójcicka K, Craciun A-I, et al (2022) Water Quality and Water Pollution in Time of COVID-19: Positive and Negative Repercussions. Water 14:1124. https://doi.org/10.3390/w14071124

5. US EPA O (2014) Regulatory Determination 1 Support Documents for Sodium. https://www.epa.gov/ccl/regulatory-determination-1-support-documents-sodium. Accessed 9 Jan 2024

6. Canada H (1997) Guidelines for Canadian Drinking Water Quality: Guideline Technical Document – Sodium. https://www.canada.ca/en/health-canada/services/publications/healthy-living/guidelines-canadian-drinking-water-quality-guideline-technical-document-sodium.html. Accessed 10 Jan 2024

7. (1974) Outlines of analytical methods : a guide to the occurance, significance, sampling and analysis of chemical and microbial parameters in water /. Ontario Ministry of the Environment

8. Subramanian KS, Meranger JC (1984) A survey for sodium, potassium, barium, arsenic and selenium in canadian drinking water supplies. Atomic Spectroscopy

9. (2023) Sodium in Drinking Water. https://www.mississippimills.ca/en/sodium-in-drinking-water.aspx. Accessed 7 Dec 2023

10. Salt and Drinking Water. https://www.health.ny.gov/environmental/water/drinking/salt_drinkingwater.htm. Accessed 7 Dec 2023

11. Doré E, Lytle DA, Wasserstrom L, et al (2021) Field analyzers for lead quantification in drinking water samples. Critical Reviews in Environmental Science and Technology 51:2357–2388. https://doi.org/10.1080/10643389.2020.1782654

12. World Health Organization (2011) Guidelines for drinking-water quality

13. WASSERSTROM LW, MILLER SA, TRIANTAFYLLIDOU S, et al (2017) Scale Formation Under Blended Phosphate Treatment for a Utility With Lead Pipes. J Am Water Works Assoc 109:E464–E478. https://doi.org/10.5942/jawwa.2017.109.0121

14. (2024) Flint Water Crisis: Everything You Need to Know. https://www.nrdc.org/stories/flint-water-crisis-everything-you-need-know. Accessed 5 Mar 2025

15. Phan K, Sthiannopkao S, Kim K-W, et al (2010) Health risk assessment of inorganic arsenic intake of Cambodia residents through groundwater drinking pathway. Water Research 44:5777–5788. https://doi.org/10.1016/j.watres.2010.06.021

16. Hughes MF (2002) Arsenic toxicity and potential mechanisms of action. Toxicology Letters 133:1–16. https://doi.org/10.1016/S0378-4274(02)00084-X

17. Wani AL, Ara A, Usmani JA (2016) Lead toxicity: a review. Interdisciplinary Toxicology 8:55–64. https://doi.org/10.1515/intox-2015-0009

18. Gillis BS, Arbieva Z, Gavin IM (2012) Analysis of lead toxicity in human cells. BMC Genomics 13:344. https://doi.org/10.1186/1471-2164-13-344

19. Bernhoft RA (2013) Cadmium Toxicity and Treatment. The Scientific World Journal 2013:e394652. https://doi.org/10.1155/2013/394652

20. Moulis J-M, Thévenod F (2010) New perspectives in cadmium toxicity: an introduction. Biometals 23:763–768. https://doi.org/10.1007/s10534-010-9365-6

21. Canada H (2018) Copper in drinking water. https://www.canada.ca/en/health-canada/programs/consultation-copper-drinking-water/document.html. Accessed 6 Mar 2025

22. Selvaraj S, Krishnaswamy S, Devashya V, et al (2011) Investigations on Membrane Perturbation by Chrysin and Its Copper Complex Using Self-Assembled Lipid Bilayers. Langmuir 27:13374–13382. https://doi.org/10.1021/la2029356

23. Kilfoy BA, Zhang Y, Park Y, et al (2011) Dietary nitrate and nitrite and the risk of thyroid cancer in the NIH-AARP Diet and Health Study. Int J Cancer 129:160–172. https://doi.org/10.1002/ijc.25650

24. Chen J, Wu H, Qian H, Gao Y (2017) Assessing Nitrate and Fluoride Contaminants in Drinking Water and Their Health Risk of Rural Residents Living in a Semiarid Region of Northwest China. Expo Health 9:183–195. https://doi.org/10.1007/s12403-016-0231-9

25. Agrawal A, Pandey RS, Sharma B (2010) Water Pollution with Special Reference to Pesticide Contamination in India. Journal of Water Resource and Protection 2:432–448. https://doi.org/10.4236/jwarp.2010.25050

26. Li S, Liu Y, Wu Y, et al (2022) Antibiotics in global rivers. NSO 1:20220029. https://doi.org/10.1360/nso/20220029

27. Khan S, Naushad Mu, Govarthanan M, et al (2022) Emerging contaminants of high concern for the environment: Current trends and future research. Environmental Research 207:112609. https://doi.org/10.1016/j.envres.2021.112609

28. Zwiener C, Frimmel FH (2004) LC-MS analysis in the aquatic environment and in water treatment technology--a critical review. Part II: Applications for emerging contaminants and related pollutants, microorganisms and humic acids. Anal Bioanal Chem 378:862–874. https://doi.org/10.1007/s00216-003-2412-1

29. Rodriguez-Mozaz S, Lopez de Alda MJ, Barceló D (2007) Advantages and limitations of on-line solid phase extraction coupled to liquid chromatography-mass spectrometry technologies versus biosensors for monitoring of emerging contaminants in water. J Chromatogr A 1152:97–115. https://doi.org/10.1016/j.chroma.2007.01.046

30. Biosensor - Principle, Components, Types & Their Applications. https://www.elprocus.com/what-is-a-biosensor-types-of-biosensors-and-applications/. Accessed 17 Jun 2023

31. Thavarajah W, Verosloff MS, Jung JK, et al (2020) A primer on emerging field-deployable synthetic biology tools for global water quality monitoring. npj Clean Water 3:1–10. https://doi.org/10.1038/s41545-020-0064-8

32. Sri VR, Shwetharani R, Mohammed J, et al (2022) Review on Electrochemical Sensing of Triclosan using Nanostructured Semiconductor Materials. ChemElectroChem 9:e202101664. https://doi.org/10.1002/celc.202101664

33. Hara TO, Singh B (2021) Electrochemical Biosensors for Detection of Pesticides and Heavy Metal Toxicants in Water: Recent Trends and Progress. ACS EST Water 1:462–478. https://doi.org/10.1021/acsestwater.0c00125

34. Yilmaz E, Majidi D, Ozgur E, Denizli A (2015) Whole cell imprinting based Escherichia coli sensors: A study for SPR and QCM. Sensors and Actuators B: Chemical 209:714–721. https://doi.org/10.1016/j.snb.2014.12.032

35. Carrascosa LG, Huertas CS, Lechuga LM (2016) Prospects of optical biosensors for emerging label-free RNA analysis. TrAC Trends in Analytical Chemistry 80:177–189. https://doi.org/10.1016/j.trac.2016.02.018

36. Huertas CS, Lechuga LM (2017) Editor's Pick: Simple, Low-Cost, and Timely Optical Biosensors for the Detection of Epigenetic Biomarkers: The Future of Cancer Diagnosis. EMJ 5:54–61. https://doi.org/10.33590/emjoncol/10311704

37. Banakar M, Hamidi M, Khurshid Z, et al (2022) Electrochemical Biosensors for Pathogen Detection: An Updated Review. Biosensors (Basel) 12:927. https://doi.org/10.3390/bios12110927

38. Potentiostat/Galvanostat Electrochemical Instrument Basics Gamry Instruments. https://www.gamry.com/application-notes/instrumentation/potentiostat-fundamentals/. Accessed 14 Jul 2023

39. (2002) Allen J. Bard and Larry R. Faulkner, Electrochemical Methods: Fundamentals and Applications, New York: Wiley, 2001, 2nd ed. Russian Journal of Electrochemistry 38:1364–1365. https://doi.org/10.1023/A:1021637209564

40. Justino CIL, Freitas AC, Pereira R, et al (2015) Recent developments in recognition elements for chemical sensors and biosensors. TrAC Trends in Analytical Chemistry 68:2–17. https://doi.org/10.1016/j.trac.2015.03.006

41. Mohd Said NA, Ogurtsov V, Herzog G (2014) ELECTROCHEMICAL BIOSENSOR BASED ON MICROFABRICATED ELECTRODE ARRAYS FOR LIFE SCIENCES APPLICATIONS

42. Cao Y, Feng T, Xu J, Xue C (2019) Recent advances of molecularly imprinted polymer-based sensors in the detection of food safety hazard factors. Biosensors and Bioelectronics 141:111447. https://doi.org/10.1016/j.bios.2019.111447

43. Wang L, Pagett M, Zhang W (2023) Molecularly imprinted polymer (MIP) based electrochemical sensors and their recent advances in health applications. Sensors and Actuators Reports 5:100153. https://doi.org/10.1016/j.snr.2023.100153

44. Jaywant SA, Arif KM (2019) A Comprehensive Review of Microfluidic Water Quality Monitoring Sensors. Sensors (Basel) 19:4781. https://doi.org/10.3390/s19214781

45. Seguro I, Pacheco JG, Delerue-Matos C (2021) Low Cost, Easy to Prepare and Disposable Electrochemical Molecularly Imprinted Sensor for Diclofenac Detection. Sensors (Basel) 21:1975. https://doi.org/10.3390/s21061975

46. Wang X, Zhou J, Wang H (2024) Bioreceptors as the key components for electrochemical biosensing in medicine. Cell Reports Physical Science 5:101801. https://doi.org/10.1016/j.xcrp.2024.101801

47. Kadam US, Hong JC (2022) Advances in aptameric biosensors designed to detect toxic contaminants from food, water, human fluids, and the environment. Trends in Environmental Analytical Chemistry 36:e00184. https://doi.org/10.1016/j.teac.2022.e00184

48. Sahu S, Roy R, Anand R (2022) Harnessing the Potential of Biological Recognition Elements for Water Pollution Monitoring. ACS Sens 7:704–715. https://doi.org/10.1021/acssensors.1c02579

49. Warner J, Andreescu S (2016) An acetylcholinesterase (AChE) biosensor with enhanced solvent resistance based on chitosan for the detection of pesticides. Talanta 146:279–284. https://doi.org/10.1016/j.talanta.2015.08.030

50. Azzouz A, Hejji L, Kumar V, Kim K-H (2023) Nanomaterials-based aptasensors: An efficient detection tool for heavy-metal and metalloid ions in environmental and biological samples. Environmental Research 238:117170. https://doi.org/10.1016/j.envres.2023.117170

51. Sala A, Brisset H, Margaillan A, et al (2022) Electrochemical sensors modified with ion-imprinted polymers for metal ion detection. TrAC Trends in Analytical Chemistry 148:116536. https://doi.org/10.1016/j.trac.2022.116536

52. Guan G, Liu B, Wang Z, Zhang Z (2008) Imprinting of Molecular Recognition Sites on Nanostructures and Its Applications in Chemosensors. Sensors 8:8291–8320. https://doi.org/10.3390/s8128291

53. Maksymiuk K, Stelmach E, Michalska A (2020) Unintended Changes of Ion-Selective Membranes Composition—Origin and Effect on Analytical Performance. Membranes 10:266. https://doi.org/10.3390/membranes10100266

54. Bühlmann P, Pretsch E, Bakker E (1998) Carrier-Based Ion-Selective Electrodes and Bulk Optodes. 2. Ionophores for Potentiometric and Optical Sensors. Chem Rev 98:1593–1688. https://doi.org/10.1021/cr970113+

55. Darestani-Farahani M, Montealegre IM, Gilavan MT, et al (2024) A highly sensitive ion-selective chemiresistive sensor for online monitoring of lead ions in water. Analyst 149:2915–2924. https://doi.org/10.1039/D4AN00159A

56. Malitesta C, Mazzotta E, Picca RA, et al (2012) MIP sensors--the electrochemical approach. Anal Bioanal Chem 402:1827–1846. https://doi.org/10.1007/s00216-011-5405-5

57. Altintas Z, Akgun M, Kokturk G, Uludag Y (2018) A fully automated microfluidic-based electrochemical sensor for real-time bacteria detection. Biosensors and Bioelectronics 100:541–548. https://doi.org/10.1016/j.bios.2017.09.046

58. Kim M, Jung T, Kim Y, et al (2015) A microfluidic device for label-free detection of Escherichia coli in drinking water using positive dielectrophoretic focusing, capturing, and impedance measurement. Biosensors and Bioelectronics 74:1011–1015. https://doi.org/10.1016/j.bios.2015.07.059

59. Zhang Y, Li J, Jiao S, et al (2024) Microfluidic sensors for the detection of emerging contaminants in water: A review. Science of The Total Environment 929:172734. https://doi.org/10.1016/j.scitotenv.2024.172734

60. Nge PN, Rogers CI, Woolley AT (2013) Advances in Microfluidic Materials, Functions, Integration, and Applications. Chem Rev 113:2550–2583. https://doi.org/10.1021/cr300337x

61. Rai PK, Islam M, Gupta A (2022) Microfluidic devices for the detection of contamination in water samples: A review. Sensors and Actuators A: Physical 347:113926. https://doi.org/10.1016/j.sna.2022.113926

62. Raksawong P, Nurerk P, Chullasat K, et al (2019) A polypyrrole doped with fluorescent CdTe quantum dots and incorporated into molecularly imprinted silica for fluorometric determination of ampicillin. Microchim Acta 186:338. https://doi.org/10.1007/s00604-019-3447-0

63. Wang W, Mai Z, Chen Y, et al (2017) A label-free fiber optic SPR biosensor for specific detection of C-reactive protein. Sci Rep 7:16904. https://doi.org/10.1038/s41598-017-17276-3

64. Pol R, Céspedes F, Gabriel D, Baeza M (2017) Microfluidic lab-on-a-chip platforms for environmental monitoring. TrAC Trends in Analytical Chemistry 95:62–68. https://doi.org/10.1016/j.trac.2017.08.001

65. Sophocleous M, Atkinson JK (2017) A review of screen-printed silver/silver chloride (Ag/AgCl) reference electrodes potentially suitable for environmental potentiometric sensors. Sensors and Actuators A: Physical 267:106–120. https://doi.org/10.1016/j.sna.2017.10.013

66. Sartore L, Barbaglio M, Borgese L, Bontempi E (2011) Polymer-grafted QCM chemical sensor and application to heavy metal ions real time detection. Sensors and Actuators B: Chemical 155:538–544. https://doi.org/10.1016/j.snb.2011.01.003

67. L. Walsh C, M. Babin B, W. Kasinskas R, et al (2009) A multipurpose microfluidic device designed to mimic microenvironment gradients and develop targeted cancer therapeutics. Lab on a Chip 9:545–554. https://doi.org/10.1039/B810571E

68. Einav S, Gerber D, Bryson PD, et al (2008) Discovery of a hepatitis C target and its pharmacological inhibitors by microfluidic affinity analysis. Nat Biotechnol 26:1019–1027. https://doi.org/10.1038/nbt.1490

69. Gerber D, Maerkl SJ, Quake SR (2009) An in vitro microfluidic approach to generating protein-interaction networks. Nat Methods 6:71–74. https://doi.org/10.1038/nmeth.1289

70. Inci F, Saylan Y, Kojouri AM, et al (2020) A disposable microfluidic-integrated hand-held plasmonic platform for protein detection. Applied Materials Today 18:100478. https://doi.org/10.1016/j.apmt.2019.100478

71. Coluccio ML, Perozziello G, Malara N, et al (2019) Microfluidic platforms for cell cultures and investigations. Microelectronic Engineering 208:14–28. https://doi.org/10.1016/j.mee.2019.01.004

72. Dossi N, Susmel S, Toniolo R, et al (2009) Application of microchip electrophoresis with electrochemical detection to environmental aldehyde monitoring. ELECTROPHORESIS 30:3465–3471. https://doi.org/10.1002/elps.200900297

73. Safdar M, Jänis J, Sánchez S (2016) Microfluidic fuel cells for energy generation. Lab on a Chip 16:2754–2758. https://doi.org/10.1039/C6LC90070D

74. Jiang W, Tang Q, Zhu Y, et al (2024) Research progress of microfluidics-based food safety detection. Food Chemistry 138319. https://doi.org/10.1016/j.foodchem.2023.138319

75. Mou L, Jiang X (2017) Materials for Microfluidic Immunoassays: A Review. Advanced Healthcare Materials 6:1601403. https://doi.org/10.1002/adhm.201601403

76. Ren K, Zhou J, Wu H (2013) Materials for Microfluidic Chip Fabrication. Acc Chem Res 46:2396–2406. https://doi.org/10.1021/ar300314s

77. Lu J, Qin Y, Wu Y, et al (2019) Recent advances in ion-imprinted membranes: separation and detection via ion-selective recognition. Environmental Science: Water Research & Technology 5:1626–1653. https://doi.org/10.1039/C9EW00465C

78. Pan J, Yin Y, Ma Y, et al (2016) Hierarchical porous molecule/ion imprinted polymers with double specific binding sites: Combination of Pickering HIPEs template and pore-filled strategy. Chemical Engineering Journal 301:210–221. https://doi.org/10.1016/j.cej.2016.04.154

79. Fu J, Chen L, Li J, Zhang Z (2015) Current status and challenges of ion imprinting. J Mater Chem A 3:13598–13627. https://doi.org/10.1039/C5TA02421H

80. Li Y, Qiu T, Xu X (2013) Preparation of lead-ion imprinted crosslinked electro-spun chitosan nanofiber mats and application in lead ions removal from aqueous solutions. European Polymer Journal 49:1487–1494. https://doi.org/10.1016/j.eurpolymj.2013.04.002

81. Branger C, Meouche W, Margaillan A (2013) Recent advances on ion-imprinted polymers. Reactive and Functional Polymers 73:859–875. https://doi.org/10.1016/j.reactfunctpolym.2013.03.021

82. Alahi MdEE, Mukhopadhyay SC, Burkitt L (2018) Imprinted polymer coated impedimetric nitrate sensor for real- time water quality monitoring. Sensors and Actuators B: Chemical 259:753–761. https://doi.org/10.1016/j.snb.2017.12.104

83. Rao TP, Kala R, Daniel S (2006) Metal ion-imprinted polymers—Novel materials for selective recognition of inorganics. Analytica Chimica Acta 578:105–116. https://doi.org/10.1016/j.aca.2006.06.065

84. Andaç M, Özyapı E, Şenel S, et al (2006) Ion-Selective Imprinted Beads for Aluminum Removal from Aqueous Solutions. Ind Eng Chem Res 45:1780–1786. https://doi.org/10.1021/ie0512338

85. El Ouardi Y, Giove A, Laatikainen M, et al (2021) Benefit of ion imprinting technique in solid-phase extraction of heavy metals, special focus on the last decade. Journal of Environmental Chemical Engineering 9:106548. https://doi.org/10.1016/j.jece.2021.106548

86. Kazemi E, Dadfarnia S, Haji Shabani AM, Ranjbar M (2017) Synthesis, characterization, and application of a Zn (II)-imprinted polymer grafted on graphene oxide/magnetic chitosan nanocomposite for selective extraction of zinc ions from different food samples. Food Chemistry 237:921–928. https://doi.org/10.1016/j.foodchem.2017.06.053

87. Francisco JE, Feiteira FN, da Silva WA, Pacheco WF (2019) Synthesis and application of ion-imprinted polymer for the determination of mercury II in water samples. Environ Sci Pollut Res 26:19588–19597. https://doi.org/10.1007/s11356-019-05178-y

88. Mustafai FA, Balouch A, Abdullah, et al (2018) Microwave-assisted synthesis of imprinted polymer for selective removal of arsenic from drinking water by applying Taguchi statistical method. European Polymer Journal 109:133–142. https://doi.org/10.1016/j.eurpolymj.2018.09.041

89. Lenoble V, Meouche W, Laatikainen K, et al (2015) Assessment and modelling of Ni(II) retention by an ion-imprinted polymer: Application in natural samples. Journal of Colloid and Interface Science 448:473–481. https://doi.org/10.1016/j.jcis.2015.02.055

90. Jalilzadeh M, Şenel S (2016) Removal of Cu(II) ions from water by ion-imprinted magnetic and non-magnetic cryogels: A comparison of their selective Cu(II) removal performances. Journal of Water Process Engineering 13:143–152. https://doi.org/10.1016/j.jwpe.2016.08.010

91. Ma L, Qi J, Gao L, et al (2024) 18-Crown-6-ether assembly of cesium ion-imprinted polymer enabling efficiently selective separation of cs(I) from aqueous solution. Adsorption 30:1047–1057. https://doi.org/10.1007/s10450-024-00481-8

92. Luo F, Huang S, Xiong X, Lai X (2015) Synthesis and characterization of Hg(II)-ion-imprinted polymer and its application for the determination of mercury in water samples. RSC Adv 5:67365–67371. https://doi.org/10.1039/C5RA10861F

93. Xi Y, Luo Y, Luo J, Luo X (2015) Removal of Cadmium(II) from Wastewater Using Novel Cadmium Ion-Imprinted Polymers. J Chem Eng Data 60:3253–3261. https://doi.org/10.1021/acs.jced.5b00494

94. Zhou Z, Kong D, Zhu H, et al (2018) Preparation and adsorption characteristics of an ion-imprinted polymer for fast removal of Ni(II) ions from aqueous solution. Journal of Hazardous Materials 341:355–364. https://doi.org/10.1016/j.jhazmat.2017.06.010

95. Dahaghin Z, Kilmartin PA, Mousavi HZ (2020) Novel ion imprinted polymer electrochemical sensor for the selective detection of lead(II). Food Chemistry 303:125374. https://doi.org/10.1016/j.foodchem.2019.125374

96. Kumar A, Balouch A, Abdullah, Pathan AA (2019) Synthesis, adsorption and analytical applicability of Ni-imprinted polymer for selective adsorption of Ni2+ ions from the aqueous environment. Polymer Testing 77:105871. https://doi.org/10.1016/j.polymertesting.2019.04.018

97. Ghanei-Motlagh M, Taher MA (2017) Novel imprinted polymeric nanoparticles prepared by sol–gel technique for electrochemical detection of toxic cadmium(II) ions. Chemical Engineering Journal 327:135–141. https://doi.org/10.1016/j.cej.2017.06.091

98. Fuchs Y, Soppera O, Haupt K (2012) Photopolymerization and photostructuring of molecularly imprinted polymers for sensor applications—A review. Analytica Chimica Acta 717:7–20. https://doi.org/10.1016/j.aca.2011.12.026

99. Faghihian H, Adivi FG (2012) Separation and Pre-Concentration of Cu(II) Ions by a Synthesized Ion-Imprinted Polymer. Adsorption Science & Technology 30:205–215. https://doi.org/10.1260/0263-6174.30.3.205

100. Zhou X, Wang B, Wang R (2022) Insights into ion-imprinted materials for the recovery of metal ions: Preparation, evaluation and application. Separation and Purification Technology 298:121469. https://doi.org/10.1016/j.seppur.2022.121469

101. Meouche W, Laatikainen K, Margaillan A, et al (2017) Effect of porogen solvent on the properties of nickel ion imprinted polymer materials prepared by inverse suspension polymerization. European Polymer Journal 87:124–135. https://doi.org/10.1016/j.eurpolymj.2016.12.022

102. Liu W, Zhang M, Liu X, et al (2020) Preparation of Surface Ion-Imprinted Materials Based on Modified Chitosan for Highly Selective Recognition and Adsorption of Nickel Ions in Aqueous Solutions. Ind Eng Chem Res 59:6033–6042. https://doi.org/10.1021/acs.iecr.9b04755

103. Chi Z, Zhu Y, Liu W, et al (2021) Selective removal of As(III) using magnetic graphene oxide ion-imprinted polymer in porous media: Potential effect of external magnetic field. Journal of Environmental Chemical Engineering 9:105671. https://doi.org/10.1016/j.jece.2021.105671

104. Ashouri N, Mohammadi A, Hajiaghaee R, et al (2016) Preparation of a new nanoparticle Cd(II)-imprinted polymer and its application for selective separation of cadmium(II) ions from aqueous solutions and determination via inductively coupled plasma optical emission spectrometry. Desalination and Water Treatment 57:14280–14289. https://doi.org/10.1080/19443994.2015.1072742

105. Buhani, Narsito, Nuryono, Kunarti ES (2010) Production of metal ion imprinted polymer from mercapto–silica through sol–gel process as selective adsorbent of cadmium. Desalination 251:83–89. https://doi.org/10.1016/j.desal.2009.09.139

106. Hossein Beyki M, Shemirani F, Shirkhodaie M (2016) Aqueous Co(II) adsorption using 8-hydroxyquinoline anchored γ-Fe2O3@chitosan with Co(II) as imprinted ions. International Journal of Biological Macromolecules 87:375–384. https://doi.org/10.1016/j.ijbiomac.2016.02.077

107. Kuras MJ, Więckowska E (2015) Synthesis and characterization of a new copper(II) ion-imprinted polymer. Polym Bull 72:3227–3240. https://doi.org/10.1007/s00289-015-1463-8

108. Roushani M, Abbasi S, Khani H (2015) Synthesis and application of ion-imprinted polymer nanoparticles for the extraction and preconcentration of copper ions in environmental water samples. Environ Monit Assess 187:219. https://doi.org/10.1007/s10661-015-4468-8

109. Behbahani M, Bagheri A, Taghizadeh M, et al (2013) Synthesis and characterisation of nano structure lead (II) ion-imprinted polymer as a new sorbent for selective extraction and preconcentration of ultra trace amounts of lead ions from vegetables, rice, and fish samples. Food Chemistry 138:2050–2056. https://doi.org/10.1016/j.foodchem.2012.11.042

110. Adibmehr Z, Faghihian H (2018) Novel ion-imprinted adsorbent for lead removal from aqueous solutions, selectivity and adsorption capacity improvement, and evaluation of adsorption isotherms and kinetic. Separation Science and Technology 53:2388–2400. https://doi.org/10.1080/01496395.2018.1459703

111. Shamsipur M, Rajabi HR, Pourmortazavi SM, Roushani M (2014) Ion imprinted polymeric nanoparticles for selective separation and sensitive determination of zinc ions in different matrices. Spectrochimica Acta Part A: Molecular and Biomolecular Spectroscopy 117:24–33. https://doi.org/10.1016/j.saa.2013.07.094

112. Singh DK, Mishra S (2010) Synthesis, characterization and analytical applications of Ni(II)-ion imprinted polymer. Applied Surface Science 256:7632–7637. https://doi.org/10.1016/j.apsusc.2010.06.018

113. Rajabi HR, Shamsipur M, Pourmortazavi SM (2013) Preparation of a novel potassium ion imprinted polymeric nanoparticles based on dicyclohexyl 18C6 for selective determination of K+ ion in different water samples. Materials Science and Engineering: C 33:3374–3381. https://doi.org/10.1016/j.msec.2013.04.022

114. Hashemi B, Shamsipur M, Seyedzadeh Z (2016) Preparation of a K(+) -imprinted polymer for the selective recognition of K(+) in food samples. J Sep Sci 39:2006–2012. https://doi.org/10.1002/jssc.201501359

115. Nishide H, Deguchi J, Tsuchida E (1976) SELECTIVE ADSORPTION OF METAL IONS ON CROSSLINKED POLY(VINYLPYRIDINE) RESIN PREPARED WITH A METAL ION AS A TEMPLATE. Chemistry Letters 5:169–174. https://doi.org/10.1246/cl.1976.169

116. Wuff G, Sarhan A (1972) The use of polymers with enzyme-analogous structures for the resolution of racemate. Angew Chem Int Ed 11:341–345

117. Takagishi T, Klotz IM (1972) Macromolecule-small molecule interactions; introduction of additional binding sites in polyethyleneimine by disulfide cross–linkages. Biopolymers 11:483–491. https://doi.org/10.1002/bip.1972.360110213

118. Shakerian F, Kim K-H, Kwon E, et al (2016) Advanced polymeric materials: Synthesis and analytical application of ion imprinted polymers as selective sorbents for solid phase extraction of metal ions. TrAC Trends in Analytical Chemistry 83:55–69. https://doi.org/10.1016/j.trac.2016.08.001

119. Díaz-Díaz G, Antuña-Jiménez D, Carmen Blanco-López M, et al (2012) New materials for analytical biomimetic assays based on affinity and catalytic receptors prepared by molecular imprinting. TrAC Trends in Analytical Chemistry 33:68–80. https://doi.org/10.1016/j.trac.2011.09.011

120. Birlik E, Ersöz A, Açıkkalp E, et al (2007) Cr(III)-imprinted polymeric beads: Sorption and preconcentration studies. Journal of Hazardous Materials 140:110–116. https://doi.org/10.1016/j.jhazmat.2006.06.141

121. Lazar MM, Ghiorghita C-A, Dragan ES, et al (2023) Ion-Imprinted Polymeric Materials for Selective Adsorption of Heavy Metal Ions from Aqueous Solution. Molecules 28:2798. https://doi.org/10.3390/molecules28062798

122. Branger C, Meouche W, Margaillan A (2013) Recent advances on ion-imprinted polymers. Reactive and Functional Polymers 73:859–875. https://doi.org/10.1016/j.reactfunctpolym.2013.03.021

123. Hande PE, Samui AB, Kulkarni PS (2015) Highly selective monitoring of metals by using ion-imprinted polymers. Environ Sci Pollut Res 22:7375–7404. https://doi.org/10.1007/s11356-014-3937-x

124. Jaishankar M, Tseten T, Anbalagan N, et al (2014) Toxicity, mechanism and health effects of some heavy metals. Interdisciplinary Toxicology 7:60–72. https://doi.org/10.2478/intox-2014-0009

125. Briffa J, Sinagra E, Blundell R (2020) Heavy metal pollution in the environment and their toxicological effects on humans. Heliyon 6:e04691. https://doi.org/10.1016/j.heliyon.2020.e04691

126. Hu J, Sedki M, Shen Y, et al (2021) Chemiresistor sensor based on ion-imprinted polymer (IIP)-functionalized rGO for Cd(II) ions in water. Sensors and Actuators B: Chemical 346:130474. https://doi.org/10.1016/j.snb.2021.130474

127. Lopes Pinheiro SC, Descalzo AB, Raimundo IM, et al (2012) Fluorescent ion-imprinted polymers for selective Cu(II) optosensing. Anal Bioanal Chem 402:3253–3260. https://doi.org/10.1007/s00216-011-5620-0

128. Luo X, Guo B, Wang L, et al (2014) Synthesis of magnetic ion-imprinted fluorescent CdTe quantum dots by chemical etching and their visualization application for selective removal of Cd(II) from water. Colloids and Surfaces A: Physicochemical and Engineering Aspects 462:186–193. https://doi.org/10.1016/j.colsurfa.2014.09.012

129. Shao H, Li C, Ma C, et al (2017) An ion-imprinted material embedded carbon quantum dots for selective fluorometric determination of lithium ion in water samples. Microchim Acta 184:4861–4868. https://doi.org/10.1007/s00604-017-2493-8

130. Cuartero M, Crespo GA (2018) All-solid-state potentiometric sensors: A new wave for *in situ* aquatic research. Current Opinion in Electrochemistry 10:98–106. https://doi.org/10.1016/j.coelec.2018.04.004

131. Zareh MM (2012) Plasticizers and Their Role in Membrane Selective Electrodes. In: Recent Advances in Plasticizers. IntechOpen

132. Alizadeh T, Rashedi M (2014) Synthesis of nano-sized arsenic-imprinted polymer and its use as As3+ selective ionophore in a potentiometric membrane electrode: Part 1. Analytica Chimica Acta 843:7–17. https://doi.org/10.1016/j.aca.2014.06.052

133. Abu-Dalo MA, Salam AA, Nassory NS (2015) Ion Imprinted Polymer Based Electrochemical Sensor for Environmental Monitoring of Copper(II). International Journal of Electrochemical Science 10:6780–6793. https://doi.org/10.1016/S1452-3981(23)06761-5

134. Hamidi N, Alizadeh T, Madani M (2018) A novel potentiometric Ni2+-sensor based on a Ni2+ ion-imprinted polymer. Analytical and Bioanalytical Electrochemistry 10:281–291

135. Alizadeh T, Naser Shamkhali A, Hanifehpour Y, Woo Joo S (2016) A Ca 2+ selective membrane electrode based on calcium-imprinted polymeric nanoparticles. New Journal of Chemistry 40:8479–8487. https://doi.org/10.1039/C6NJ00582A

136. Çıtlakoğlu M, Yolcu Z (2023) Dinuclear Pb(II) monomer complex: Synthesis, characterization, and application of Pb(II) ion-imprinted polymer as a selective potentiometric microsensor. Polyhedron 243:116539. https://doi.org/10.1016/j.poly.2023.116539

137. Shamsipur M, Hashemi B, Dehdashtian S, et al (2014) Silver ion imprinted polymer nanobeads based on a aza-thioether crown containing a 1,10-phenanthroline subunit for solid phase extraction and for voltammetric and potentiometric silver sensors. Analytica Chimica Acta 852:223–235. https://doi.org/10.1016/j.aca.2014.09.028

138. Olson C, Adams RN (1960) Carbon paste electrodes application to anodic voltammetry. Analytica Chimica Acta 22:582–589. https://doi.org/10.1016/S0003-2670(00)88341-5

139. Topcu C, Lacin G, Yilmaz V, et al (2018) Electrochemical Determination of Copper(II) in Water Samples Using a Novel Ion-Selective Electrode Based on a Graphite Oxide–Imprinted Polymer Composite. Analytical Letters

140. Ganjali MR, Rahmani AR, Shokoohi R, et al (2019) A Highly Sensitive and Selective Electrochemical Mercury(II) Sensor Based on Nanoparticles of Hg(II)-imprinted Polymer and Graphitic Carbon Nitride (g-C3N4). International Journal of Electrochemical Science 14:6420–6430. https://doi.org/10.20964/2019.07.80

141. Shirzadmehr A, Afkhami A, Madrakian T (2015) A new nano-composite potentiometric sensor containing an Hg2 +-ion imprinted polymer for the trace determination of mercury

ions in different matrices. Journal of Molecular Liquids 204:227–235. https://doi.org/10.1016/j.molliq.2015.01.014

142. Razmi H, Dehghanzade M (2020) Highly Selective and Sensitive Electrochemical Determination of Ni(II) in Real Samples Based on Ion-imprinted Polymer Technology. Electroanalysis 32:198–206. https://doi.org/10.1002/elan.201900097

143. Rajabi HR, Roushani M, Shamsipur M (2013) Development of a highly selective voltammetric sensor for nanomolar detection of mercury ions using glassy carbon electrode modified with a novel ion imprinted polymeric nanobeads and multi-wall carbon nanotubes. Journal of Electroanalytical Chemistry 693:16–22. https://doi.org/10.1016/j.jelechem.2013.01.003

144. An Z, Liu W, Liang Q, et al (2018) Ion-Imprinted Polymers Modified Sensor for Electrochemical Detection of Cu2+. NANO 13:1850140. https://doi.org/10.1142/S1793292018501400

145. Di Masi S, Garcia Cruz A, Canfarotta F, et al (2019) Synthesis and Application of Ion-Imprinted Nanoparticles in Electrochemical Sensors for Copper (II) Determination. ChemNanoMat 5:754–760. https://doi.org/10.1002/cnma.201900056

146. Heinze J, Frontana-Uribe BA, Ludwigs S (2010) Electrochemistry of Conducting Polymers—Persistent Models and New Concepts. Chem Rev 110:4724–4771. https://doi.org/10.1021/cr900226k

147. Di Masi S, Pennetta A, Guerreiro A, et al (2020) Sensor based on electrosynthesised imprinted polymeric film for rapid and trace detection of copper(II) ions. Sensors and Actuators B: Chemical 307:127648. https://doi.org/10.1016/j.snb.2019.127648

148. Mazloum-Ardakani M, Amini MK, Dehghan M, et al (2014) Preparation of Cu (II) imprinted polymer electrode and its application for potentiometric and voltammetric determination of Cu (II). J IRAN CHEM SOC 11:257–262. https://doi.org/10.1007/s13738-013-0295-4

149. Ma W, Chang Q, Zhao J, Ye B-C (2020) Novel electrochemical sensing platform based on ion imprinted polymer with nanoporous gold for ultrasensitive and selective determination of As3+. Microchim Acta 187:571. https://doi.org/10.1007/s00604-020-04552-9

150. Hu S, Gao G, Liu Y, et al (2019) An Electrochemical Sensor Based on ion Imprinted PPy/rGO Composite for Cd(II) Determination in Water. International Journal of Electrochemical Science 14:10714–10730. https://doi.org/10.20964/2019.11.56

151. Fu X-C, Wu J, Nie L, et al (2012) Electropolymerized surface ion imprinting films on a gold nanoparticles/single-wall carbon nanotube nanohybrids modified glassy carbon electrode for electrochemical detection of trace mercury(II) in water. Analytica Chimica Acta 720:29–37. https://doi.org/10.1016/j.aca.2011.12.071

152. Kumar D, Madhuri R, Prasad Tiwari M, et al (2011) Molecularly imprinted polymer-modified electrochemical sensor for simultaneous determination of copper and zinc. Advanced Materials Letters 2:294–297. https://doi.org/10.5185/amlett.indias.207

153. Wei P, Zhu Z, Song R, et al (2019) An ion-imprinted sensor based on chitosan-graphene oxide composite polymer modified glassy carbon electrode for environmental sensing application. Electrochimica Acta 317:93–101. https://doi.org/10.1016/j.electacta.2019.05.136

154. Torkashvand M, Gholivand MB, Azizi R (2017) Synthesis, characterization and application of a novel ion-imprinted polymer based voltammetric sensor for selective extraction and trace determination of cobalt (II) ions. Sensors and Actuators B: Chemical 243:283–291. https://doi.org/10.1016/j.snb.2016.11.094

155. Prasad BB, Jauhari D (2015) Double-ion imprinted polymer @magnetic nanoparticles modified screen printed carbon electrode for simultaneous analysis of cerium and gadolinium ions. Analytica Chimica Acta 875:83–91. https://doi.org/10.1016/j.aca.2015.02.009

156. Bai H, Wang S, Liu P, et al (2016) Electrochemical sensor based on in situ polymerized ion-imprinted membranes at graphene modified electrode for palladium determination. Journal of Electroanalytical Chemistry 771:29–36. https://doi.org/10.1016/j.jelechem.2016.04.013

157. Weibel DB, Whitesides GM (2006) Applications of microfluidics in chemical biology. Current Opinion in Chemical Biology 10:584–591. https://doi.org/10.1016/j.cbpa.2006.10.016

158. Zhou J, Li B, Qi A, et al (2020) ZnSe quantum dot based ion imprinting technology for fluorescence detecting cadmium and lead ions on a three-dimensional rotary paper-based microfluidic chip. Sensors and Actuators B: Chemical 305:127462. https://doi.org/10.1016/j.snb.2019.127462

159. Li F, Hu Y, Li Z, et al (2019) Three-dimensional microfluidic paper-based device for multiplexed colorimetric detection of six metal ions combined with use of a smartphone. Anal Bioanal Chem 411:6497–6508. https://doi.org/10.1007/s00216-019-02032-5

160. Schirhagl R, Ren K, Zare RN (2012) Surface-imprinted polymers in microfluidic devices. Sci China Chem 55:469–483. https://doi.org/10.1007/s11426-012-4544-7

161. Wang L, Li B, Wang J, et al (2022) A rotary multi-positioned cloth/paper hybrid microfluidic device for simultaneous fluorescence sensing of mercury and lead ions by using ion imprinted technologies. Journal of Hazardous Materials 428:128165. https://doi.org/10.1016/j.jhazmat.2021.128165

162. Tian Y, Liu J, Qiao J, et al (2025) Advancements in electrochemical sensingTechnology for Heavy Metal Ions Detection. Food Chem X 25:102204. https://doi.org/10.1016/j.fochx.2025.102204

163. Sala A, Brisset H, Margaillan A, et al (2022) Electrochemical sensors modified with ion-imprinted polymers for metal ion detection. TrAC Trends in Analytical Chemistry 148:116536. https://doi.org/10.1016/j.trac.2022.116536

164. Saraji M, Yousefi H (2009) Selective solid-phase extraction of Ni(II) by an ion-imprinted polymer from water samples. Journal of Hazardous Materials 167:1152–1157. https://doi.org/10.1016/j.jhazmat.2009.01.111

165. Micromax® 5018. In: Insulectro. https://insulectro-pe.com/products/dupont-5018. Accessed 17 Mar 2025

166. Davies RT, Kim J, Jang SC, et al (2012) Microfluidic filtration system to isolate extracellular vesicles from blood. Lab Chip 12:5202–5210. https://doi.org/10.1039/C2LC41006K

167. Maafa IM (2023) Inhibition of Free Radical Polymerization: A Review. Polymers (Basel) 15:488. https://doi.org/10.3390/polym15030488

168. Akhtarian S, Doostmohammadi A, Youssef K, et al (2023) Metal Microwires Functionalized with Cell-Imprinted Polymer for Capturing Bacteria in Water. ACS Appl Polym Mater 5:3235–3246. https://doi.org/10.1021/acsapm.2c01886

169. Rahman SKA, Yusof NA, Abdullah AH, et al (2018) Evaluation of porogen factors for the preparation of ion imprinted polymer monoliths used in mercury removal. PLOS ONE 13:e0195546. https://doi.org/10.1371/journal.pone.0195546

170. Tan J, Jiang Z-T, Li R, Yan X-P (2012) Molecularly-imprinted monoliths for sample treatment and separation. TrAC Trends in Analytical Chemistry 39:207–217. https://doi.org/10.1016/j.trac.2012.05.009

171. Rajabi HR, Shamsipur M, Pourmortazavi SM (2013) Preparation of a novel potassium ion imprinted polymeric nanoparticles based on dicyclohexyl 18C6 for selective determination of K+ ion in different water samples. Materials Science and Engineering: C 33:3374–3381. https://doi.org/10.1016/j.msec.2013.04.022

172. Hayvalı Z, Köksal P (2013) Syntheses and spectroscopic characterization of double-armed benzo-15-crown-5 derivatives and their sodium and potassium complexes. J Incl Phenom Macrocycl Chem 76:369–378. https://doi.org/10.1007/s10847-012-0208-7

173. Schwab S, Jung JPH, Appenroth J, et al (2017) Reduction of Sodium Migration in Polymers by Addition of 15-Crown-5 Ether as Getter Substance. ECS J Solid State Sci Technol 6:N70–N75. https://doi.org/10.1149/2.0111707jss

174. Shirazifard P, Sadjadi S, Ahmadi SJ, Faghihi F (2016) Selective solid-phase extraction of trace Pb(II) from aqueous solution using Pb(II)-ion imprinted polymer. Separation Science and Technology

175. Hu S, Xiong X, Huang S, Lai X (2016) Preparation of Pb(II) Ion Imprinted Polymer and Its Application as the Interface of an Electrochemical Sensor for Trace Lead Determination. ANAL SCI 32:975–980. https://doi.org/10.2116/analsci.32.975

176. Huang Y, Wang R (2019) Highly Effective and Low-Cost Ion-Imprinted Polymers Loaded on Pretreated Vermiculite for Lithium Recovery. Ind Eng Chem Res 58:12216–12225. https://doi.org/10.1021/acs.iecr.9b01244

177. Sun D, Zhu Y, Meng M, et al (2017) Fabrication of highly selective ion imprinted macroporous membranes with crown ether for targeted separation of lithium ion. Separation and Purification Technology 175:19–26. https://doi.org/10.1016/j.seppur.2016.11.029

178. Sun D, Meng M, Qiao Y, et al (2018) Synthesis of ion imprinted nanocomposite membranes for selective adsorption of lithium. Separation and Purification Technology 194:64–72. https://doi.org/10.1016/j.seppur.2017.10.052

179. Hashemi B, Shamsipur M, Seyedzadeh Z (2016) Synthesis of ion imprinted polymeric nanoparticles for selective pre-concentration and recognition of lithium ions. New J Chem 40:4803–4809. https://doi.org/10.1039/C5NJ03366G

180. Xu X, Li Y, Yang D, et al (2018) A facile strategy toward ion-imprinted hierarchical mesoporous material via dual-template method for simultaneous selective extraction of lithium and rubidium. Journal of Cleaner Production 171:264–274. https://doi.org/10.1016/j.jclepro.2017.10.023

181. Benedet J, Lu D, Cizek K, et al (2009) Amperometric sensing of hydrogen peroxide vapor for security screening. Anal Bioanal Chem 395:371–376. https://doi.org/10.1007/s00216-009-2788-7

182. Kuo JS, Chiu DT (2011) Controlling Mass Transport in Microfluidic Devices. Annu Rev Anal Chem (Palo Alto Calif) 4:275–296. https://doi.org/10.1146/annurev-anchem-061010-113926

183. Shao L, Petersen K, Shiri F, et al (2020) Characteristics of electrical field flow fractionation with chronoamperometry and electrochemical impedance. Micro & Nano Letters 15:13–17. https://doi.org/10.1049/mnl.2018.5663

184. Oseyemi AE, Zabihihesari A, Salahandish R, Rezai P (2025) Low-Level Salinity Monitoring in Drinking Water Using an Electrochemical Microfluidic Sensor with an Ion-Selective Polymer Membrane. Submitted to Microchemical Journal, Elsevier

185. Zhu Q, Liu Y, Zuo P, et al (2022) An isoporous ion exchange membrane for selective Na+ transport. Journal of Membrane Science 659:120805. https://doi.org/10.1016/j.memsci.2022.120805

186. Vrbka L, Vondrášek J, Jagoda-Cwiklik B, et al (2006) Quantification and rationalization of the higher affinity of sodium over potassium to protein surfaces. Proceedings of the

National Academy of Sciences 103:15440–15444. https://doi.org/10.1073/pnas.0606959103

187. Lu S-H, Li Y, Wang X (2023) Soft, flexible conductivity sensors for ocean salinity monitoring. J Mater Chem B 11:7334–7343. https://doi.org/10.1039/D3TB01167D

188. Xie N, Zhang H, Liu B, et al (2018) In-Line Microfiber-Assisted Mach–Zehnder Interferometer for Microfluidic Highly Sensitive Measurement of Salinity. IEEE Sensors Journal 18:8767–8772. https://doi.org/10.1109/JSEN.2018.2869273

189. Sun C, Chen S-T, Hsiao P-J (2015) Mapping the Salinity Gradient in a Microfluidic Device with Schlieren Imaging. Sensors 15:11587–11600. https://doi.org/10.3390/s150511587

190. Khanikar T, Pathak AK, Singh VK (2018) Reflectance-based no core fiber sensor with enhanced Sensitivity for salinity detection. Optik 159:1–8. https://doi.org/10.1016/j.ijleo.2018.01.053

191. Hussain I, Das M, Ahamad KU, Nath P (2017) Water salinity detection using a smartphone. Sensors and Actuators B: Chemical 239:1042–1050. https://doi.org/10.1016/j.snb.2016.08.102

192. Robinson S, Nakkeeran R (2012) PC based optical salinity sensor for different temperatures. Photonic Sens 2:187–192. https://doi.org/10.1007/s13320-012-0055-6

193. Farshchi Heydari MJ, Tabatabaei N, Rezai P (2022) Low-Cost Resistive Microfluidic Salinity Sensor for High-Precision Detection of Drinking Water Salt Levels. ACS Omega 7:15529–15539. https://doi.org/10.1021/acsomega.2c00268

194. Liu S, Ding J, Qin W (2018) Current pulse based ion-selective electrodes for chronopotentiometric determination of calcium in seawater. Analytica Chimica Acta 1031:67–74. https://doi.org/10.1016/j.aca.2018.06.018

195. De Marco R, Clarke G, Pejcic B (2007) Ion-Selective Electrode Potentiometry in Environmental Analysis. Electroanalysis 19:1987–2001. https://doi.org/10.1002/elan.200703916

196. James HJ, Carmack Gary, Freiser Henry (1972) Coated wire ion-selective electrodes. Anal Chem 44:856–857. https://doi.org/10.1021/ac60312a046

197. Rezk MR, Fayed AS, Marzouk HM, Abbas SS (2017) Green Ion Selective Electrode Potentiometric Application for the Determination of Cinchocaine Hydrochloride in Presence of Its Degradation Products and Betamethasone Valerate: A Comparative Study of Liquid and Solid Inner Contact Ion-Selective Electrode Membranes. J Electrochem Soc 164:H628. https://doi.org/10.1149/2.0921709jes

198. Rezk MR, Fayed AS, Marzouk HM, Abbas SS (2018) Potentiometric ion-selective electrodes for determination of cyclopentolate hydrochloride and phenylephrine

hydrochloride in their challenging ophthalmic formulation. J Solid State Electrochem 22:3351–3361. https://doi.org/10.1007/s10008-018-4045-5

199. Soliman MA, Mahmoud AM, Elzanfaly ES, Abdel Fattah LE (2024) Design and application of supramolecular based solid-contact ion-selective electrode for selective green determination of tenofovir disoproxil fumarate. International Journal of Electrochemical Science 19:100477. https://doi.org/10.1016/j.ijoes.2024.100477

200. Zhang Y, Liu Y, Xu W, et al (2024) Novel electrochemical sensor based on rGO@TiO2 composite material and ion-imprinted polymer modification for highly selective detection of cadmium ions in real samples. Ionics. https://doi.org/10.1007/s11581-024-05410-x

201. Peng J, Tian M, Cantillo NM, Zawodzinski T (2018) The ion and water transport properties of K+ and Na+ form perfluorosulfonic acid polymer. Electrochimica Acta 282:544–554. https://doi.org/10.1016/j.electacta.2018.06.035

202. Zhou X, Wang Z, Epsztein R, et al (2020) Intrapore energy barriers govern ion transport and selectivity of desalination membranes. Science Advances 6:eabd9045. https://doi.org/10.1126/sciadv.abd9045

203. Epsztein R, DuChanois RM, Ritt CL, et al (2020) Towards single-species selectivity of membranes with subnanometre pores. Nat Nanotechnol 15:426–436. https://doi.org/10.1038/s41565-020-0713-6

204. Gomes C, Sadoyan G, Dias RCS, Costa MRPFN (2017) Development of Molecularly Imprinted Polymers to Target Polyphenols Present in Plant Extracts. Processes 5:72. https://doi.org/10.3390/pr5040072

205. Rahman SM, Mohd Said S, S B, et al (2016) Synthesis and characterization of polymer electrolyte using deep eutectic solvents and electrospun PVA membrane. Industrial & Engineering Chemistry Research 55:. https://doi.org/10.1021/acs.iecr.6b01754

206. Lim H-R, Kim Y-S, Kwon S, et al (2020) Wireless, Flexible, Ion-Selective Electrode System for Selective and Repeatable Detection of Sodium. Sensors 20:3297. https://doi.org/10.3390/s20113297

207. Giovannitti A, Nielsen CB, Rivnay J, et al (2016) Sodium and Potassium Ion Selective Conjugated Polymers for Optical Ion Detection in Solution and Solid State. Advanced Functional Materials 26:514–523. https://doi.org/10.1002/adfm.201503791

208. Ozer T, Henry CS (2022) Microfluidic-based ion-selective thermoplastic electrode array for point-of-care detection of potassium and sodium ions. Microchim Acta 189:152. https://doi.org/10.1007/s00604-022-05264-y

209. Samreen S, Ali MS, Akhtar MW, et al (2023) Cu-Doped ZnO Nanoparticle Electrode for Precise and Rapid Sodium Ion Detection in Water Samples. ECS J Solid State Sci Technol 12:077007. https://doi.org/10.1149/2162-8777/ace84d

210. Cho S-K, Cho W-J (2021) Highly Sensitive and Selective Sodium Ion Sensor Based on Silicon Nanowire Dual Gate Field-Effect Transistor. Sensors 21:4213. https://doi.org/10.3390/s21124213

211. Cazalé A, Sant W, Launay J, et al (2013) Study of field effect transistors for the sodium ion detection using fluoropolysiloxane-based sensitive layers. Sensors and Actuators B: Chemical 177:515–521. https://doi.org/10.1016/j.snb.2012.11.054

212. Cai X, Li J, Zhang Z, et al (2014) Novel Pb2+ Ion Imprinted Polymers Based on Ionic Interaction via Synergy of Dual Functional Monomers for Selective Solid-Phase Extraction of Pb2+ in Water Samples. ACS Appl Mater Interfaces 6:305–313. https://doi.org/10.1021/am4042405

213. Vergili I, Gönder ZB, Kaya Y, et al (2017) Lead removal from battery wastewater using synthesized poly(ethyleneglycol dimethacrylate-methacrylic acid) gel bead and poly(methacrylic acid) hydrogel. Polym Bull 74:2605–2624. https://doi.org/10.1007/s00289-016-1855-4

214. Babyak C, Smart RB (2004) Electrochemical Detection of Trace Concentrations of Cadmium and Lead with a Boron-Doped Diamond Electrode: Effect of KCl and KNO3 Electrolytes, Interferences and Measurement in River Water. Electroanalysis 16:175–182. https://doi.org/10.1002/elan.200302794

215. Fan F, Dou J, Ding A, et al (2013) Determination of Lead by Square Wave Anodic Stripping Voltammetry Using an Electrochemical Sensor. ANAL SCI 29:571–577. https://doi.org/10.2116/analsci.29.571

216. Dash D, Kumar S, Mallika C, Mudali UK (2012) New Data on Activity Coefficients of Potassium, Nitrate, and Chloride Ions in Aqueous Solutions of KNO3 and KCl by Ion Selective Electrodes. International Scholarly Research Notices 2012:730154. https://doi.org/10.5402/2012/730154

217. Soleymanpour A, Shafaatian B, Kor K, Hasaninejad AR (2012) Coated wire lead(II)-selective electrode based on a Schiff base ionophore for low concentration measurements. Monatsh Chem 143:181–188. https://doi.org/10.1007/s00706-011-0634-z

218. Dahaghin Z, Kilmartin PA, Mousavi HZ (2018) Simultaneous determination of lead(II) and cadmium(II) at a glassy carbon electrode modified with GO@Fe3O4@benzothiazole-2-carboxaldehyde using square wave anodic stripping voltammetry. Journal of Molecular Liquids 249:1125–1132. https://doi.org/10.1016/j.molliq.2017.11.114

219. Letsoalo MR, Ambushe AA, Mamo MA (2021) Novel Chemoresistive Sensor for Sensitive Detection of Pb2+ Ions Using an Interdigital Gold Electrode Fabricated with a Reduced Graphene Oxide-Based Ion-Imprinted Polymer. ACS Omega 6:31528–31538. https://doi.org/10.1021/acsomega.1c03955

220. Bojdi MK, Mashhadizadeh MH, Behbahani M, et al (2014) Synthesis, characterization and application of novel lead imprinted polymer nanoparticles as a high selective

electrochemical sensor for ultra-trace determination of lead ions in complex matrixes. Electrochimica Acta 136:59–65. https://doi.org/10.1016/j.electacta.2014.05.095

221. Huang Y, Wang R (2018) An efficient lithium ion imprinted adsorbent using multi-wall carbon nanotubes as support to recover lithium from water. Journal of Cleaner Production 205:201–209. https://doi.org/10.1016/j.jclepro.2018.09.076

222. Liang C, Zhang X, Liu W, et al (2023) Thermo-responsive ion imprinted polymer on the surface of magnetic carbon nanospheres for recognizing and capturing low-concentration lithium ion. Minerals Engineering 201:108210. https://doi.org/10.1016/j.mineng.2023.108210

223. Siddaiah T, Ojha P, Gopal NO, et al (2018) Thermal, structural, optical and electrical properties of PVA/MAA:EA polymer blend filled with different concentrations of Lithium Perchlorate. Journal of Science: Advanced Materials and Devices 3:456–463. https://doi.org/10.1016/j.jsamd.2018.11.004

224. (2014) 7.3: Sizes of Atoms and Ions. In: Chemistry LibreTexts. https://chem.libretexts.org/Bookshelves/General_Chemistry/Map%3A_Chemistry_-_The_Central_Science_(Brown_et_al.)/07%3A_Periodic_Properties_of_the_Elements/7.03%3A_Sizes_of_Atoms_and_Ions. Accessed 16 Feb 2025

Appendix

In this chapter, we dug deeper into the working of the membrane-integrated sensor by investigating the effects of the key parameters associated with sensor fabrication and operation, towards optimizing its overall performance. This study was conducted on the lead-ion imprinted polymer (Pb-IIP) membrane sensor using the Taguchi Design of Experiments (DOE) approach. Three main factors were selected for optimization, namely: flowrate, template:monomer ratio, and template:crosslinker ratio. Applied voltage was maintained at the optimal 0.6 V while membrane thickness was 300 μm all through. The goal was to identify the most effective combination of synthesis parameters to enhance the sensor's electrochemical response for Pb^{2+} detection.

A.1 Optimization of Complex Pb-IIP Compositions Using Taguchi Design of Experiment (DOE)

In this chapter, the optimization of lead-ion imprinted polymer (Pb-IIP) membrane sensor compositions was performed using the Taguchi Design of Experiments (DOE) approach. Three main factors were selected for optimization while keeping the applied voltage (0.6 V) and membrane thickness (300 μm) constant. The goal was to identify the most effective combination of synthesis parameters to enhance the sensor's electrochemical response for Pb^{2+} detection.

A.1.1 Experimental Design

The factors and their respective levels used in the Taguchi L9 orthogonal array are listed below:

- Flow Rate (µL/min): 100, 400, 800
- Template:Monomer Ratio: 1:1, 1:2, 1:4
- Template:Crosslinker Ratio: 1:10, 1:20, 1:30

Table A-1 presents the Taguchi L9 design matrix along with the chemical composition for each run.

Table A-1 Taguchi L9 DOE matrix and composition details.

Run	Flow Rate (µL/min)	Template: Monomer	Template: Crosslinker	$Pb(NO_3)_2$ (mg)	8-HQ (mg)	MAA (µL)	EGDMA (µL)	Solvent (mL)
1	100	1:1	1:10	33.12	14.54	17.24	206.8	2.0
2	100	1:2	1:20	33.12	14.54	34.48	413.6	2.0
3	100	1:4	1:30	33.12	14.54	68.96	620.4	2.0
4	400	1:2	1:30	33.12	14.54	34.48	620.4	2.0
5	400	1:4	1:10	33.12	14.54	68.96	206.8	2.0
6	400	1:1	1:20	33.12	14.54	17.24	413.6	2.0
7	800	1:4	1:20	33.12	14.54	68.96	413.6	2.0
8	800	1:1	1:30	33.12	14.54	17.24	620.4	2.0
9	800	1:2	1:10	33.12	14.54	34.48	206.8	2.0

A.1.2 Sensor Performance Evaluation

Each run was evaluated using $Pb(NO_3)_2$ concentrations of 0, 0.01, 0.1, 1, 10, 50, and 100 ppm. Current responses were measured and tabulated (Table A-2). Among these, the current response at

10 ppm was selected as the representative metric for Taguchi analysis. The concentration of 10 ppm was chosen as a mid-range value to capture reliable performance trends while ensuring sensor response remains within the linear operating range.

Table A-2 Expansion of Taguchi of DOE matrix L9 (to L27) with current response of each run on 0-100 ppm $Pb(NO_3)_2$ concentration.

Run	Flow Rate (µL/min)	Template: Monomer	Template: Crosslinker	Pb^{2+} Conc. (ppm)	Current Response (µA)	Standard Deviation
1	100	1:1	1:10	0	0.0545	0.001121
1	100	1:1	1:10	0.01	0.0785	0.002155
1	100	1:1	1:10	0.1	0.0976	0.016455
1	100	1:1	1:10	1	0.1248	0.002358
1	100	1:1	1:10	10	0.1483	0.004613
1	100	1:1	1:10	50	0.2460	0.013352
1	100	1:1	1:10	100	0.3365	0.011566
2	100	1:2	1:20	0	0.0513	0.002063
2	100	1:2	1:20	0.01	0.0741	0.004051
2	100	1:2	1:20	0.1	0.0718	0.002109
2	100	1:2	1:20	1	0.0578	0.001896
2	100	1:2	1:20	10	0.0685	0.000991
2	100	1:2	1:20	50	0.0926	0.002584
2	100	1:2	1:20	100	0.1009	0.007119
3	100	1:4	1:30	0	0.0144	0.000125
3	100	1:4	1:30	0.01	0.0125	0.000672
3	100	1:4	1:30	0.1	0.0140	0.000936
3	100	1:4	1:30	1	0.0101	0.000286
3	100	1:4	1:30	10	0.0098	0.000228
3	100	1:4	1:30	50	0.0094	0.000323
3	100	1:4	1:30	100	0.0088	0.00038
4	400	1:2	1:30	0	0.0176	0.000285
4	400	1:2	1:30	0.01	0.0166	0.000563
4	400	1:2	1:30	0.1	0.0152	0.000945
4	400	1:2	1:30	1	0.0153	0.001779
4	400	1:2	1:30	10	0.0149	0.000493
4	400	1:2	1:30	50	0.0160	0.000406
4	400	1:2	1:30	100	0.0155	0.000627
5	400	1:4	1:10	0	0.0655	0.0027
5	400	1:4	1:10	0.01	0.0671	0.003517
5	400	1:4	1:10	0.1	0.0724	0.000998
5	400	1:4	1:10	1	0.0769	0.002685
5	400	1:4	1:10	10	0.1334	0.001266
5	400	1:4	1:10	50	0.2895	0.002466

5	400	1:4	1:10	100	0.4194	0.000404
6	400	1:1	1:20	0	0.0177	0.000666
6	400	1:1	1:20	0.01	0.0207	0.000225
6	400	1:1	1:20	0.1	0.0211	0.000688
6	400	1:1	1:20	1	0.0215	0.00074
6	400	1:1	1:20	10	0.0397	0.001525
6	400	1:1	1:20	50	0.0983	0.001722
6	400	1:1	1:20	100	0.1466	0.003459
7	800	1:4	1:20	0	0.0409	0.002367
7	800	1:4	1:20	0.01	0.0520	0.001352
7	800	1:4	1:20	0.1	0.0308	0.00037
7	800	1:4	1:20	1	0.0419	0.000705
7	800	1:4	1:20	10	0.0964	0.000733
7	800	1:4	1:20	50	0.1765	0.000872
7	800	1:4	1:20	100	0.2526	0.001168
8	800	1:1	1:30	0	0.0092	0.000301
8	800	1:1	1:30	0.01	0.0094	0.001075
8	800	1:1	1:30	0.1	0.0072	0.000217
8	800	1:1	1:30	1	0.0080	0.000623
8	800	1:1	1:30	10	0.0076	0.000309
8	800	1:1	1:30	50	0.0065	0.000407
8	800	1:1	1:30	100	0.0061	0.000284
9	800	1:2	1:10	0	0.0212	0.000877
9	800	1:2	1:10	0.01	0.0213	0.001548
9	800	1:2	1:10	0.1	0.0214	0.000358
9	800	1:2	1:10	1	0.0215	0.000704
9	800	1:2	1:10	10	0.0374	0.003559
9	800	1:2	1:10	50	0.0612	0.005026
9	800	1:2	1:10	100	0.0944	0.006031

A.1.3. Signal-to-Noise Ratio Analysis

The Taguchi method considers "larger is better" for maximizing sensor signal output. The Signal-to-Noise (S/N) ratio for each experimental run is calculated using the formula:

$$S/N = -10\, log_{10}\pi\left(\frac{1}{n}\sum_{i=1}^{n}\frac{1}{{y_i}^2}\right)$$

where y_i represents the observed response (current in μA) for i^{th} trial, and n is the number of repetitions.

The S/N ratio analysis for the three factors is shown in Table A-3.

Table A-3 Response table for S/N ratios (larger is better)

Level	Flowrate (μL/min)	Template : Monomer	Template : Crosslinker
1	-26.68	-29.00	-20.87
2	-27.35	-29.46	-23.88
3	-30.41	-26.00	-39.70
Delta	3.74	3.46	18.83
Rank	2	3	1

The crosslinker ratio had the most significant impact on current response. This is likely since crosslinkers influence the rigidity and porosity of the polymer matrix, thereby affecting the accessibility of imprinted sites to Pb^{2+} ions. Lower crosslinking (1:10) may result in more flexible polymer chains and improved analyte diffusion.

A.1.4. Mean Response Analysis

Mean response values at 10 ppm Pb^{2+} for each factor level are summarized in Table A-4.

Table A-4 Response table for means

Level	Flowrate (μL/min)	Template : Monomer	Template : Crosslinker
1	0.07553	0.06520	0.10637
2	0.06267	0.04027	0.06820
3	0.04713	0.07987	0.01077
Delta	0.02840	0.03960	0.09560
Rank	3	2	1

Fig. A-1. illustrates the main effect of each factor on the current response at 10 ppm.

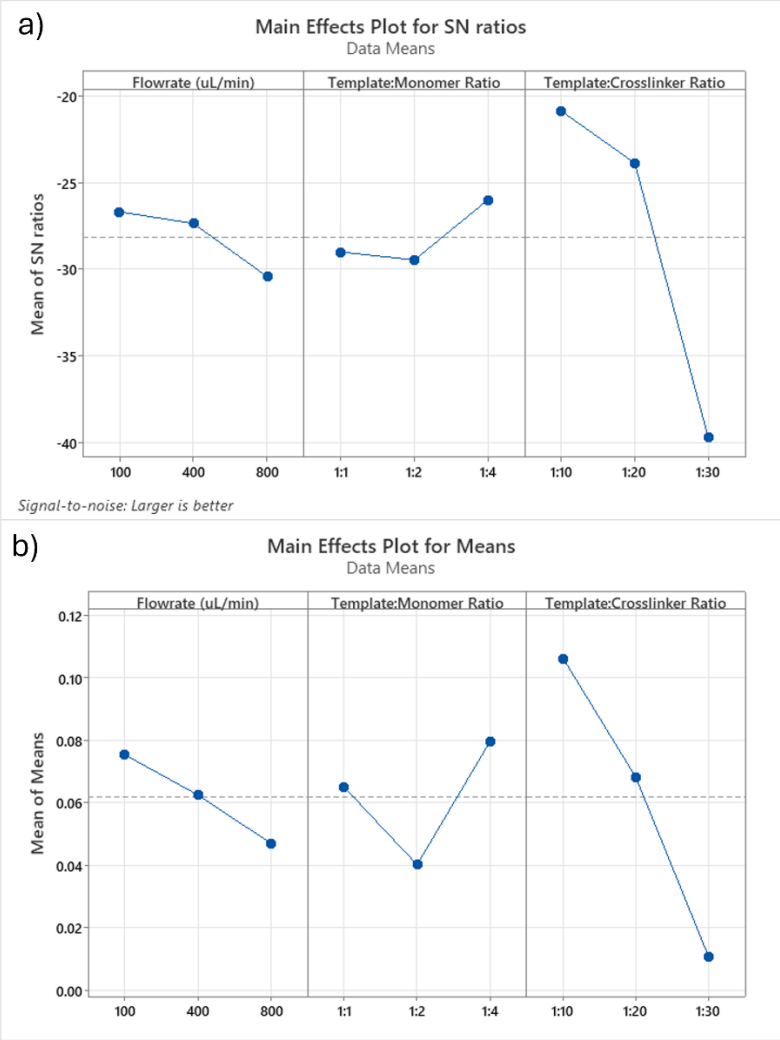

Fig. A-1 Main effects of flowrate, template:monomer ratio and template:cross-linker ratio on current response (a) SN ratios (b) Means .

- **Main effect plot for Flow Rate on Current Response:** A decreasing trend is observed as flow rate increases, indicating reduced interaction time between analyte and sensor surface. At higher flow rates, the residence time of Pb^{2+} ions on the membrane decreases, potentially limiting effective binding.

- **Main effect plot for Template:Monomer Ratio on Current Response:** The optimal monomer ratio appears to be 1:4, yielding the highest mean current response. Higher monomer content likely increases the density of binding sites, enhancing Pb^{2+} capture efficiency.
- **Main effect plot for Template:Crosslinker Ratio on Current Response:** A strong decrease is observed as crosslinker content increases, showing that 1:10 is optimal. Excessive crosslinking may hinder ion diffusion into the imprinted sites by reducing polymer flexibility.

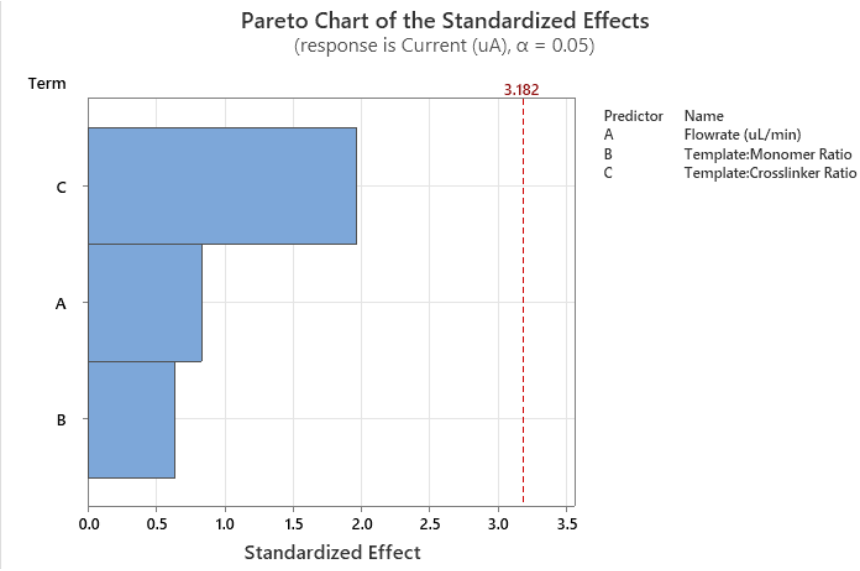

Fig. A-2 Pareto chart of standardized effects(Δ Mean Response)

The Pareto chart visually confirms that Template : Crosslinker ratio has the highest influence on sensor response, followed by Template : Monomer ratio and Flow Rate. The effect sizes are based on the Δ values from mean response analysis, helping prioritize factors during optimization.

A.1.5. Optimal Conditions and Interpretation

From the above analysis:

- **Most influential factor:** Template:Crosslinker ratio (1:10 optimal)
- **Optimal Conditions:**
    - Flowrate: **100 µL/min**
    - Template:Monomer: **1:4**
    - Template:Crosslinker: **1:10**

This combination ensures sufficient residence time, high density of monomer sites for imprinting, and a flexible matrix structure that facilitates efficient Pb^{2+} ion uptake.

A.1.6. Regression Analysis

A linear regression model was developed to further evaluate factor contributions. The coefficients for all combinations are listed in Table A-5. Notably, the template:crosslinker ratio of 1:30 exhibited a nearly significant negative coefficient ($p = 0.068$), indicating excessive crosslinking reduces sensor performance.

Table A-5 Summary of regression coefficients.

Term	Coef	SE Coef	T-Value	P-Value
Constant	0.1273	0.0377	3.38	0.043
Flowrate (uL/min)	-0.000040	0.000049	-0.83	0.467
Template:Monomer Ratio				
1:2	-0.0249	0.0342	-0.73	0.519
1:4	0.0147	0.0342	0.43	0.697
Template:Crosslinker Ratio				
1:20	-0.0382	0.0342	-1.12	0.346
1:30	-0.0956	0.0342	-2.80	0.068

Summary of regression analysis.

- R-sq = 76.89%
- Adjusted R-sq = 38.37%
- Template : Crosslinker = most impactful ($p \sim 0.068$)
- Flowrate and Template : Monomer not as significant ($p > 0.1$).

A.1.7. Analysis of Variance (ANOVA)

Table A-6 shows the ANOVA summary. Although none of the factors show statistical significance ($p < 0.05$), the relatively higher F-value and lower p-value for Template : Crosslinker ratio support its dominant influence, consistent with physical observations and prior sections.

Table A-6 ANOVA table.

Source	DF	Adj SS	Adj MS	F-Value	P-Value
Regression	5	0.01751	0.00350	2.00	0.302
Flowrate	1	0.00121	0.00121	0.69	0.467
Template : Monomer	2	0.00240	0.00120	0.69	0.569
Template : Crosslinker	2	0.01389	0.00695	3.96	0.144
Error	3	0.00526	0.00176		
Total	8	0.02278			

A.1.8. Conclusion

Taguchi DOE successfully identified the optimal composition for maximizing the current response of Pb-IIP membrane sensors. Among the factors studied, the Template : Crosslinker ratio was the most influential. The regression model supports the observed trends.

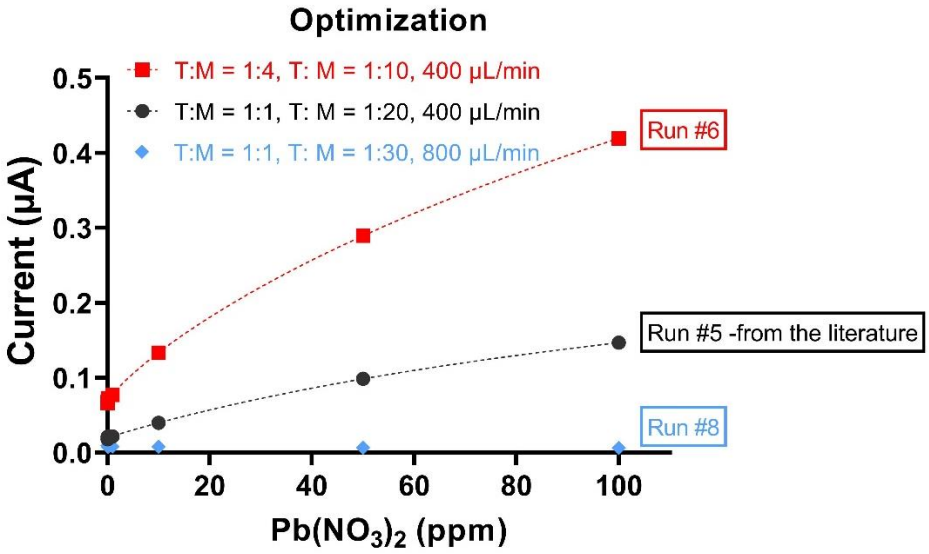

Fig. A-3 Comparison of the dose-response curves of Pb-IIP membrane design number 6, 5 and 8 (according to table A-1)

Key Optimal Parameters:

- Flowrate: 400 µL/min
- Template:Monomer: 1:4
- Template:Crosslinker: 1:10

These parameters provide the highest current responses across all tested concentrations (0-100 ppm) of Pb^{2+} (Fig. A-3), highlighting their utility in designing highly sensitive Pb-IIP-based membrane sensors. The observed results can be mechanistically explained by improvements in binding site availability and matrix permeability under optimized polymer compositions.